

Numerical Modeling of Suspension and Particle Transport in Thermal Spray Processes

MEHDI JADIDI

A Thesis

in

the Department

of

Mechanical and Industrial Engineering

Presented in Partial Fulfillment of the Requirements
for the Degree of Doctor of Philosophy (Mechanical Engineering) at
Concordia University
Montreal, Quebec, Canada

November 2016

© MEHDI JADIDI, 2016

School of Graduate Studies

This is to certify that the thesis prepared,

By: MEHDI JADIDI

Entitled: Numerical Modeling of Suspension and Particle Transport in Thermal Spray Processes

and submitted in partial fulfillment of the requirements for the degree of

Doctor of Philosophy (Mechanical Engineering)

Complies with the regulations of the University and meets the accepted standards with respect to originality and quality.

Signed by the final examining committee:

<u>Prof. Jayakumar Rajagopalan</u>	Chair
<u>Prof. Christian Moreau</u>	Examiner
<u>Prof. Marius Paraschivoiu</u>	Examiner
<u>Prof. Fariborz Haghighat</u>	External to the department
<u>Prof. Brian Fleck</u>	External to the university
<u>Prof. Ali Dolatabadi</u>	Supervisor

Approved by _____

Chair of Department or Graduate Program Director

Date _____

Abstract

Numerical Modeling of Suspension and Particle Transport in Thermal Spray Processes

Mehdi Jadidi, Ph.D.

Concordia University, 2016

Fine microstructured coatings have attracted many attentions in recent years due to various unique properties such as remarkable wear resistance, enhanced catalytic behavior, and superior thermal insulation. Suspension thermal sprays have been shown to be viable techniques in generating this kind of coatings. In these techniques, suspension which is a combination of a base liquid and fine solid particles is injected into a high-temperature high-velocity jets. After suspension breakup, the evaporation/combustion of base liquid becomes dominant. Then, the remained particles are accelerated and heated up by the gas flow and are deposited on a substrate which results in the generation of dense and well-adhered coatings.

Suspension thermal spraying is very complex and many fields such as turbulent flow, multiphase flow, compressible flow, combustion, atomization, suspension properties, and plasma physics are involved in the mentioned technique. In addition, many parameters and mechanisms in this technique are still unknowns. Therefore, both numerical and experimental studies should be performed to obtain a comprehensive understanding of various phenomena in suspension thermal spraying and to improve the coating quality. The main goal of this study is the numerical modeling of suspension thermal sprays.

An Eulerian-Lagrangian approach with two-way coupling assumption is presented and suspension droplet evolution in the atmospheric plasma spraying and high velocity oxygen fuel spraying techniques is investigated. In this model, suspension is considered as a multi-component mixture and a predefined droplet distribution is injected into the jet. In this approach, the breakup process is simulated using Taylor Analogy Breakup (TAB), and Kelvin-Helmholtz Rayleigh-Taylor (KHRT) breakup models. After breakup process is complete, the liquid component of suspension droplet evaporates/burns, and the particles/agglomerates are tracked in the domain. In general, the effects of suspension injection velocity, suspension properties, suspension injector location, standoff distance, substrate shape, and gas properties on the coating characteristics can be investigated by this approach. For example, in the case of radial injection of suspension into a plasma plume, it is illustrated that if particles move close to the jet centerline, particle velocity and temperature as well as probability of particle impact on the substrate will increase.

The mentioned Eulerian-Lagrangian approach revealed that the breakup phenomenon mainly controls the droplets/particles trajectories, temperatures and velocities. However, the typical TAB and KHRT models ignore liquid/suspension column deformation, and need experimental calibration. To study the breakup process in more details, the effect of nonuniform gaseous crossflow and liquid column perturbations on the primary breakup of liquid jets are investigated. A coupled level set and volume-of-fluid method together with the large eddy simulation turbulence model are used to study the behavior of nonturbulent liquid jets in nonuniform crossflows. It is shown that liquid penetration height is significantly affected by the crossflow nonuniformity. In addition, to investigate the effects of liquid column perturbations on the breakup process, experimental studies are performed using shadowgraphy technique. General correlations for the penetration height, the column breakup point, and the onset of surface breakup are presented. It is

found that the liquid column perturbations result in formation of large ligaments very close to the liquid and gas flows interaction point. These ligaments control the droplet size distribution and have significant effects on particle in-flight behavior, and coatings quality. The results of these studies can be used to estimate the spray trajectory in suspension plasma spray process, and to improve the accuracy of TAB and KHRT breakup models.

Contribution of Authors

This thesis is prepared in manuscript format. Some parts of chapter 1 and all chapters 2, 3, 4, and 5 are reprinted from journal papers. Mehdi Jadidi who is the author of the current thesis, is the first author of all the journal papers. He is responsible for running the simulations, doing the experiments, and post processing the results. The papers titles, journals names, volumes numbers, pages numbers, and the contribution of the co-authors are given below:

Chapter 1: some parts of this chapter is from a review paper entitled "A comprehensive review on fluid dynamics and transport of suspension/liquid droplets and particles in high-velocity oxygen-fuel (HVOF) thermal spray" and published in "Coatings, 2015, volume 5, pages 576-645". The co-authors of this review paper are Dr. Sara Moghtadernejad, and Prof. Ali Dolatabadi. Dr. Moghtadernejad has contributed in editing and classifying the chapters and subchapters of this review paper. She also helped the first author to cover some topics related to chemical engineering (e.g. surfactant types and their influence on the suspension properties) in the review paper. Prof. Dolatabadi was the supervisor of the project.

Chapter 2: the paper entitled "A three-dimensional analysis of the suspension plasma spray impinging on a flat substrate" is published in "Journal of Thermal Spray Technology, 2015, volume 24, pages 11-23". The co-authors of this paper are Mr. Milad Mousavi, Dr. Sara Moghtadernejad, and Prof. Ali Dolatabadi. Mr. Mousavi helped the first author to find and estimate the material properties. Dr. Moghtadernejad has contributed in editing the paper and post processing some of the results. Prof. Dolatabadi was the supervisor of the project.

Chapter 3: the paper entitled "Numerical modeling of suspension HVOF spray" is published in "Journal of Thermal Spray Technology, 2016, volume 25, pages 451-464". Dr. Sara

Moghtadernejad, and Prof. Ali Dolatabadi are the co-authors of the paper. Dr. Moghtadernejad helped in the subjects related to combustion and chemical engineering. She has also contributed in post processing some of the results and editing the paper. The supervisor of the project was Prof. Dolatabadi.

Chapter 4: the paper entitled "Numerical simulation of primary breakup of round nonturbulent liquid jets in shear-laden gaseous crossflow" is accepted in the Journal of Atomization and Sprays (it is in press now). The co-authors of the paper are Dr. Sara Moghtadernejad, and Prof. Ali Dolatabadi. Dr. Moghtadernejad helped the first author in post processing some results and manuscript editing. Prof. Dolatabadi was the research supervisor.

Chapter 5: the paper entitled "Penetration and breakup of free liquid jets in transverse free air jets with application in suspension-solution thermal sprays" is published in "Material and Design, 2016, volume 110, pages 425-435". Dr. Sara Moghtadernejad, and Prof. Ali Dolatabadi are the co-authors of the paper. Dr. Moghtadernejad helped the first author in 1/4 of the experimental works and post processing the results. The research supervisor was Prof. Dolatabadi.

Acknowledgements

I would like to thank my supervisor Prof. Ali Dolatabadi for his help and support during my PhD graduate studies. I would also like to thank my committee members for their helpful comments and ideas.

I would like to say a very special thank you to my parents for their love, support, and encouragement.

I would also like to express my appreciation to my colleagues and friends, Dr. Ghobad Amini, Dr. Moussa Tembely, Dr. Sara Moghtadernejad, and Mr. Milad Mousavi for helping me in several stages of my research.

Table of Contents

List of Figures	xi
List of Tables	xvii
Nomenclature	xviii
1 Introduction	1
1.1 Overview	1
1.2 Numerical Methods and Previous Studies	7
1.3 Objectives	15
1.4 Thesis Layout	17
2 A Three-Dimensional Analysis of the Suspension Plasma Spray Impinging on a Flat Substrate.....	18
2.1 Introduction	19
2.2 Mathematical Modeling	24
2.3 Results and Discussions	29
2.4 Summary and Conclusions.....	44
3 Numerical Modeling of Suspension HVOF Spray	45
3.1 Introduction	46
3.2 Mathematical Modeling	48
3.3 Results and Discussions	57
3.4 Summary and Conclusions.....	69
4 Numerical Simulation of Primary Breakup of Round Nonturbulent Liquid Jets in Shear-Laden Gaseous Crossflow.....	70
4.1 Introduction	71
4.2 Numerical Modeling	75
4.2.1 Numerical Method	75
4.2.2 Simulation Configuration.....	80
4.3 Results and Discussions	86
4.4 Summary and Conclusions.....	104
5 Penetration and Breakup of Liquid Jet in Transverse Free Air Jet with Application in Suspension-Solution Thermal Sprays.....	106

5.1	Introduction	107
5.2	Experimental Setup	114
5.3	Results and Discussion.....	117
5.4	Summary and Conclusions.....	130
6	Conclusions and Suggestions for Future Work	132
6.1	Summary	132
6.2	Scope for Research and Future Work	134
	References.....	137
	Appendix: A coupled level set and volume of fluid method with application to compressible two-phase flow	152

List of Figures

Figure 1.1 Schematic of a typical plasma torch.....	2
Figure 1.2 Schematic of a typical HVOF nozzle [1]	3
Figure 1.3 External radial injection of suspension into HVOF jet, (a) spray atomization and (b) mechanical injection (continuous jet) [9]	4
Figure 1.4 The cross-flow suspension atomization is divided into three zones; cylindrical liquid jet, disintegration of liquid column, and droplets [11]	5
Figure 1.5 A schematic of a suspension droplet evolution in a high temperature jet or flame [8].	5
Figure 1.6 A schematic view of suspension/liquid injected into non-uniform cross-flow in thermal spray systems.....	11
Figure 1.7 Function α which represents the fractional volume of the cell occupied by liquid [1]	12
Figure 2.1 The schematic of a typical impinging gas-jet system.....	22
Figure 2.2 The schematic of suspension injection into a plasma plume.....	23
Figure 2.3 The suspension atomization, evaporation and particle agglomeration in the realistic and the model cases [19]	26
Figure 2.4 The droplet size distribution injected into the plasma jet as well as a schematic diagram of the discrete injector	26
Figure 2.5 Computational domain for the jet simulation.....	28
Figure 2.6 The comparison between gas velocities at various standoff distances for a) without suspension injection, b) with suspension injection.....	30
Figure 2.7 The comparison between gas temperatures at various standoff distances for a) without suspension injection, b) with suspension injection.....	31

Figure 2.8 The penetration depth of suspension in the plasma plume as a function of standoff distance	32
Figure 2.9 The variation of gas temperature and velocity near the substrate (at $d_{fs}=1$ mm) (a) $SD=40$ mm and (b) $SD=60$ mm as a function of standoff distance (size of each figure is the same as substrate size	34
Figure 2.10 Change in the plasma temperature as a function of distance from the substrate. T_{sub} stands for the plasma temperature when the substrate exists in the flow and T stands for the plasma temperature when there is no substrate in the domain	35
Figure 2.11 Change in the plasma temperature as a function of distance from the substrate and substrate standoff distance.....	35
Figure 2.12 The effect of standoff distance on the particle temperature and trajectory	37
Figure 2.13 The effect of standoff distance on the particle velocity and trajectory	37
Figure 2.14 Particle size distributions as a function of cumulative percentage of particles at different standoff distances.....	39
Figure 2.15 Particle temperature profiles as a function of cumulative percentage of particles at different standoff distances.....	39
Figure 2.16 Particle velocity profiles as a function of cumulative percentage of particles at different standoff distances.....	40
Figure 2.17 Effect of particle Stokes number on particle conditions upon impact (using normalized velocity and diameter, $v_0=1800$ m/s and $D=7.88$ mm).....	40
Figure 2.18 Landing location, particle temperature, size and velocity on the substrate as a function of standoff distances.....	43
Figure 3.1 Geometry, boundary conditions, and computational mesh	50

Figure 3.2 The schematic representation of suspension breakup, vaporization, and particle agglomeration in the current model.....	54
Figure 3.3 Effect of suspension injection on the gas flow; (left) gas flow contours and (right) along centerline.....	59
Figure 3.4 Mass fraction of propylene, gaseous ethanol, and gaseous ethylene glycol inside the combustion chamber.....	60
Figure 3.5 Suspension/particle size, temperature, and velocity distributions within the computational domain	61
Figure 3.6 Comparison between the gas and particle characteristics along the centerline.....	63
Figure 3.7 Particle temperature and spatial distributions at different standoff distances (SD).....	64
Figure 3.8 Particle velocity and spatial distributions at different standoff distances (SD).....	65
Figure 3.9 Comparison between numerical and experimental [117] results for particle velocity at different standoff distances (SD)	68
Figure 3.10 Comparison between numerical and experimental [117] results for particle temperature at different standoff distances (SD)	68
Figure 4.1 Flowchart of the S-CLSVOF solver in OpenFOAM proposed by Albadawi <i>et al.</i> [68]	79
Figure 4.2 Computational domain and boundary conditions.....	81
Figure 4.3 Dynamic adaptive mesh refinement method; (a) the original mesh, (b) dynamic refined mesh of cells with α between 0.01 and 0.99, and (c) mesh refinement close-up	83
Figure 4.4 Prediction of liquid breakup and structure of ligaments and droplets (time=6 ms, $U_R=1$, $We=100$, and $q=20$) as a function of refinement levels; a) without refinement, b) with two refinement levels, c) with three refinement levels.....	84

Figure 4.5 Prediction of surface wavelength as a function of refinement levels (time=6 ms, $U_R=1$, $We=100$, and $q=20$)	85
Figure 4.6 Prediction of column breakup point location as a function of refinement levels (time=6 ms, $U_R=1$, $We=100$, and $q=20$)	85
Figure 4.7 Computational time as a function of refinement levels ($U_R=1$, $We=100$, and $q=20$)..	86
Figure 4.8 Predicted liquid structure for $We=50$, and different q and U_R	87
Figure 4.9 Predicted liquid structure for $We=100$, and different q and U_R	88
Figure 4.10 Predicted liquid structure for different We , q , and UR ; view from the incoming air direction.....	90
Figure 4.11 Surface wave structures and wavelengths for high UR cases; top right corner: view from the incoming air direction.....	91
Figure 4.12 Comparison of predicted liquid penetration height with the experimental observations [47]	93
Figure 4.13 Liquid penetration heights obtained from experimental data [47]	96
Figure 4.14 Comparison of the predicted liquid surface wavelength in the current study with the experimental [44, 46] and numerical [152, 153] results for the uniform crossflow; the effects of We and UR on liquid surface wavelength	98
Figure 4.15 Comparison of the predicted liquid surface wavelength in this study with the experimental [46] and numerical [153] results for the uniform crossflow; the effects of q and UR on liquid surface wavelength	99
Figure 4.16 Comparison of the predicted liquid jet dimension at onset of breakup with the experimental [44, 46] and numerical [152, 153] results for the uniform crossflow; the effects of We and UR on di	100

Figure 4.17 Comparison of the predicted liquid jet dimension at onset of breakup with the experimental [46] and numerical [153] results for the uniform crossflow; the effects of q and UR on d_i	101
Figure 4.18 Comparison of the liquid column breakup point location (in crossflow direction) predicted in the current study with the experimental [46], theoretical [149] and numerical [152, 153] results for the uniform crossflow; the effects of We and UR on x_b	102
Figure 4.19 Comparison of the liquid column breakup point location (in crossflow direction) predicted in this study with the experimental [46] and numerical [153] results for the uniform crossflow; the effects of q and UR on x_b	103
Figure 4.20 Comparison of the liquid column breakup point location (in direction of the liquid injection) predicted in the current study with the experimental, and theoretical results [149] for the uniform crossflow	104
Figure 5.1 Liquid (water) radial injection into the plasma plume	110
Figure 5.2 Instantaneous images of the interaction of a continuous water jet with dc plasma flow: a) water pressure=0.25 Mpa, b) water pressure=0.45 Mpa, c) water pressure=0.65 Mpa, d) breakup close-up [179]	113
Figure 5.3 Schematic of experimental setup.....	115
Figure 5.4 Configuration of liquid injector and air tube to study the water jets injection into transverse free air jets	116
Figure 5.5 Breakup of water jets in transverse free air jets: a) enhanced capillary breakup ($We = 2.5, q = 3.6$), b) bag breakup ($We = 6.7, q = 15$), c) multimode breakup ($We = 25, q = 28$), d) shear breakup ($We = 72, q = 9$), e) surface/column breakup ($We = 175, q = 8.2$)	119
Figure 5.6 Breakup regime map of liquid jets in transverse free air jets	121
Figure 5.7 The technique used to locate the column breakup point (CBP)	122

Figure 5.8 Location of the liquid column breakup point (CBP) as a function of gaseous Weber number and momentum flux ratio (based on the average gas velocity at the nozzle exit) for different values of Dd , and Hd	124
Figure 5.9 Location of the liquid column breakup point (CBP) as a function of Dd , and Hd ...	125
Figure 5.10 Comparison of the location of liquid column breakup point (CBP) obtained in this study with the results of Wu <i>et al.</i> [149]	126
Figure 5.11 Liquid penetration height (spray trajectory) as a function of liquid-to-gas momentum flux ratio, q	127
Figure 5.12 A series of captured images with time difference of 0.4 ms	129
Figure 5.13 Effect of axial distance between the liquid nozzle exit and the air tube on breakup mechanisms and penetration height: a) bag breakup ($We = 6.7, q = 5.6, H/d = 35, W/D = 3.75$), b) enhanced capillary breakup ($We = 6.7, q = 5.6, H/d = 35, W/D = 14.5$).....	130
Figure A.1 Schematic diagram of the problem of bubble growth and detachment	154
Figure A.2 Bubble shape predictions by experimental [68], VOF and S-CLSVOF for the problem of bubble growth and detachment	155

List of Tables

Table 2.1 Materials thermo-physical properties [95-98]	27
Table 3.1 Operating condition	50
Table 4.1 Values of Ux , α , Ux, u , Ux, avg , U_R , We , and q for various cases.....	82
Table 5.1 Gaseous Weber number to define breakup transition criteria for liquid jet in crossflow	118

Nomenclature

A	Projected area (m ²)
B_m	Spalding mass number
B_T	Spalding heat transfer number
c	Sound speed (m/s)
C	Specific heat (J/(kg.K))
C_D	Drag coefficient
d	Diameter (m)
D	Nozzle exit diameter (m)
d_s	Distance from the substrate (m)
d_i	Liquid jet dimension at the onset of drop formation (m)
e	Internal energy (J)
E	Total energy (J)
F_D	Drag force (N)
g	Gravitational acceleration (m/s ²)
G_k	Turbulent kinetic energy production
h	Heat transfer coefficient (W/(K.m ²))
H	Vertical distance between gas nozzle and liquid orifice (m)
h_{fg}	Latent heat of evaporation (J/kg)
H_v	Heaviside function
k	Turbulent kinetic energy
k_m	Mass transfer coefficient (m/s)
Kn	Knudsen number
L	Computational domain height (m)
m	Mass (kg)
M	Mach number
M_t	Turbulent Mach number
n	Face unit normal flux
p	Pressure (Pa)

Pr	Prandtl number
q	Momentum flux ratio
r	Radius (m)
Re	Reynolds number
S	Surface area (m ²)
SD	Standoff distance (m)
S_f	Cell face area vector
$sign$	Sign function
St	Stokes number
T	Temperature (K)
U	Velocity (m/s)
U_c	Vector of relative velocity normal to the interface
U_R	Velocity ratio
V	Velocity (m/s)
W	Axial distance between gas nozzle and liquid orifice (m)
We	Weber number
x	Coordinate direction and distance
x_b	Axial location of liquid column breakup point
y	Coordinate direction and distance
Y	Mass fraction
y_b	Vertical location of liquid column breakup point
Y_M	Dilatation dissipation
α	Volume fraction
β	Parameter defined in level set method
γ	Ratio of specific heats
δ	Dirac function
δ_b	Boundary layer thickness (m)
Δx	Mesh size (m)
ε	Viscous dissipation
κ	Interface curvature
λ	Thermal conductivity (W/(m.K))

λ_s	Liquid surface wavelength (m)
μ	Viscosity (kg/(m.s))
μ_t	Eddy viscosity (kg/(m.s))
ξ	Bulk viscosity (kg/(m.s))
ρ	Density (kg/m ³)
σ	Surface tension (N/m)
τ	Shear stress (kg/(m.s ²))
φ	Face volume flux
ϕ	Level set function
ϕ_0	Level set function before re-initialization
ψ	Compressibility (s ² /m ²)
ζ	Pseudo time used in level set re-initialization equation
<i>CBP</i>	Column breakup point
<i>CLSVOF</i>	Coupled level set and volume of fluid method
<i>HVOF</i>	High velocity oxygen fuel spray
<i>HVSFS</i>	High velocity suspension flame spraying
<i>KHRT</i>	Kelvin-Helmholtz Rayleigh-Taylor breakup model
<i>LES</i>	Large eddy simulation
<i>LS</i>	Level set method
<i>SCLSVOF</i>	Simple coupling of level set and volume of fluid methods
<i>SPS</i>	Suspension plasma spraying
<i>TAB</i>	Taylor analogy breakup model
<i>VOF</i>	Volume of fluid method

Subscripts

<i>a</i>	Bottom of the inlet boundary
<i>avg</i>	Average
<i>c</i>	Carrier gas
<i>d</i>	Droplet
<i>g</i>	Gas
<i>j</i>	Jet

<i>l</i>	Liquid
<i>p</i>	Particle
<i>sgs</i>	Sub-grid scale
<i>sub</i>	Substrate
<i>u</i>	Top of the inlet boundary
<i>x</i>	In axial direction

Chapter 1

“Some parts of this chapter is reprinted from the paper published in journal of Coatings, 2015, volume 5, pp. 576-645, [1], with permission”

Introduction

1.1 Overview

Thermal spraying is a process in which molten, semi-molten or solid particles are deposited on a substrate. Various thermal spray techniques such as atmospheric plasma spraying (APS), and high velocity oxygen fuel spraying (HVOF) are extensively used in industry to generate many different types of coatings such as thermal barrier, wear resistance, and corrosion resistance. As the coating particles are molten or solid and sufficiently fast in a stream of gas, they can plastically deform while impacting on the substrate which results in coating production. Obviously, the particle temperature and melting state and its kinetic energy have enormous influences on the coating properties. Therefore, the temperature, trajectory, and velocity of these fine particles must be well controlled to generate repeatable and desirable coatings [2-5].

The plasma torch usually consists of an anode made of copper and a cathode of thoriated tungsten (see Figure (1.1)). The plasma gas is heated up by the electric arc discharge and goes through a nozzle. Then, the gas typically expands in the atmosphere and forms a jet with Mach number around 0.6. The plasma gases are typically Ar, Ar+H₂, Ar+He, Ar+N₂, Ar+He+H₂, and Ar+He+N₂. It is worth mentioning that, Ar causes the arc inside the nozzle to be stabilized and the presence of He, H₂, and N₂ in the mixture results in the enhancement of heat transfer from gas to

particles. In a typical plasma torch, the gas temperature and velocity at the nozzle exit is around 14000K and 800 m/s, respectively. Using a carrier gas, the powder is usually injected into the jet radially. The powders are typically oxide ceramics in the range of 20-90 μm . The distance between the nozzle exit and the substrate is between 60 and 130 mm [2].

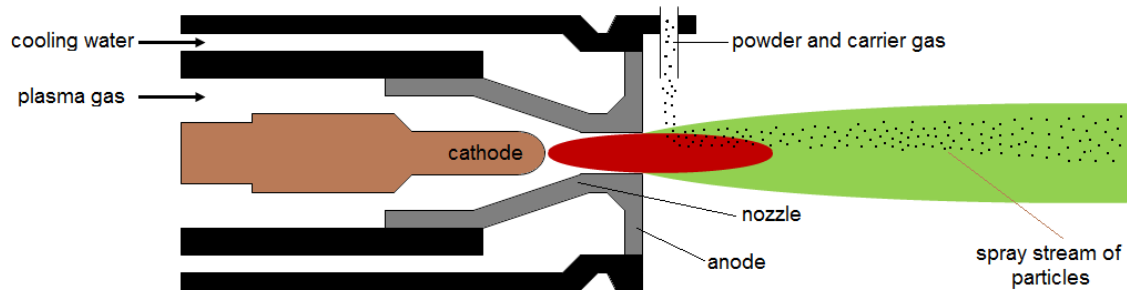


Figure 1.1 Schematic of a typical plasma torch

In a typical HVOF process, fuel (gas or liquid) and oxygen are injected into the combustion chamber and ignited. Then the exhaust gas goes through a nozzle and a supersonic jet is obtained which emerges into the surrounding air (see Figure (1.2)) [2]. The powder can be injected into the jet in radial or axial directions using a carrier gas which is usually nitrogen or argon [2]. The HVOF system can be used to spray metals, metallic alloys, cermets, ceramics, and polymers [2, 5-7]. However, particles are usually composites with carbide reinforcements, metals, and alloys, and are in the range of 5-45 μm [2]. Due to the nozzle geometry, chamber pressure and flame temperature, the particles in the HVOF process undergo high velocity (more than 500 m/s) and temperature in a way that their temperature reaches the melting point or above. The wire/rode is also applied in this technique to generate the molten particles. The end of wire/rode become molten in the flame and then atomized by compressed air to form droplets and these droplets accelerate toward the substrate. The distance between torch exit and the substrate is typically in the range of 150-300

mm [2]. Water, air or a mixture of both (hybrid) can be used for cooling the combustion chamber and the nozzle [1].

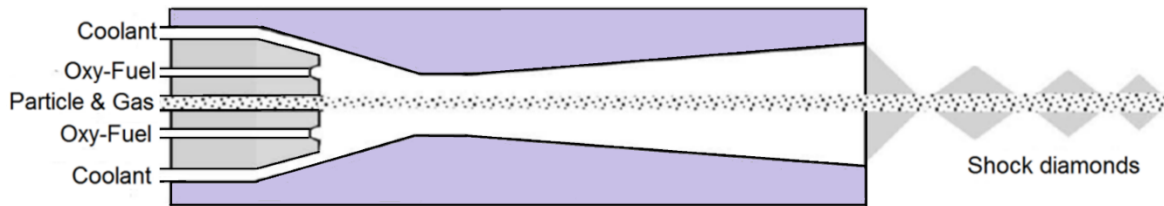


Figure 1.2 Schematic of a typical HVOF nozzle [1]

As fine microstructured coatings have great performance, coating with nano and submicron sized particles is the main trend in development of emerging thermal spray processes. There are various unique properties related to fine microstructured coatings such as enhanced catalytic behavior, noticeable superhydrophobicity behavior, remarkable wear resistance, superior thermal insulation and thermal shock resistance [1, 7]. Nevertheless, coating fine particles using conventional atmospheric thermal spray techniques is a difficult task to do, due to several reasons. The first reason is that nano and sub-micron particles usually form agglomerates which lead to clogging the feed lines. The second reason is the strong tracking of gas phase streamlines by the sub-micron particles. In other words, very fine particles decelerate and get diverted by the gas flow in the stagnation region near the substrate. The third reason is the easily distribution of nano scaled particles in air, which lead to their penetration in human skin or passing through the respiratory tract, the lungs and finally entering the blood circuit [1, 8].

To address the above mentioned issues, spraying suspension of fine solid particles is one of the best known techniques [7, 8]. A combination of fine solid particles (usually in the range 500nm-5 μ m) and a base liquid such as water or alcohol is known as suspension. To stabilize the suspension

(preventing particle agglomeration and sedimentation) a proper chemical stabilizers or surfactants are usually added to the system [8]. Suspension is commonly performed with the APS and HVOF techniques that are usually called as suspension plasma spraying (SPS) and high velocity suspension flame spraying (HVSFS). Instead of powder injection, suspension is injected into the jet/flame using spray atomization or injection of continuous jet methods (see Figure (1.3)) [9]. In addition, suspension can be injected into the jet radially or axially [7-10]. Figure (1.4) illustrates the radial injection of suspension into a plasma plume in more details. As can be seen, the spray field can be divided into three zones: 1) liquid jet, 2) disintegration of liquid column and formation of ligaments, 3) droplets [11]. In HVSFS process, axial injection of suspension into the combustion chamber is more common [10].

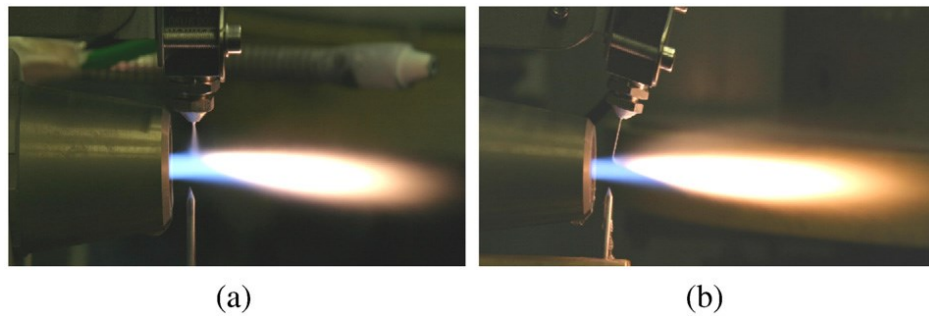


Figure 1.3 External radial injection of suspension into HVOF jet, (a) spray atomization and (b) mechanical injection (continuous jet) [9]

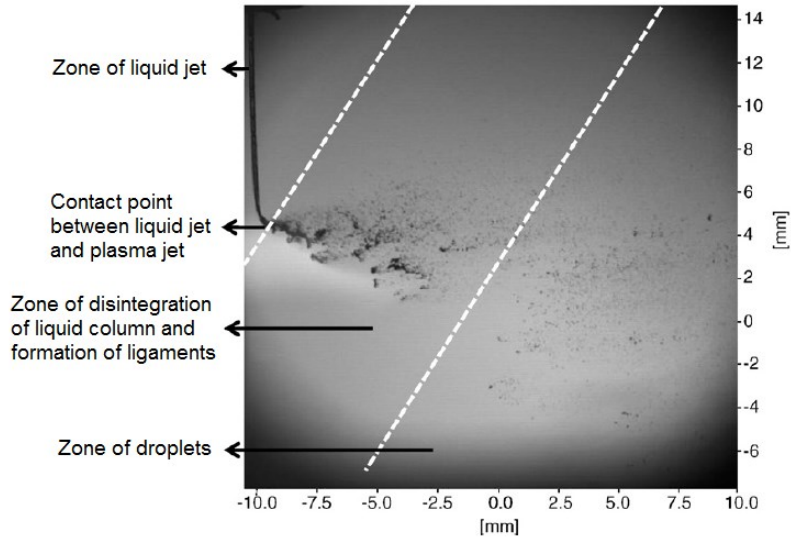


Figure 1.4 The cross-flow suspension atomization is divided into three zones; cylindrical liquid jet, disintegration of liquid column, and droplets [11]

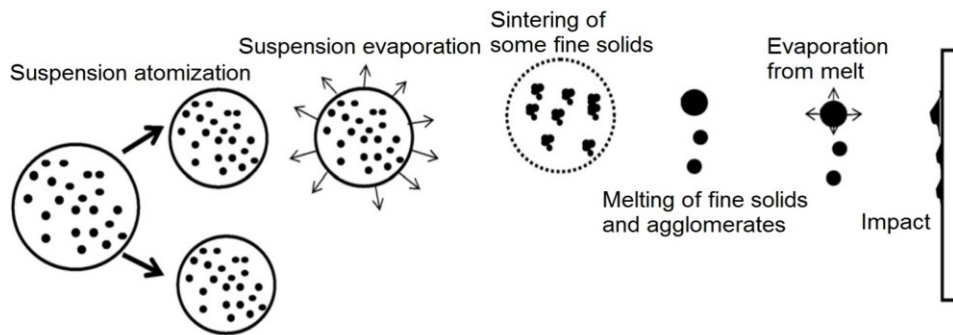


Figure 1.5 A schematic of a suspension droplet evolution in a high temperature jet or flame [8]

Figure (1.5) shows a schematic of the suspension droplet evolution in a high temperature jet or flame [8]. After suspension injection, the flame/jet atomizes the suspension (primary and secondary breakup) firstly and the liquid evaporation becomes dominant subsequently. Because of liquid evaporation, the solid particles or their agglomerations remain in the field and the flame/jet temperature decreases. Then, the particles are heated up by the flame/jet and accelerated toward

the substrate. It should be noted that the strong cooling of the hot gases by liquid vaporization and the very low inertia of particles implies very short spray distances [8, 12, 13].

It is clear that the coating quality obtained by the suspension spraying technique depends on the suspension penetration within the jet, the primary and secondary atomization of the suspension, and the slurry droplet evaporation/combustion [8, 12]. To control the above mentioned phenomena, the suspension characteristics such as density, specific heat, viscosity, surface tension, thermal conductivity and velocity as well as the main flow (i.e. jet/flame) properties, momentum, temperature, pressure, and turbulence should be known [1]. It should be noted that the mentioned that suspension properties strongly depend on the particle concentration, particle material, size and shape, base fluid material, surfactant/additives composition and concentration, suspension temperature, and acidity (pH) [14-17]. Moreover, the type, location, and angle of suspension injectors have significant influences on droplet size and velocity distributions, and consequently on the coating properties [9, 18, 19]. The significance of most of the mentioned parameters related to the coating properties have not been explored yet.

In a comprehensive article, the main phenomena involved in suspension thermal spray process (e.g. suspension properties, primary breakup, coaxial atomization, jet in crossflow, secondary breakup, evaporation, and etc.) have been reviewed [1]. It has been discussed that many parameters and mechanisms in the suspension spraying technique are still unknowns and must be understood to control and improve the coatings properties. It is obvious that both numerical and experimental studies should be performed to prepare a complete understanding of the key phenomena involved in this process. It is worth mentioning that suspension thermal spray simulation is more complicated than the modeling of conventional thermal spray processes because of the presence of some physical phenomena such as suspension atomization. Furthermore, experimental

measurement of in-flight particle parameters such as velocity, diameter, and temperature in suspension thermal spray conditions is more challenging due to smaller size of particles. In this thesis, the main focus is on the numerical modeling of suspension thermal spray process.

1.2 Numerical Methods and Previous Studies

Today, several numerical approaches are available to model the behavior of gas-particle/droplet flow such as Eulerian-Lagrangian model, Eulerian continuum approach (Eulerian-Eulerian model or two-fluid model), kinetic theory, and Ergun theory [20, 21]. In Eulerian-Lagrangian approach, the gas is modeled as a continuum phase while Lagrangian models are used to simulate the particles motion and heat transfer. This approach is suitable for dilute flow modeling [20, 21]. In Eulerian-Eulerian approach, all phases are assumed to be continuum and this method is suitable for dense flow modeling [22, 23]. The kinetic theory is used when the concentration of the particles is high so that the interparticle collisions become the dominant transport mechanism. This method assumes the particle as a molecule. The Ergun theory calculates the pressure drop in a packed bed [20]. It should be noted that the Eulerian-Eulerian and the Eulerian-Lagrangian approaches are used to model the thermal spray processes because the concentration of the particle phase is not too high in these systems. However, the Eulerian-Eulerian approach was only used by Dolatabadi *et al.* [24] and Samareh and Dolatabadi [25] to model the dense flow in HVOF and cold spray processes, respectively. This approach is not focused here.

As mentioned above, in Eulerian-Lagrangian approach, the particle phase is simulated by Lagrangian models while the gas phase is modeled as a continuum phase. The main force which controls the motion of the particles is drag. Moreover, if the particle is homogenous and the Biot number is less than 0.1, the lumped capacity method is used to model the particle heat transfer [20,

21]. It should be noted that Lagrangian models can be categorized as stochastic and deterministic models. The stochastic model considers the effect of gas turbulence on the particle motion and heat transfer; however the deterministic model neglects the gas turbulence effects. One-way coupled and two-way coupled are other assumptions used in this approach. In one-way coupled assumption, only the effect of one phase on the other is considered and there is no reverse effect [26-28]. In two-way coupled assumption, the effects of both phases on each other are considered. To model the gas phase, the equations of mass, momentum, species, and energy are solved [20, 21].

A comprehensive review of the Eulerian-Lagrangian approach is presented by the author [1]. Some empirical formulas for drag coefficient, thermophoretic force, and Nusselt number are described and the compressible form of the mass, momentum, species mass fractions, and internal energy equations of the gas phase are presented. Different models for reaction rate simulation such as the laminar finite rate model, the eddy dissipation model (EDM), and the finite-rate/eddy-dissipation model are discussed. In addition, large eddy simulation (LES), and Reynolds-averaged Navier-Stokes (RANS) turbulence models are explained in the paper. It is also discussed that to simulate the droplet secondary breakup, Taylor Analogy Breakup (TAB), Wave, and Kelvin-Helmholtz Rayleigh-Taylor (KHRT) models are typically used [29]. Therefore, for more details of Eulerian-Lagrangian approach and its formulation, the interested reader is referred to the author's review paper [1].

The Eulerian-Lagrangian approach has been used to model the HVSFS and SPS processes. In some preliminary works [30-32], the liquid part of suspension was considered only. For example, the effects of ethanol droplet size, flow rate and injection velocity on the gas phase and droplets vaporization in the HVSFS process were studied by Taleby and Hossainpour [30] and Gozali *et*

al. [31]. In the work of Taleby and Hossainpour [30], the premixed combustion of propane-oxygen, the non-premixed combustion of gaseous ethanol-oxygen, and the droplet evaporation were modeled. In this study, ethanol was injected axially into the chamber and the droplet breakup simulation was not included. Gozali *et al.* [31] employed the same approach and simulated the droplet secondary breakup. The droplets breakup for axial injections was modeled by TAB and for radial injections the wave model was used [31]. They revealed that neglecting modeling droplet breakup results in high order of errors. Gozali *et al.* [32] also developed their model [31] to consider the suspension feedstock as a mixture of water and ethanol. In the work of Dongmo *et al.* [33, 34], suspension was considered as two separate parcels: droplet (ethanol) and particle (titania) parcels, where each parcel was injected into the combustion chamber of HVOF system axially. They showed that the injection angle variation has significant influence on the ethanol residence time and evaporation length in the combustion chamber. Furthermore, by changing the straight geometry of the combustion chamber to a conical shape, they achieved good results regarding the micron and nano particles trajectories in the combustion chamber.

Jabbari *et al.* [19] used a two-component mixture model for simulating the suspension with a given particle concentration as a slurry droplet. The main goal was to mimic the suspension breakup, vaporization, particle temperature, velocity and trajectory in the suspension plasma spraying. The first component was the base fluid (e.g. ethanol), and the second component was considered to have the same properties as nickel (density, evaporation temperature, latent heat of evaporation, and etc.). To determine the coating particles characteristics, the suspended particles were tracked after completion of the suspension breakup and vaporization. This model was used by Jadidi *et al.* [35] and Pourang *et al.* [36] to investigate the effect of substrate shape and curvature on in-flight particle velocity, temperature and trajectory in suspension plasma spraying.

As mentioned above, the breakup process has significant influences on the droplet/particle in-flight behavior in suspension thermal sprays. It should be noted that the above mentioned breakup models (i.e. TAB, Wave, and KHRT) ignore some main features of breakup process such as liquid/suspension column deformation and ligaments formation. Furthermore, it is very difficult to experimentally measure the spray properties such as the droplet size distribution and penetration height in thermal spray conditions. Therefore, using interface tracking/capturing methods such as Volume of Fluid (VOF) is very helpful to predict the spray properties, penetration height, and column deformation. In some preliminary works [37-39], the VOF method was applied to model the penetration of water in the plasma plume and characterize the penetration height.

By a quick glance at the primary breakup section of suspension plasma spray process (see Figure (1.6)), one could find that the gas flow nonuniformity and the perturbations on the cylindrical suspension/liquid jet might have significant influences on the breakup mechanisms, spray trajectory, ligament formation, and final droplet size distribution. In this thesis, the effects of crossflow nonuniformity and suspension/liquid column perturbations on the primary breakup, have been fundamentally studied. In other words, numerical simulations (using VOF method) and experimental studies (using shadowgraphy technique) are performed to analyze the effects of crossflow nonuniformity and suspension/liquid column perturbations on the primary breakup, respectively. In this case, the dominant parameters on the breakup mechanisms, column breakup point, and penetration height can be discussed in more details. It should be noted that, this approach (separating different parameters and analyzing their effects individually) is also used by many researchers in the field of propulsion to study the behavior of liquid jet in crossflow [40-50].

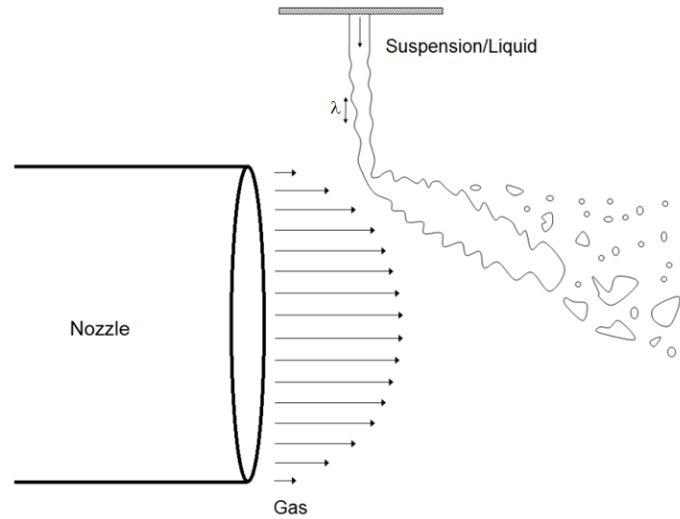


Figure 1.6 A schematic view of suspension/liquid injected into non-uniform cross-flow in thermal spray systems

In VOF method, one set of the Navier-Stokes equations is solved for both liquid and gas phases [51-53]. The surface tension force is usually included in the momentum equation as the continuum surface force and it depends on the interface curvature [54]. In this method, the interface location, curvature and its normal are calculated implicitly from an indicator function. A function (α) which represents the fractional volume of the cell occupied by liquid is defined where $\alpha=1$ and $\alpha=0$ correspond to a cell full of liquid and an empty cell (e.g. a cell full of gas), respectively. Therefore, a cell with α value between zero and one or a full cell which has at least one neighboring empty cell is known as a surface cell (see Figure (1.7)) [51-53].

0	0	0	0	0
0.32	0.6	0.35	0.1	0
1	1	1	0.77	0.18
1	1	1	1	0.42
1	1	1	1	0.58

Figure 1.7 Function α which represents the fractional volume of the cell occupied by liquid [1]

It should be noted that mass conservation is the main advantage of VOF method [55]. Moreover, the VOF method is able to model large density ratio multiphase flows accurately if the momentum equation in conservative form is solved and both momentum and mass are transported in exactly the same discrete manner [55, 56]. Grid dependency is one of the main drawbacks of this method. In addition, interface diffusion is another disadvantage of this method and it is caused by naive advection of discontinuous (Heaviside) VOF function (α) [55, 57]. All the suggested methods to alleviate this issue can be categorized into two classes; geometric and algebraic advection of VOF function [55]. The geometric reconstruction methods prevent the numerical diffusion, however, they increase the computational expenses [57, 58]. In addition, implementing these methods in higher dimensions and unstructured grids is very challenging. Although geometric reconstruction methods predict a sharp interface over a one cell width, discontinuous nature of VOF (Heaviside) function makes the estimation of interface curvature very difficult [55, 59]. Therefore, some algorithms for smoothing the VOF function (i.e. using smoothing kernels) and/or combining the VOF method with a height function (i.e. using a local height function) have been suggested [59]. However, it is indicated by many authors that these algorithms produce significant errors in poorly resolved or high-curvature regions [60, 61]. In algebraic methods the

interface reconstruction is avoided. Therefore, these methods are simple and computationally less expensive. However, algebraic methods cannot predict the interface precisely because the interface is spread over three to four cells [55, 58, 62].

Another drawback associated with VOF methods is the generation of spurious currents and unphysical vortices around the interface only due to numerical errors [55]. Lack of a discrete balance between surface tension force and pressure gradient, and inaccurate interface curvature are the main sources of spurious currents [55, 63]. It should be noted that the former relates to consistency of the solver formulation and the latter relates to the choice of interface capturing methodology [55, 63]. It is also worth mentioning that although the generation of spurious currents is an important issue for flows with low Weber number, it does not have significant effects on the flows with high Weber number [55].

Among different types of VOF codes that are used to simulate multiphase flows, free open source VOF solvers named `interFoam` and `compressibleinterFoam`, which are parts of OpenFOAM software [64], have been receiving an increased amount of usage and attention. In addition, the OpenFOAM software is very attractive for research because of many useful features such as ease of turbulence modeling, parallelization, and availability of wide range of spatial and temporal discretization schemes, boundary conditions, and wall functions. The `interFoam` and `compressibleinterFoam` solvers are used to model the gas-liquid two-phase incompressible and compressible flows, respectively. The volume fraction equations in these solvers include a compression term to mitigate the numerical diffusion [55, 64-66]. In other words, `interFoam` and `compressibleinterFoam` employ an algebraic advection method for mitigating the numerical diffusion. In the Ph.D. thesis of Rusche [67] supplementary details of implementation of the

interFoam solver in OpenFOAM can be found. The OpenFOAM software is used in the current study to capture the spray trajectory and penetration height.

The mass conservation is excellent in the interFoam and compressibleinterFoam solvers [55]. It is also revealed that inertia-dominated (high Weber number) flows with large density ratio are simulated very accurately by this solver [55]. On the other hand, for flows with low Weber number where surface tension force is important and interface curvature must be calculated accurately, these solvers do not result in a good agreement with analytical and experimental data [55, 66, 68]. Furthermore, similar to the most of VOF algorithms, the mentioned solvers suffer from spurious currents problem. Deshpande *et al.* [55] found that pressure-surface tension formulation is consistent in VOF solvers in OpenFOAM and the main reason of spurious currents is the inaccurate interface curvature.

Recently, coupled Level Set and Volume of Fluid (CLSVOF) method [69-71] has attracted many attentions. In Level Set (LS) method, the interface location and curvature are calculated from a smooth function called level set function (ϕ). The interface is captured by the zero level set, while the negative and positive values of ϕ define gas and liquid regions, respectively [72]. It is proven that mass loss is the main disadvantage of the LS method [70]. However, the precise capturing and evaluation of the curvature of the free surface is the main advantage of the LS method [70, 72]. In addition, as mentioned above, mass conservation and handling large density ratios are the main advantages of VOF method and inaccurate interface curvature is the main drawback of VOF method. It is clear that by coupling of level set and volume of fluid methods (CLSVOF), the mass conservation property of VOF can be combined with the interface smoothness property of LS [69-71]. Different algorithms for coupling of LS and VOF methods have been suggested [69-71]. However, we focus on the work of Albadawi *et al.* [68] since it is

based on the incompressible VOF solver in OpenFOAM. In this algorithm, the volume fraction (α) equation is only solved and the level set function is initialized by the advected volume fraction (α) in each time step. The surface tension force and interface curvature are calculated based on the LS function. It should be noted that, as mentioned above, the suspension/liquid phase interacts with a compressible gas medium in thermal spray systems. Therefore, a simple coupling of LS and VOF methods with application to compressible gas-liquid two-phase flow is presented in the current study. In general, in comparison with VOF method, in CLSVOF we have less spurious currents and more accurate interface normal and curvature.

1.3 Objectives

As mentioned, the particle temperature and melting state and the particle kinetic energy have enormous influence on the coating properties. Therefore, the temperature, trajectory, and velocity of these fine particles must be understood to generate controllable and repeatable coatings, and to improve the coating properties. The first objective of this study is to prepare a model to estimate the in-flight droplet/particle behavior in the suspension thermal sprays. The model should be able to consider the suspension properties, suspension breakup, liquid evaporation/combustion, particle motion and heat transfer, and compressible turbulent gas flows. Having this model, one can investigate the effect of different parameters such as standoff distance, suspension mass flow rate, injection angle, and gas flow velocity and temperature on the coatings properties and deposition rate.

The second objective of this work is to study the suspension primary breakup in plasma crossflow in more details. As discussed above, there are some reasons for choosing this goal; i) radial and external injection of suspension into the plasma plume is the most popular technique

among different suspension thermal spray techniques, ii) it is known from the model explained in the previous paragraph that when particles move near the plasma jet centerline, particle temperature, velocity and chance of particle deposition on the substrate increase. It is clear that suspension column deformation and primary breakup mainly controls the droplets/particles trajectories and, therefore, they should be studied in more details, and iii) it is shown by many researchers (e.g. see [19]) that the typical TAB and KHRT models are not able to precisely simulate spray trajectory and penetration height. Therefore, interface capturing/tracking numerical approaches such as VOF together with experimental studies are needed to analyze the suspension/liquid primary breakup and to improve the accuracy of TAB and KHRT models. To achieve the second objective of this study the following steps are considered:

1. Investigating the behavior of liquid jets in nonuniform crossflows using VOF method and developing a general correlation for liquid penetration height as a function of crossflow velocity profile,
2. Experimental study (using shadowgraphy technique) of the effects of liquid column perturbations on the breakup physics, liquid penetration height, and column breakup point, and developing general correlations for these parameters as a function of liquid-gas momentum flux ratio and the distance between gas nozzle exit and liquid orifice,
3. Coupling of Level Set (LS) and compressible Volume-of-Fluid (VOF) methods to improve the interface curvature computation, and validating the code by running the benchmark tests.

1.4 Thesis Layout

This thesis is organized in a manuscript-based format to study the suspension and particle transport in thermal spray processes. In chapter 2, an Eulerian-Lagrangian approach is explained to model the suspension breakup, liquid evaporation, and particle in-flight behavior in suspension plasma sprays. In this model, suspension is considered as a two-component mixture of ethanol and nickel, and substrate is included in the computational domain. In chapter 3, using Eulerian-Lagrangian approach, the suspension behavior in HVOF process is modelled. In this study, suspension is considered as a three-component mixture of ethanol, ethylene glycol, and mullite. In addition, premixed combustion of propylene-oxygen and non-premixed combustion of ethanol-oxygen and ethylene glycol-oxygen are modeled. In chapter 4, the behavior of liquid jet in nonuniform crossflow is numerically studied. The results of this chapter, especially the developed correlation for the liquid penetration height, are very useful for estimating the spray trajectory in SPS technique. In chapter 5, the experimental setup and the shadowgraphy techniques applied to investigate the effects of liquid column perturbations on the breakup physics are explained. The outcomes of this chapter can be used to estimate the breakup mechanisms in SPS technique. In appendix, the implementation of coupled LS and compressible VOF method in OpenFOAM is discussed and the code is validated against experimental data. This code can be used to model gas-liquid two-phase flows with different compressibilities.

Chapter 2

A Three-Dimensional Analysis of the Suspension Plasma Spray Impinging on a Flat Substrate

“Reprinted from the paper published in Journal of Thermal Spray Technology, 2015, volume 24, pp. 11-23, [35], with permission”

Abstract

Suspension feedstock in plasma spraying is an emerging process for producing coatings with enhanced characteristics. Sub-micron up to few micron-sized particles are suspended in a liquid and injected into the plasma plume. After suspension's breakup and evaporation, molten and semi-molten fine particles are deposited on a substrate. Particle conditions upon impact (i.e. trajectory, velocity, and temperature) as well as substrate location and shape have key influences on the adhesion and quality of the coatings. In the current study, a three dimensional two-way coupled Eulerian-Lagrangian approach is used to model the plasma jet, droplet/particle trajectory, velocity, and temperature. To model the turbulence and the effect of substrate on the flow field, Reynolds Stress Model (RSM) is used. In addition, Kelvin-Helmholtz Rayleigh-Taylor (KHRT) breakup model is employed to predict the secondary breakup of the suspension. The focus of this work is on the particles behavior near the substrate. Flat substrates placed at standoff distances ranging from 40 to 60 mm are

modeled to provide detailed information on the coating particles upon impact using suspension plasma spraying.

2.1 Introduction

The main trend in developing the emerging thermal spray processes, is coating with nano and submicron sized particles due to the superior performance of fine microstructured coatings. Fine microstructured coatings demonstrate various unique properties, such as remarkable wear resistance, enhanced catalytic behaviour, superior thermal insulation and thermal shock resistance [7]. However, due to the following two main reasons it is difficult to coat fine particles using conventional thermal spray techniques. The first reason is clogging in the feed lines owing to the agglomeration of nano and sub-micron particles. The second reason is that while the jet is impinging on a substrate, fine particles decelerate and get diverted by the flow in the stagnation region. One of the most common techniques to address the above mentioned issues is spraying fine solid particles suspensions. In this technique, instead of powder injection, suspension of nano/submicron sized particles in a base fluid is radially or axially injected into the hot jets and flames [73]. The base fluid is typically water, ethanol or the mixture of both [73].

In suspension plasma spray (SPS) technique, the suspension is usually injected into the plasma plume radially. Injecting nano/submicron particles by a liquid provides enough momentum for the particles to penetrate the rapid plasma jet. There are different parameters that can affect coating properties in SPS such as torch operating conditions, arc root fluctuations, the droplet size, breakup and vaporization, melting and acceleration of the particles. Fazilleau *et al.* [12] showed that suspension atomization by the plasma plume occurs before the domination of the droplet vaporization process. It was demonstrated that Weber number is high in the plasma core and the

catastrophic breakup happens. In the catastrophic breakup regime both Rayleigh-Taylor and Kelvin-Helmholtz waves exist. Afterwards, the plasma is cooled down by vaporization process of the suspension and the particles or their agglomerates are set free. Heating up and acceleration of these particles then occur inside the plasma jet.

In the past few years, a number of numerical studies were dedicated to the simulation of interaction between suspension and the plasma plume. Vincent *et al.* [38] used volume of fluid (VOF) method to simulate the penetration of continuous water jet in an Ar-H₂ plasma flow. In addition, the authors developed their model to display the continuous water jet primary fragmentation into large drops [74]. Noting that, the effect of phase change on the water was not included in [38, 74]. In ref. [39] the secondary atomization of droplets in the plasma plume was simulated by volume of fluid method. Authors modeled the first instant of droplet interaction with a plasma jet [39]. Eulerian-Lagrangian approach was used by Shan *et al.* [75] to simulate the droplet breakup and collision in the solution precursor plasma spraying. The gas flow, droplet breakup, and droplet collision were simulated by the RNG k - ϵ , Taylor analogy breakup (TAB), and O'Rourke's models, respectively [75]. It was concluded that the droplet collision increases the average droplet size of the spray and the droplet breakup results in the reduction of the average droplet size of the spray. Based on their results, both droplet collision and breakup should be considered in the simulation [75]. Marchand *et al.* [37, 76] studied the effect of plasma jet fluctuations on liquid feedstock injection. They used water and concluded that penetration and breakup processes are influenced by many factors such as droplet size, relative velocity between the droplets and the main flow and droplet surface tension. However, the droplet evaporation was not considered in their studies [37, 76]. Jabbari *et al.* [19] proposed a model to mimic the suspension atomization, evaporation, particle trajectory, velocity, and temperature. Kelvin-

Helmholtz Rayleigh-Taylor (KHRT) breakup model was used to model the breakup of droplets. When the breakup and evaporation of suspension was complete, the suspended particles were tracked through the domain to determine the characteristics of the coating particles. It was shown that the suspension penetration depth, the particles velocity and temperature are higher if the suspension injector is near the gun exit and its angle is toward the gun. It was indicated that the penetration depth increases with suspension injection velocity. In their study, the substrate was not included in the computational domain.

Obviously, the presence of a cooled substrate in front of the plasma jet has considerable effects on both gas and particle behaviour [77, 78]. As shown experimentally in [77], when a cooled substrate is placed at various standoff distances of 80-120 mm, the centerline temperature of argon-hydrogen plasma jet is increased by around 12% at 5 mm elevation from the substrate, and by about 22% at the substrate location. Kang *et al.* [78] also studied the effect of presence of a flat substrate on the plasma flow field and the behaviour of the Zirconia particles near the substrate. The particle diameter was 22-125 μm and the standoff distance was 80 mm. It was described that although the substrate presence considerably impacts the plasma flow fields at substrate vicinity, no sudden change in particles trajectories was observed before impacting the substrate. Furthermore, it was shown that with the presence of a substrate, smaller particles are more exposed to the flow change.

To understand the involved physical phenomena in the plasma-substrate interaction, reviewing the impinging jets is very helpful. Impinging jets (Figure (2.1)) are widely used in industry to transfer energy or mass. In an impinging jet, as the gas approaches the substrate, its axial velocity decreases and the flow turns. This region is called stagnation or deceleration region. As the axial velocity decreases, the static pressure on the substrate increases. After turning, the gas

enters a wall jet region where it moves laterally outward parallel to the substrate [79, 80]. The onset of the boundary layer within the wall jet is in the stagnation region, where it usually has a thickness of no more than 1% of the jet diameter [81]. In order to study two-phase gas-particle impinging jets and to describe the particle behavior near the substrate, Stokes number is used. Stokes number, ($St = \rho_p d_p^2 U_g / 18 \mu D$), is a ratio of the particle's inertia and the fluid drag on the particle where ρ_p , d_p , U_g , μ , D , are particle density, particle diameter, the average exit velocity of the jet, gas viscosity and the impingement hole diameter, respectively [82-86]. Consequently, a particle with a low Stokes number tracks the flow field while a particle with a high Stokes number follows its own trajectory and is less affected by the flow field.

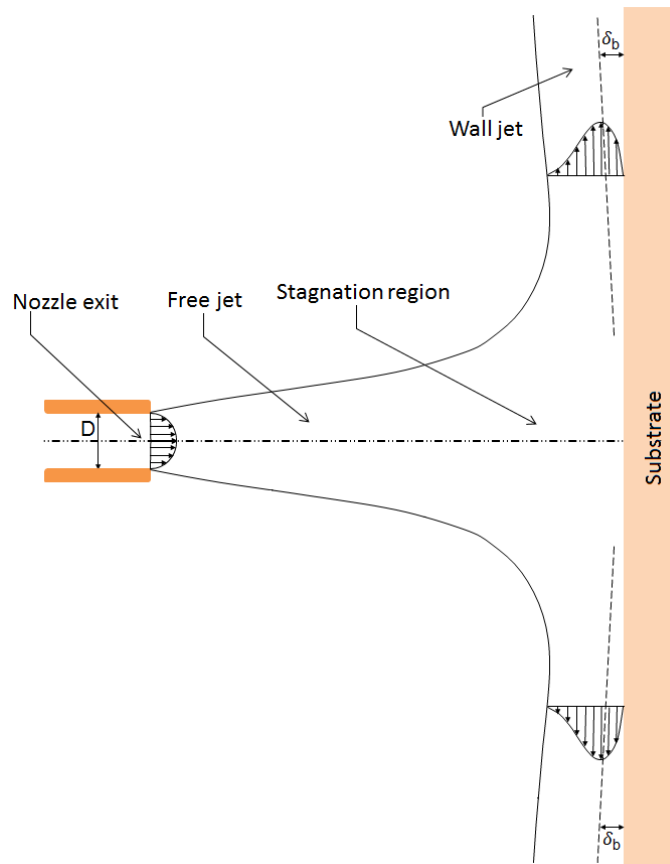


Figure 2.1 The schematic of a typical impinging gas-jet system

The motivation of the present work comes from the interest to use suspension plasma spraying of nickel and nickel oxide particles for improving electrocatalytic performance of nickel electrodes by producing a textured porous coating [87, 88]. As described in detail in ref. [87], nickel powder particles with ethanol as the base fluid are injected radially into the jet of a 3 MB Sulzer plasma gun. In the current study, the suspension penetration, atomization, evaporation, droplet/particle trajectory, velocity and temperature, are numerically investigated. The focus of this work is on particles behavior near the substrate (Figure (2.2)). Flat substrates placed at standoff distances (SD) ranging from 40 to 60 mm are considered to provide comprehensive understanding of the particles coating in suspension plasma spraying. It should be noted that in SPS technique, sub-micron up to few micron sized particles are used. These fine particles are very sensitive to the flow change and can strongly follow the gas phase streamlines. In addition, the standoff distance in SPS technique is less than that in the case of dry powder injection [13]. Therefore, in SPS technique, the presence of substrate has serious influences on plasma jet and particle behavior and needs to be well understood.

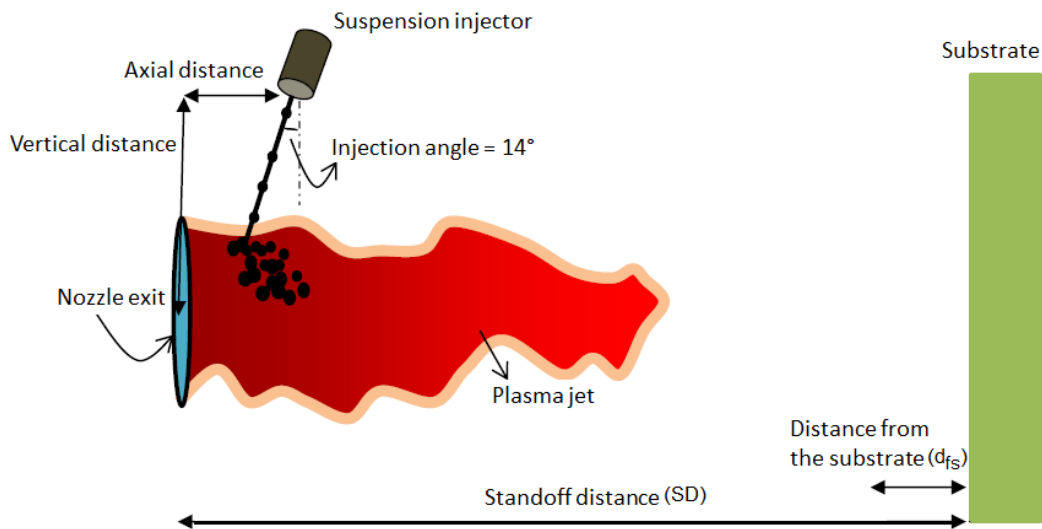


Figure 2.2 The schematic of suspension injection into a plasma plume

2.2 Mathematical Modeling

In this study, by using ANSYS®-Fluent® release 14, the Eulerian-Lagrangian approach with two-way coupling assumption is applied. The mathematical modeling was described in detail in ref. [19], and only the main assumptions are briefly reviewed here. To model the turbulent plasma flow; Reynolds Stress Model (RSM) is applied. It is demonstrated that, in comparison with $k-\varepsilon$ models, RSM yields more realistic results for simulating the high temperature zone in the plasma jet and it shows better agreement with the experimental and numerical results in the literature [19, 89]. Additionally, Reynolds stress model usually presents superior results especially for the swirling flows, and flows with large streamline curvature [29]. The steady mode is considered in order to reduce the effects of plasma jet fluctuations on drops fragmentation. Hence, argon is considered as the working gas [74]. The ideal gas model is used and the transport and thermodynamic properties of the gas phase are temperature dependent only [90]. To model the plasma jet, local thermal equilibrium (LTE) is presumed by providing velocity and temperature profiles at the nozzle exit [91, 92]. The temperature profile is assumed to be uniform and equal to 12,250 K. In addition, the velocity profile correlation is given as follows

$$v = v_0 \left[1 - \left(\frac{2r}{D} \right)^2 \right] \quad \text{Equation 2.1}$$

where $v_0=1800$ m/s and r is the nozzle exit radius [91, 92]. The data available in [93] is used for calculating the gas phase thermo-physical properties (i.e. viscosity).

Similar to the approach used in our previous study [19], a two-component mixture model for simulating nickel suspension with a given concentration (here 15 wt. %) is used. Ethanol is one of the components and the second one carries nickel properties like density, evaporation temperature, and latent heat of evaporation. The assumptions made in the present work are demonstrated schematically in Figure (2.3). Droplet surface tension is estimated by using a piecewise-linear

function. The suspension bulk surface tension is used as long as suspension temperature is less than or equal to the evaporation point of ethanol and as far as the breakup process is dominant. Fine droplets are produced subsequently and the breakup processes are stopped. However, the ethanol evaporation remains ongoing until all ethanol evaporates. For the next step, molten nickel surface tension which is higher than suspension surface tension is used [19]. It is considered that there is a discrete injector, with the diameter of 0.2 mm that is composed of ten droplets with Rosin-Rammler size distribution [94]. The droplet size distribution and a schematic diagram of the discrete injector are depicted in Figure (2.4). The mass flow rate of droplet injection into the plasma plume is adjusted to be 0.52 g/s based on the results of the experimental study [87]. The suspension velocity is set to 18 m/s according to the suspension mass flow rate and density. The injector angle is 14° which has been selected based on the results in our previous study [19]. The stochastic tracking model is assumed to account for the gas turbulence effect on the particle trajectory.

The suspension atomization (secondary breakup) is simulated using Kelvin-Helmholtz Rayleigh-Taylor (KHRT) breakup model. This model is applicable when the Weber number is high and the catastrophic breakup occurs [29]. As mentioned earlier, Fazilleau *et al.* [12] explained that in the plasma core the catastrophic breakup happens. Thus, compared to other breakup models such as Taylor analogy breakup (TAB), the KHRT is a better model to simulate the suspension breakup inside the plasma sprays. Moreover, the droplet collision is simulated by O'Rourke's model [19, 29, 75] which was used by Shan *et al.* [75] to simulate the droplet collision in the solution precursor plasma spraying.

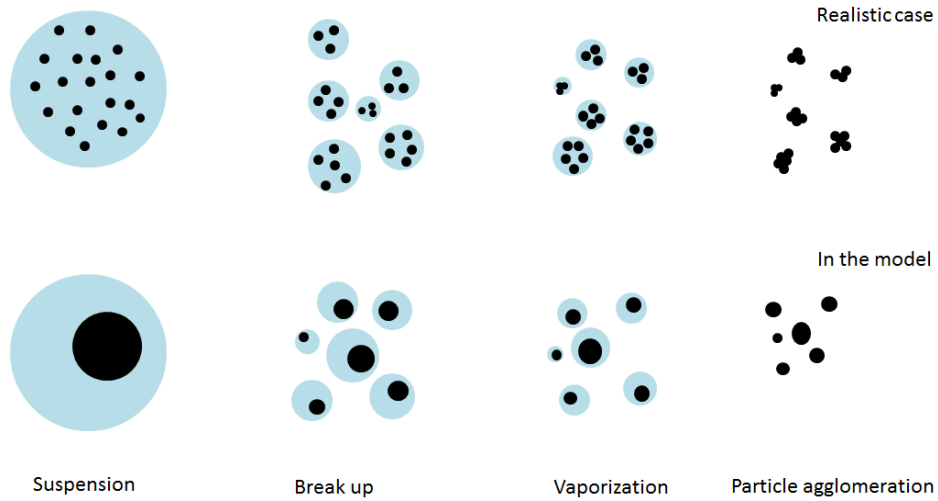


Figure 2.3 The suspension atomization, evaporation and particle agglomeration in the realistic and the model cases [19]

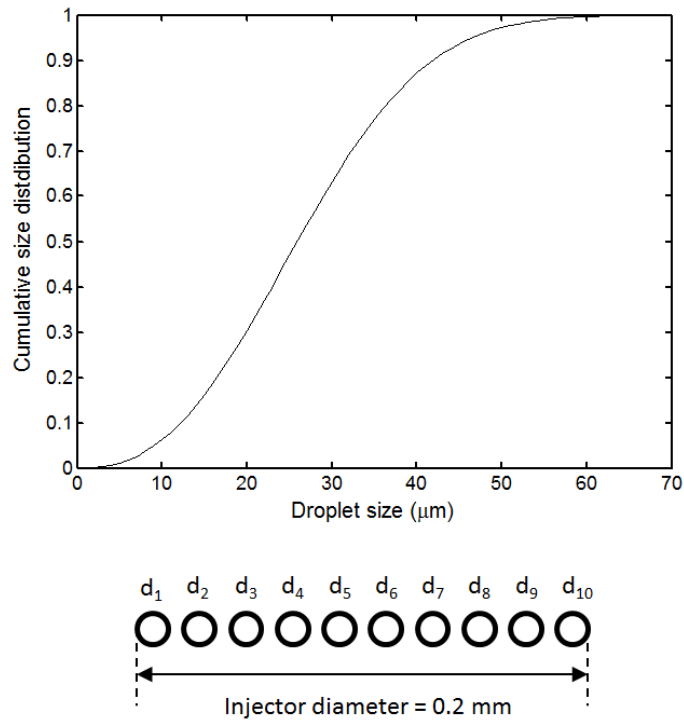


Figure 2.4 The droplet size distribution injected into the plasma jet as well as a schematic diagram of the discrete injector

For the suspension phase momentum, conservation equation is used which consists of the drag force. The drag coefficient is derived from the following correlation

$$C_D = a_1 + \frac{a_2}{Re} + \frac{a_3}{Re^2} \quad \text{Equation 2.2}$$

where Re is the Reynolds number and a_1 , a_2 and a_3 are constants [19, 29, 78]. To model the heat transfer of the suspension phase, lumped capacity method is used. The Nusselt number is calculated based on the Ranz-Marshall correlation [29]. In addition, the particle specific heat is defined as a function of temperature so that the particle melting process can be modeled. Particle melting approximation is completely explained in our previous paper [19]. The thermo-physical properties of particle/droplet materials are presented in Table (2.1).

Table 2.1 Materials thermo-physical properties [95-98]

Property	Units	Molten Nickel	Ethanol
Melting point	K	1728	-
Boiling point	K	3200	351
Density	$kg\ m^{-3}$	7850	789
Viscosity ($\times 10^3$)	$Pa\ s$	5.5	1.2
Surface tension	$N\ m^{-1}$	1.778	0.0223
Specific heat	$J\ kg^{-1}\ K^{-1}$	735	2470
Latent heat of fusion ($\times 10^5$)	$J\ kg^{-1}$	2.92	-

As mentioned above, our previous work was conducted with the elimination of substrate in the computational domain. The 3D geometry in this paper consists of the substrate and the free space in front of the nozzle which is for the plasma plume (Figure (2.5)). In order to capture the large temperature and velocity gradients both in axial and radial directions, the mesh is fine at core region of the jet and near the substrate. Locations of the flat substrates are at various standoff distances such as 40, 50 and 60 mm from the torch and perpendicular to the torch axis. The flat substrates have a thickness of 5 mm with a surface area of $25 \times 25\ mm^2$.

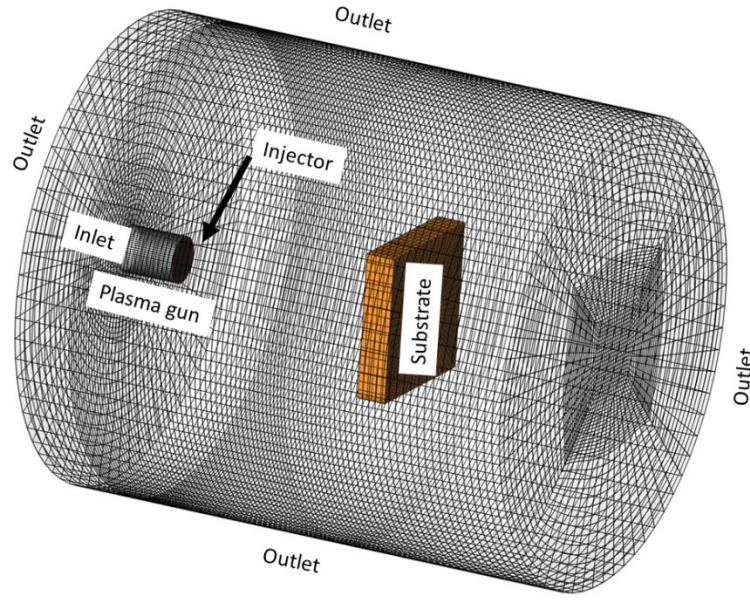


Figure 2.5 Computational domain for the jet simulation

No-slip boundary condition is imposed on the substrate and scalable wall function is used to model the velocity boundary layer on the substrate. It should be noted that, in ANSYS-Fluent[®] 14 [29], the wall laws (wall functions for turbulence modeling) are based on the wall unit, y^* , rather than y^+ . y^* is defined as $y^* = \rho C_\mu^{1/4} k^{1/2} y / \mu$ where μ , ρ , y , k , C_μ are the gas viscosity, density, distance from the wall, turbulent kinetic energy near the wall, and a constant (≈ 0.09), respectively. In the current study, scalable wall function is used to avoid the deterioration of standard wall functions under grid refinement below $y^* < 11$. Consistent results are produced by this wall function for grids of arbitrary refinement. The standard wall functions are identical for grids coarser than $y^* > 11$. Scalable wall functions are used to force the usage of the log-law in conjunction with the standard wall functions approach. This is obtained by introducing a limit in the y^* computations such that $\tilde{y}^* = \max(y^*, 11.225)$ [29]. It should be noted that as the focus of the present work is not on modeling of the heat flux from the plasma jet to the substrate, adiabatic boundary condition is applied at the substrate. The adiabatic assumption is acceptable when the

interaction time between plasma jet and the substrate is very small. Furthermore, the trap boundary condition was used to model the particle-substrate interaction. In other words, when particles strike on the substrate, they stick on it.

2.3 Results and Discussions

Extensive validation of the plasma jet, the employed turbulence model, the discrete phase and the breakup models is achieved in previous studies; therefore it is not repeated here [19, 75, 89]. Instead, the effect of flat substrate position on the gas and the particle phases is discussed in this paper in more details. Particle trajectory, velocity and temperature near the substrate are analyzed and the porosity of the coatings as a function of standoff distance is discussed. The total time of suspension injection for all cases in this paper is 20 ms.

The effect of the substrate existence on the gas velocity is compared with the free jet case without suspension injection in Figure (2.6-a). It is clear that as the gas approaches the substrate, its axial velocity decreases and as a result the static pressure on the substrate increases. An axisymmetric stagnation flow is formed on the substrate for the cases without suspension injection (Figure (2.6-a)). In addition, by increasing the standoff distance, the magnitude of the radial and axial velocities near the substrate decreases. Additionally, as displayed in Figure (2.6-b) the plasma velocity decreases due to the momentum exchange of the suspension cross-flow where the suspension penetrates. Consequently, the stagnation flow formed on the substrate is weaker in the case of suspension injection compared to the no injection case.

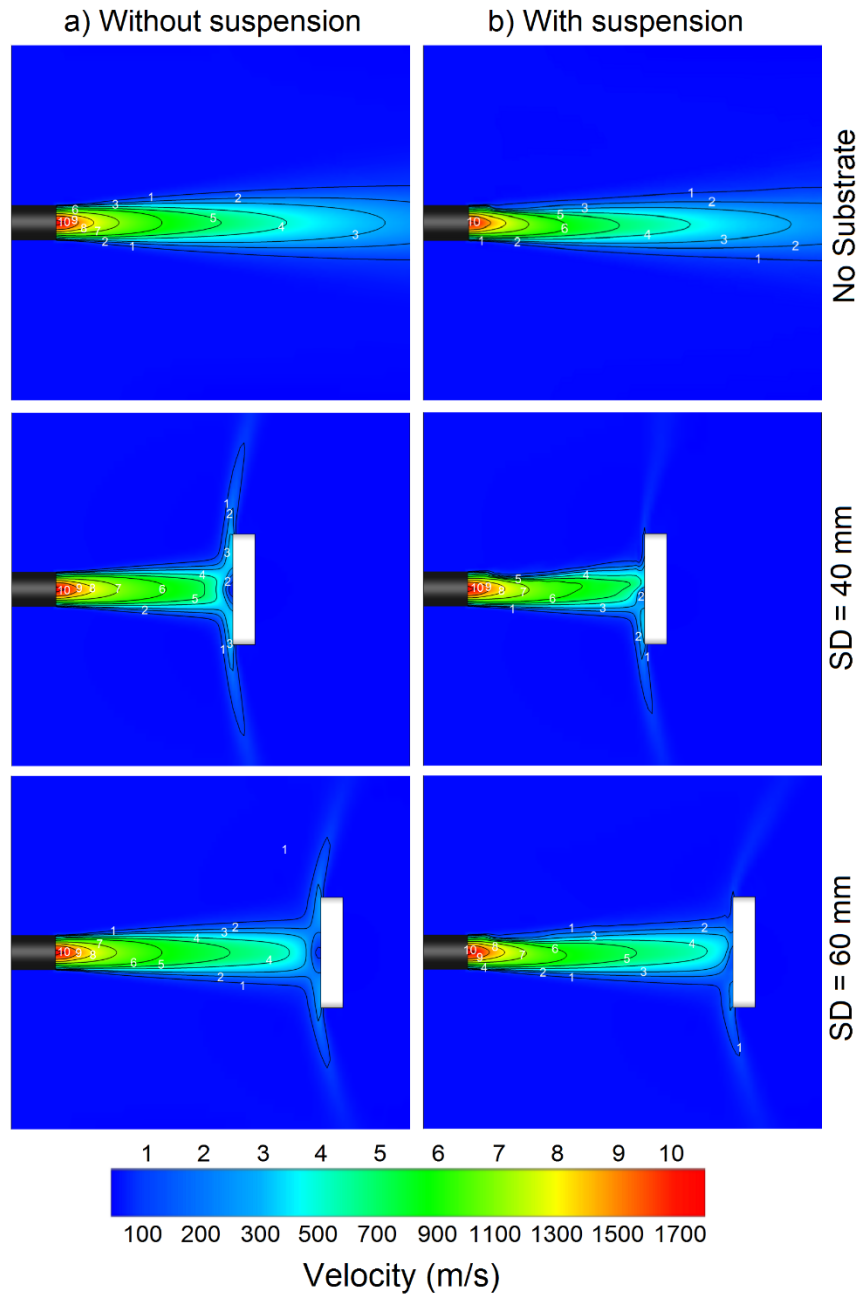


Figure 2.6 The comparison between gas velocities at various standoff distances for a) without suspension injection, b) with suspension injection

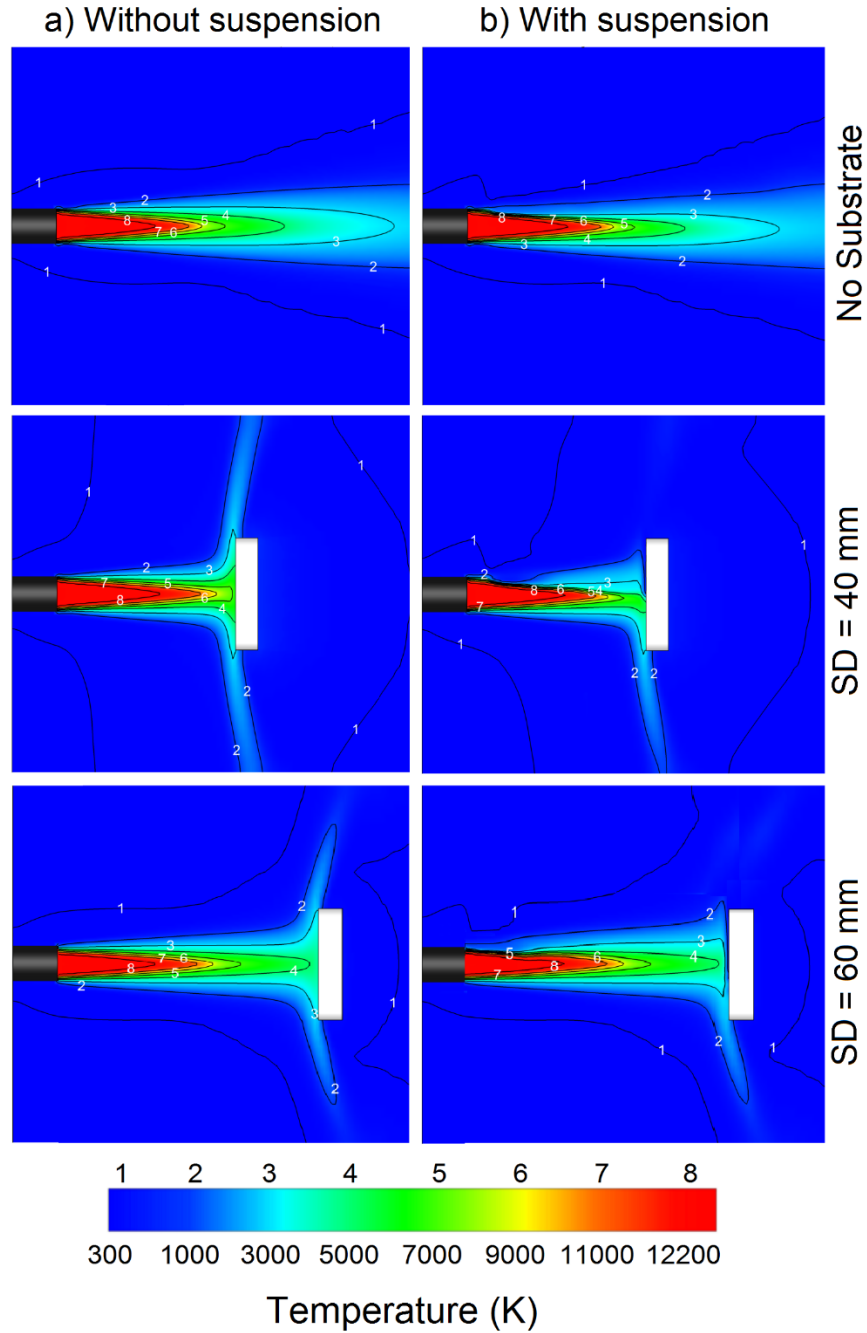


Figure 2.7 The comparison between gas temperatures at various standoff distances for a) without suspension injection, b) with suspension injection

The influence of the substrate presence on the gas temperature when the standoff distance increases from 40 to 60 mm, is shown in Figure (2.7-a) and Figure (2.7-b) for the cases without

and with suspension injection, respectively. Interestingly, for a short standoff distance of 40 mm, the plasma high temperature core is extended compared to the free jet case. The main reason is the less mixing rate between air and argon in the case of standoff distance of 40 mm. However, as the standoff distance increases from 40 to 60 mm, the mixing rate increases and the plasma high temperature zone is diminished. Nevertheless, compared to free jet case, the plasma high temperature core is slightly wider for the case of standoff distance of 60 mm. The effect of standoff distance on the plasma high temperature core is quantitatively explained in the next paragraphs. Furthermore, as shown in Figure (2.7-b), due to the suspension penetration and evaporation, the plasma temperature decreases. As presented in Figure (2.8), the penetration depth of suspension into plasma plume slightly increases as the standoff distance decreases. As a result, the standoff distance does not have significant influence on the penetration depth of suspension. This seems to be reasonable because of the low surface tension and the high evaporation rate of ethanol.

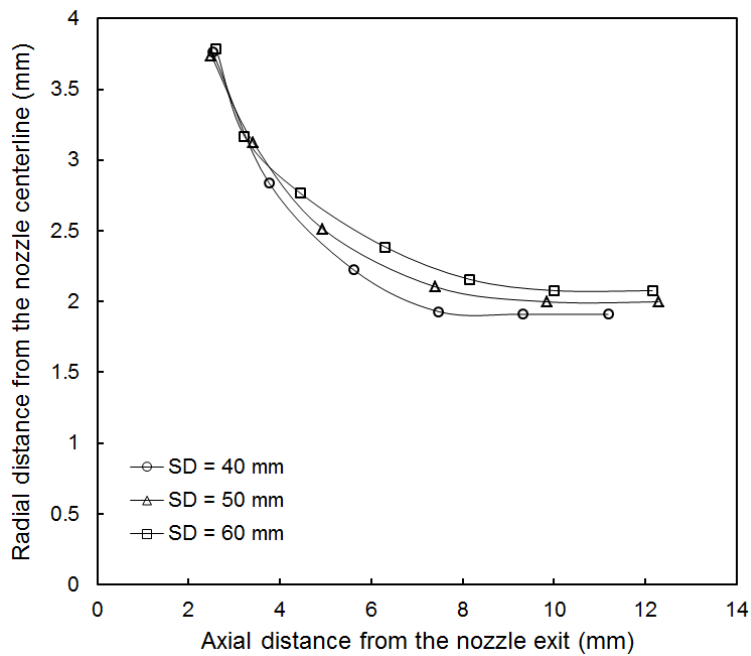


Figure 2.8 The penetration depth of suspension in the plasma plume as a function of standoff distance

Figure (2.9) shows the variations of gas temperature and velocity magnitude in the plane located at $d_{fs}=1\text{mm}$ (within the wall jet and outside the boundary layer) as a function of standoff distance (SD). As shown in Figure (2.9-a), at $SD=40\text{mm}$, the gas temperature decreases from 7000K at the center to 3000K near the edge of the substrate. However, at $SD=60\text{mm}$ (see Figure (2.9-b)), the gas temperature reduces from 4500K to 2000K. Therefore, as the standoff distance increases, the heat flux to the wall decreases significantly. Figure (2.9) also illustrates that the velocity magnitude decreases as the standoff distance increases. Therefore, fine particles are expected to deviate more at shorter standoff distance since the gas radial velocity is higher. The particle behavior as a function of standoff distance will be discussed in the next paragraphs in more details.

As mentioned above, Lapierre *et al.* [77] experimentally presented that when a cooled substrate is placed at standoff distances of 80-120 mm, the centerline temperature of plasma jet is increased by about 22% at the substrate location. Their experimental data is used to validate our simulation. The comparison between current numerical study where the standoff distance is 60 mm and the experimental data [77] is shown in Figure (2.10). The horizontal axis is the distance, d_{fs} , from the substrate (see Figure (2.2)) where the substrate is located at point 0 ($d_{fs}=0$). The vertical axis shows the temperature change. The gas temperature when the substrate exists in the flow (T_{sub}) is subtracted from the gas temperature when there is no substrate in the domain (T). This value then is divided by T to represent the normalized temperature difference. It is shown that there is a good agreement between the numerical and experimental results. The simulation predicts that the centerline temperature is increased by about 22% at the substrate location which is in agreement with the experimental result presented in [77]. As the distance from the substrate increases, the temperature change of the plasma reduces.

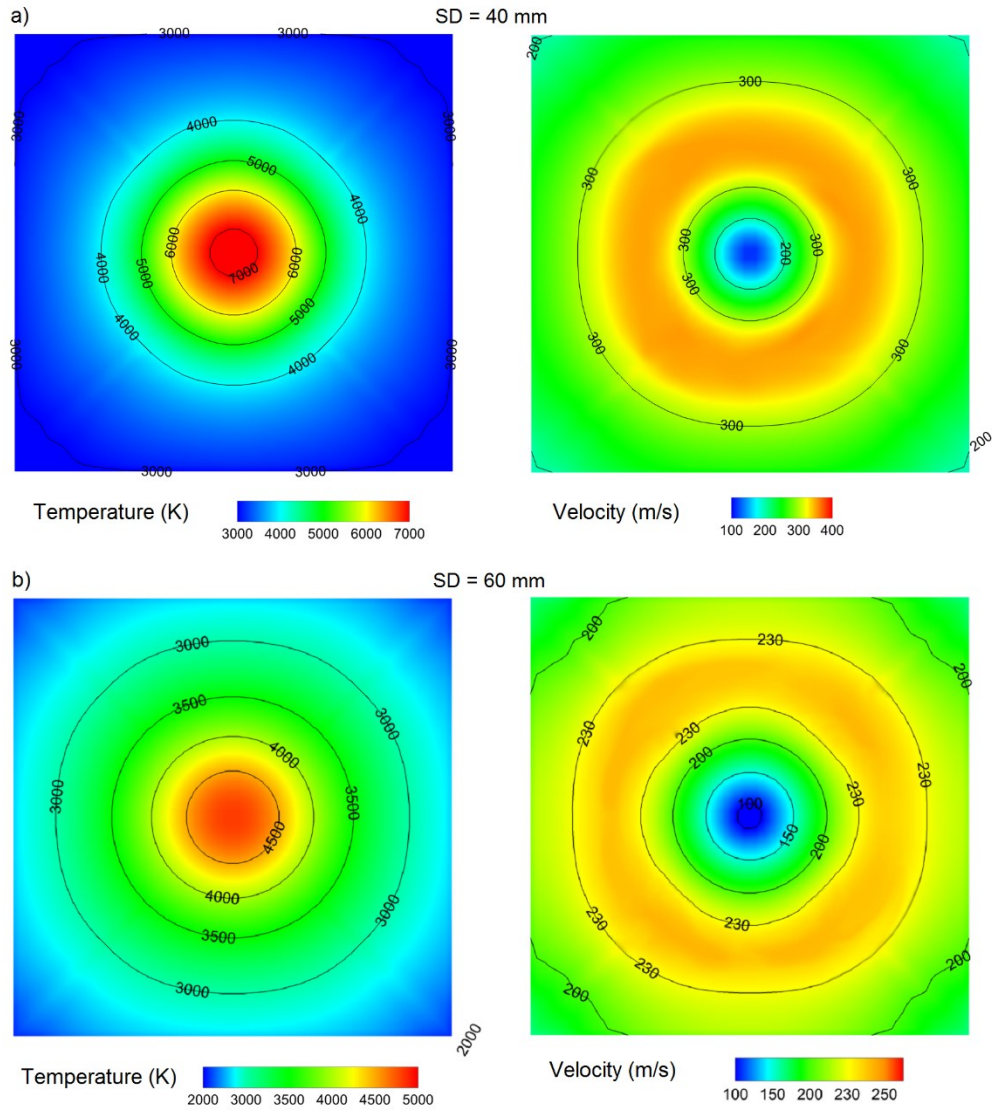


Figure 2.9 The variation of gas temperature and velocity near the substrate (at $d_{fs}=1$ mm) (a) $SD=40$ mm and (b) $SD=60$ mm as a function of standoff distance (size of each figure is the same as substrate size)

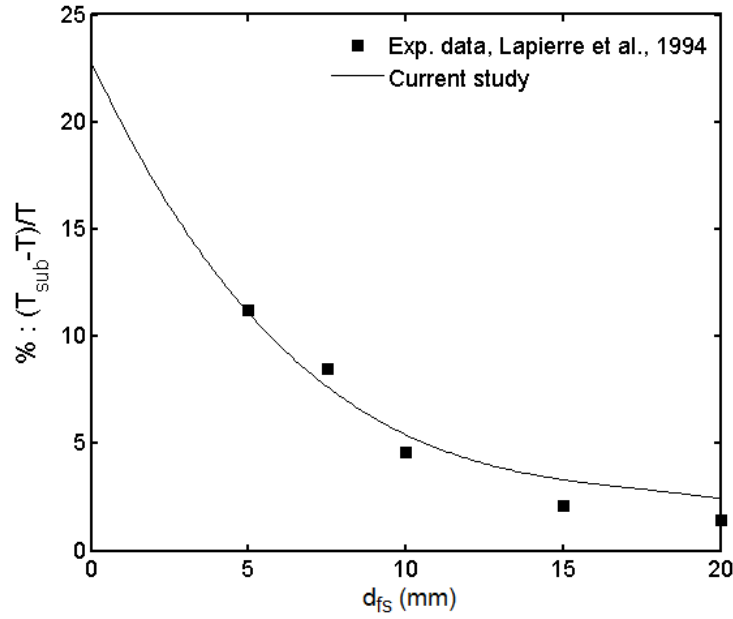


Figure 2.10 Change in the plasma temperature as a function of distance from the substrate. T_{sub} stands for the plasma temperature when the substrate exists in the flow and T stands for the plasma temperature when there is no substrate in the domain

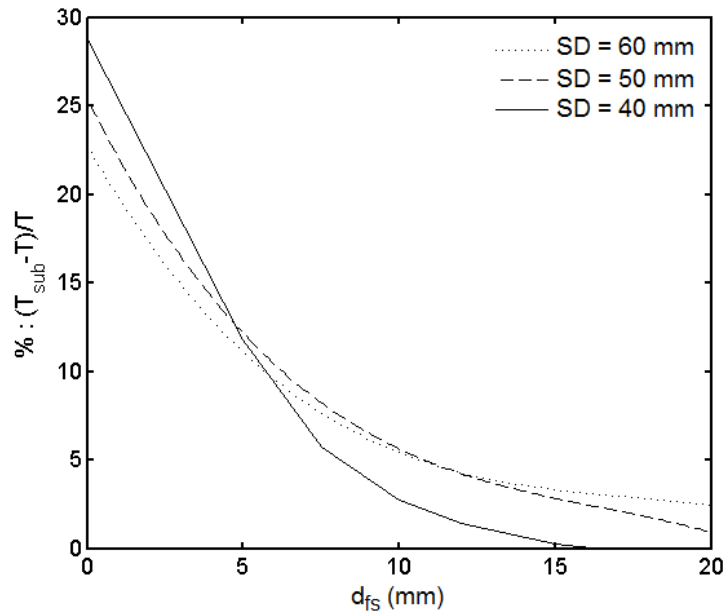


Figure 2.11 Change in the plasma temperature as a function of distance from the substrate and substrate standoff distance

The effect of substrate location on the centerline gas temperature is shown in Figure (2.11). By decreasing the standoff distance from 60 to 40 mm, the normalized temperature change defined above, increases from 22% to 28% at the substrate location. In addition, the slope of these curves can show the heat flux to the substrate. As the standoff distance decreases, the slope of the curve increases therefore heat flux to the substrate grows.

A side view of particle trajectory, velocity and temperature for free jet case as well as standoff distances of 40 and 60 mm are demonstrated in Figures (2.12) and (2.13). As it is clear from the figures, many particles especially very fine particles strongly track the gas phase streamlines and get diverted by the flow in the stagnation region. It should be noted that the particles that move close to the centerline can reach very high temperature and velocity and are less affected by the flow in the stagnation region and the wall jet. Many particles reach the molten state with the axial velocity more than 400 m/s. It is also theoretically proven that the most probable particles to be deposited are those that travel near the dividing streamline (i.e. jet centerline) or lying on it, which terminates at the stagnation point on the substrate [83]. In other words, although many particles get diverted by the stagnation region and follow the wall jet, the particles that move close to the centerline enter the boundary layer and almost all of them are coated since the particle velocity is relatively high and the thickness of boundary layer is very small. The boundary layer thickness is at most 3% of the jet diameter (the jet or torch exit diameter is 7.88 mm). This value is in agreement with the experimental and numerical results obtained from generic impingement jet flow field [79-81].

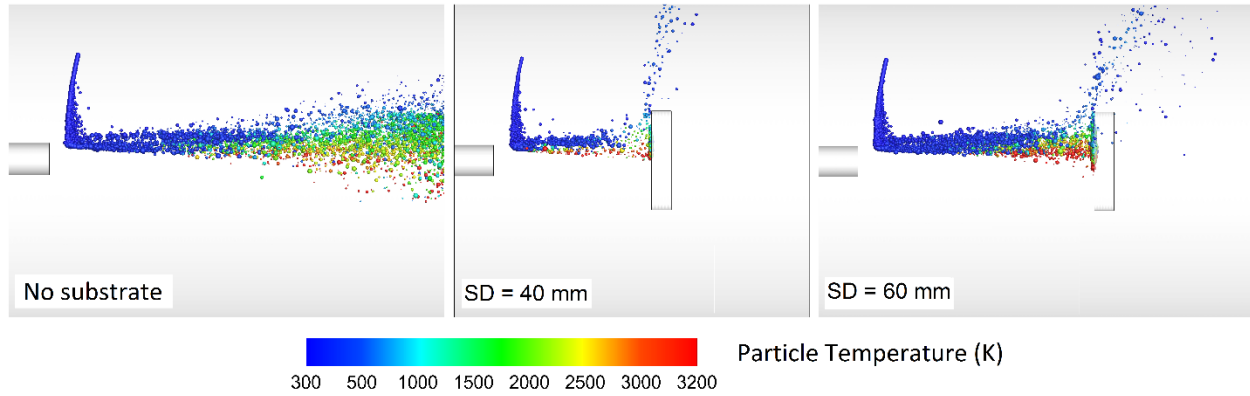


Figure 2.12 The effect of standoff distance on the particle temperature and trajectory

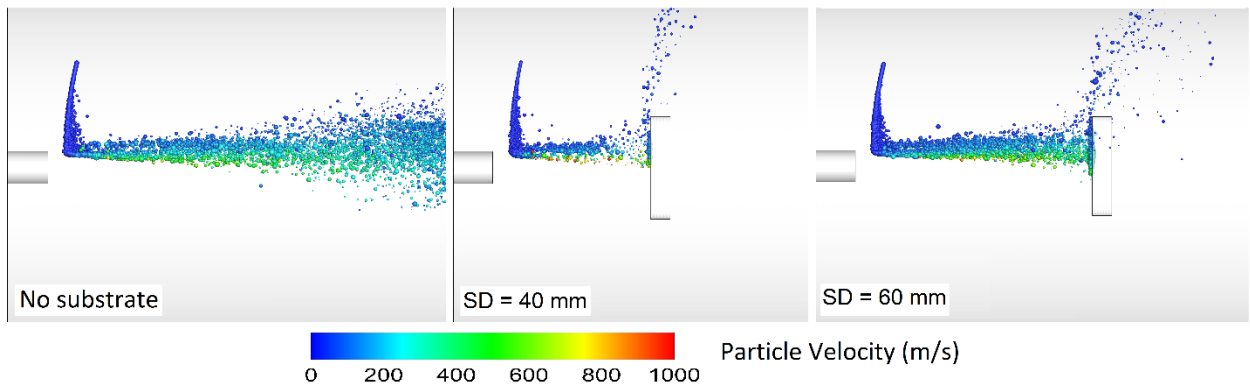


Figure 2.13 The effect of standoff distance on the particle velocity and trajectory

Figures (2.14-2.16) are presented to study the effect of stagnation region on the particle behavior in more details. The standoff distances in these figures are 40 and 60 mm. The particles that are inside a 25X25 mm² window (the size of the substrate) at the nozzle centerline are considered only. The particle size distribution as a function of cumulative percentage of particles at 5 mm ($d_{fs}=5$ mm) and 1 mm ($d_{fs}=1$ mm) elevation from the substrate is shown in Figure (2.14). It is shown that the influence of stagnation region on the smaller particles is more severe. From $d_{fs}=5$ mm to $d_{fs}=1$ mm, many small particles are decelerated and get diverted by the stagnation region in both mentioned standoff distances. As a result, the percentage of small particles decreases

and the percentage of relatively large particles increases in the vicinity of the substrate. It is also shown that the effect of stagnation region at standoff distance of 40 mm is stronger than its influence at standoff distance of 60 mm because more small particles are deviated for the former case. It should be noted that as the standoff distance decreases the static pressure on the substrate increases and therefore the percentage of deviated small particles increases.

The particle temperature as a function of cumulative percentage of particles at 5 mm ($d_{fs}=5$ mm) and 1 mm ($d_{fs}=1$ mm) elevation from the substrate is revealed in Figure (2.15). To describe this figure, two important phenomena must be considered. First, as mentioned above, small particles get diverted by the stagnation region. Second, the particle velocity and temperature strongly depend on the particle size. The momentum exchange and heat transfer have more significant effects on the velocity and temperature of smaller particles. Therefore, from $d_{fs}=5$ mm to $d_{fs}=1$ mm where many small particles get diverted by the stagnation flow, the percentage of very high and low temperature particles reduces and the number of particles with moderate temperature increases in both standoff distances. The reason is that the high and low temperatures belong to the very fine particles which are mostly deviated and the moderate temperatures belong to the relatively large particles. Changing the standoff distance from 40 to 60 mm mainly causes an increase and decrease in the percentage of very high and very low temperature particles, respectively. However, at $d_{fs}=1$ mm, it is clear that the percentage of the particles with temperatures between 1728 K and 2700 K (which are at the molten state) at standoff distance of 40 mm is more than that at standoff distance of 60 mm. At a standoff distance of 60 mm, more particles reach the boiling point.

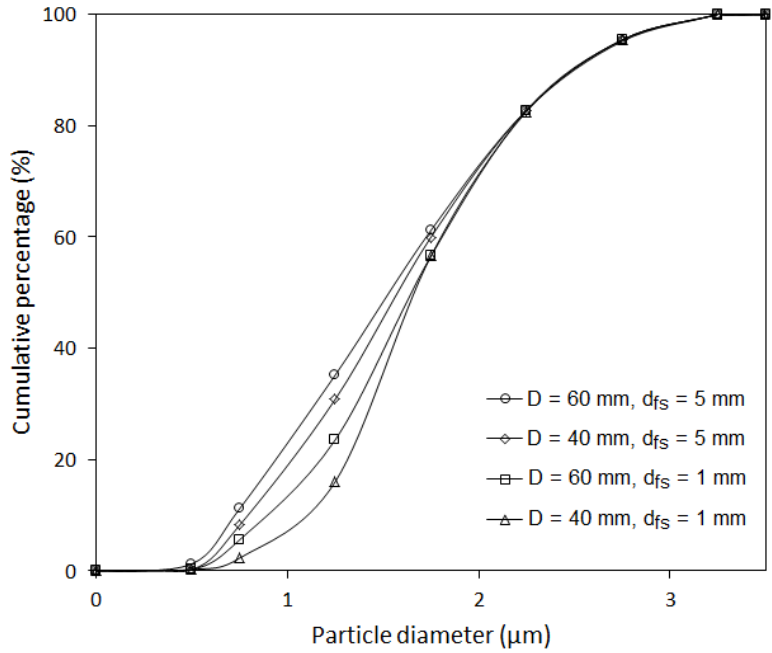


Figure 2.14 Particle size distributions as a function of cumulative percentage of particles at different standoff distances

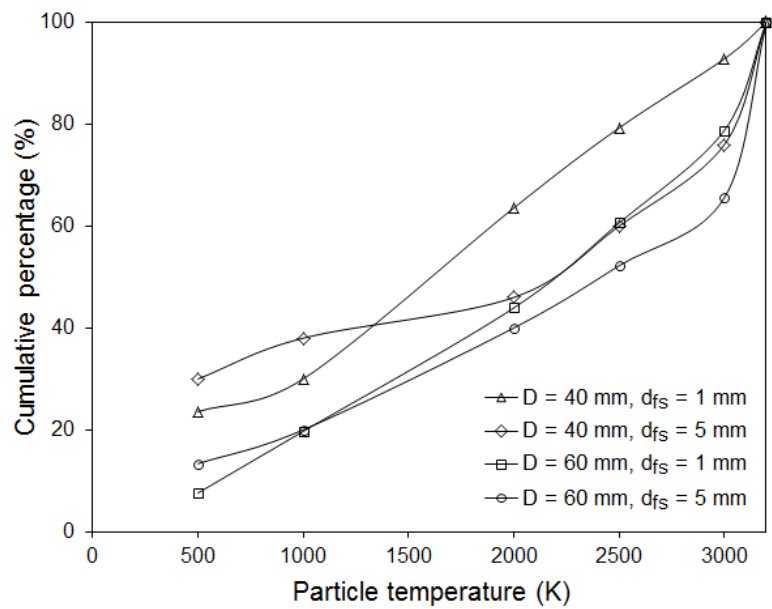


Figure 2.15 Particle temperature profiles as a function of cumulative percentage of particles at different standoff distances

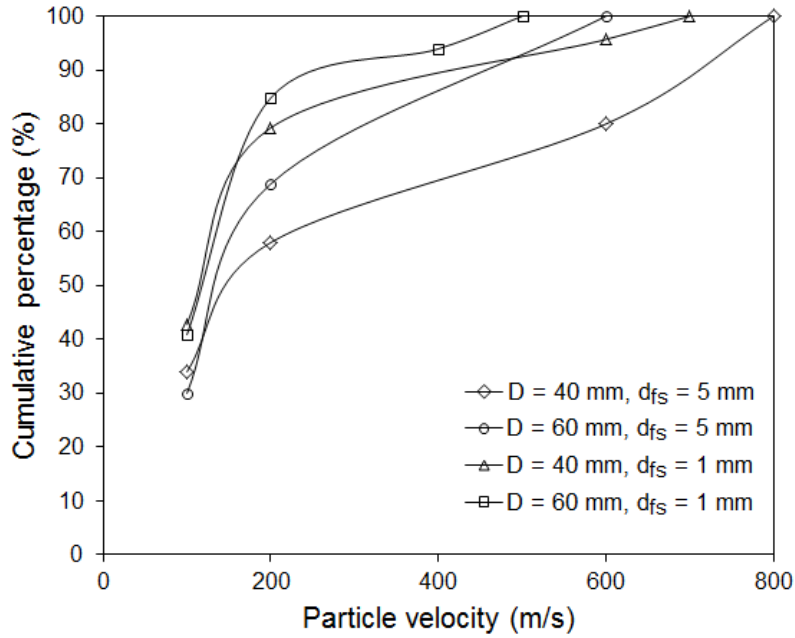


Figure 2.16 Particle velocity profiles as a function of cumulative percentage of particles at different standoff distances

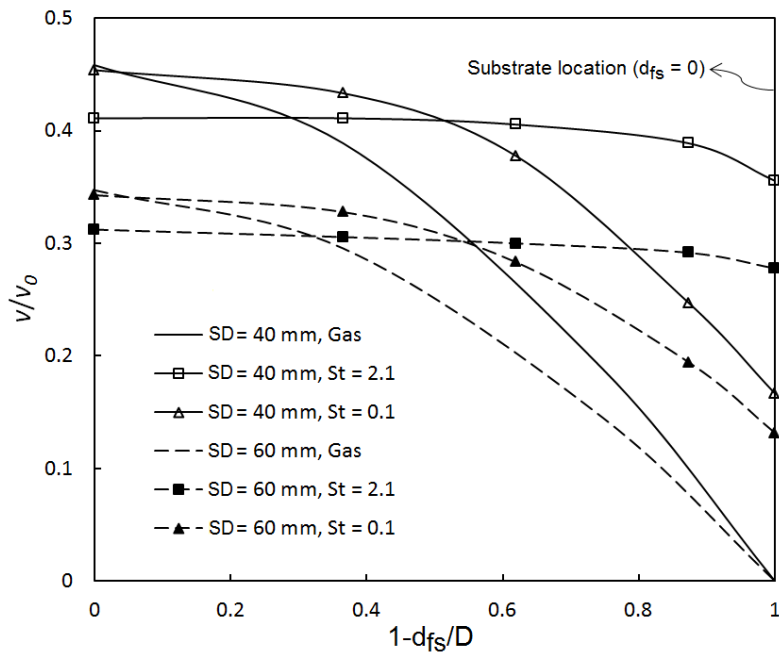


Figure 2.17 Effect of particle Stokes number on particle conditions upon impact (using normalized velocity and diameter, $v_0=1800$ m/s and $D=7.88$ mm)

The particle axial velocity as a function of cumulative percentage of particles is illustrated in Figure (2.16). From $d_{fs}=5$ mm to $d_{fs}=1$ mm, the percentage of particles with high and low axial velocity reduces and increases, respectively, due to the stagnation region effects. It should be noted that particle radial velocity has an opposite trend. As can be seen, at a standoff distance of 40 mm, many particles reach the velocity higher than 400 m/s. Since the standoff distance increases, the number of particles with high and low velocity decreases and increases respectively.

The particles that move near the centerline are mostly deposited on the substrate due to their rather high velocity and temperature upon impact. Stokes number is usually used to study the particles behavior near the substrate and their effects on the deposition pattern. Based on the mentioned suspension and plasma conditions, the Stokes number of the particles that move near the centerline (within a radius of 8mm) and are close to the substrate ($d_{fs}<8$ mm) changes from 0.1 to 2.1. These values are in agreement with the results obtained from generic impingement jet problems [99, 100]. The motion of these particles as a function of standoff distance and Stokes number as well as the gas centerline velocity are depicted in Figure (2.17) (using normalized velocity and diameter, $v_0=1800$ m/s and $D=7.88$ mm). It should be noted that both the gas velocity and viscosity decrease as the standoff distance increases. Therefore, for both standoff distances of 40 and 60 mm, the Stokes number remains in the mentioned range. As can be deduced from Figure (2.17), the particles with high Stokes number ($St=2.1$) decelerate very little as they approach the substrate. Therefore, their impact velocities may reach 650 and 500 m/s for the standoff distances of 40 and 60 mm, respectively. The incident angle (the angle between particle trajectory and substrate normal vector) of particles with high Stokes number ($St=2.1$) reaches 15° and 25° for the standoff distances of 60 and 40 mm, respectively. On the other hand, particles with low Stokes number ($St=0.1$) decelerate dramatically and their impact velocities reach 300 and 230 m/s for the

standoff distances of 40 and 60 mm, respectively. The incident angle of these particles ($St=0.1$) is 40° and 50° for the standoff distances of 60 and 40 mm, respectively. It should be noted that the Stokes number of particles that are far from the centerline is lower than 0.1 which makes most of them to get diverted by the stagnation flow and follow the wall jet.

The landing location of the particles on the substrates with standoff distances of 40 and 60 mm is shown in Figure (2.18). In addition, temperature, velocity and size of the landed particles are clearly shown in this figure. The $25 \times 25 \text{ mm}^2$ area in the figure illustrates the substrate. It is clear that almost all of the particles land on the upper half of the substrate for both standoff distances. By inspecting the particle temperatures upon impact, it is clear that most of the landed particles are fully molten since their temperature is more than 1728 K which is the melting temperature of nickel. Furthermore, the velocity of a considerable number of particles, especially when the substrate is placed at standoff distance of 40 mm, is more than 400 m/s. It is clear from Figure (2.18) that the particle deposition pattern includes a circular area near the center which consists of particles with high temperature and impact velocities, and a few rings, around the circular area, which contain particles with low temperature and impact velocities. In other words, as the radial distance from the center increases, the particle temperature and impact velocity decreases. This pattern is clearly related to the particle Stokes number. As mentioned above, particles with low Stokes number decelerate sharply near the substrate and follow the gas streamlines. Therefore, these particles struck the substrate at large radial distance from the center, large angle, and low velocity and temperature. It is also revealed from Figure (2.18) that one of the most significant parameter to achieve a dense coating is the standoff distance. It is demonstrated that when the standoff distance is 40 mm, a denser coating can be expected. In other words, if the position of substrate changes from 40 to 60 mm, the coating porosity would increase.

It was experimentally shown that the porosity increases as the standoff distance grows from 40 to 60 mm [87].

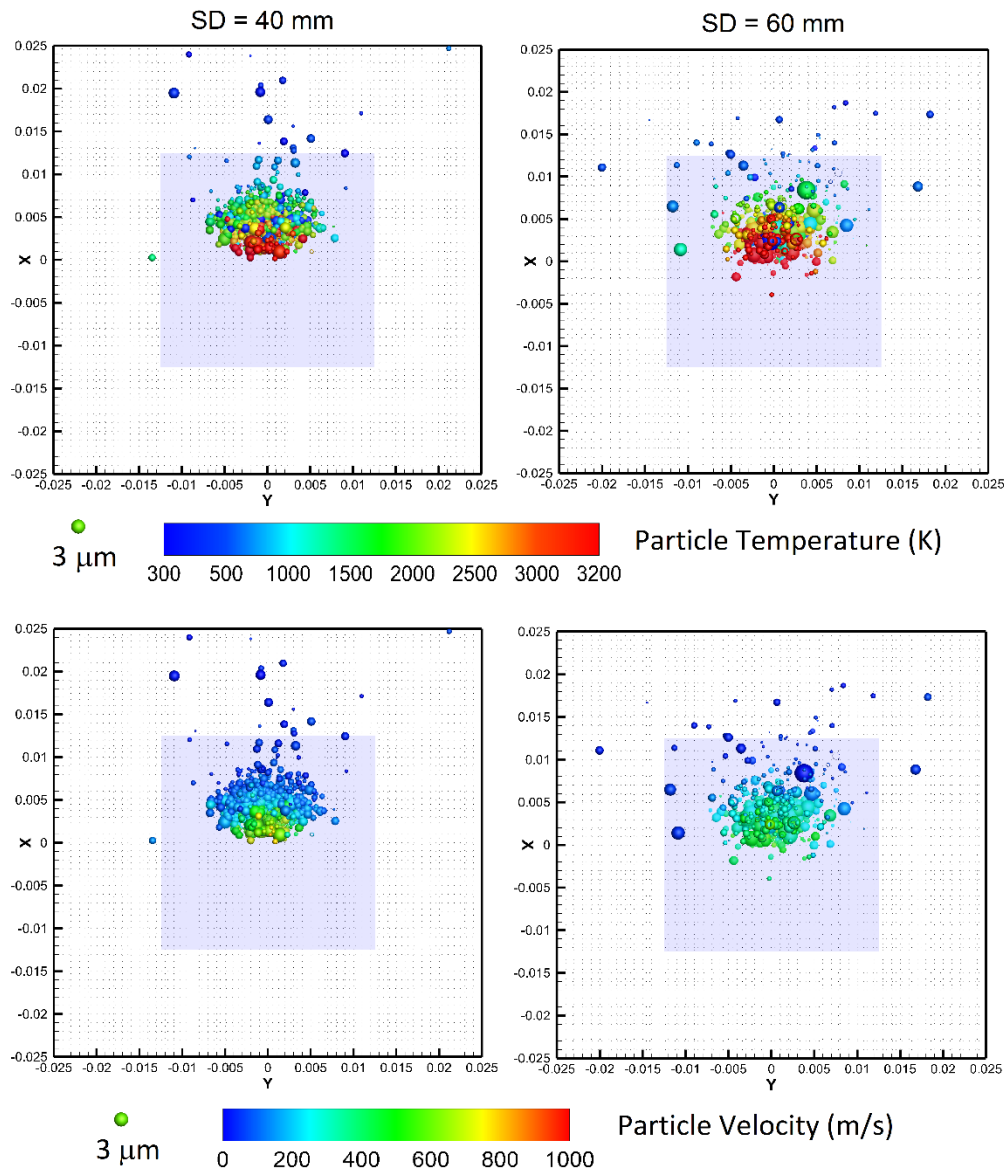


Figure 2.18 Landing location, particle temperature, size and velocity on the substrate as a function of standoff distances

2.4 Summary and Conclusions

Using discrete phase, Kelvin-Helmholtz Rayleigh-Taylor (KHRT) and Reynolds stress models, the suspension temperature, velocity, and trajectory are studied in this paper. The effect of the standoff distance on plasma jet is also investigated. For the cases without suspension injection, an axisymmetric stagnation flow is formed on the substrate. The gas radial and axial velocities near the substrate decrease by increasing the standoff distance. As the standoff distance decreases from 60 to 40 mm, the normalized temperature change increases from 22% to 28% at the substrate location. The plasma velocity and temperature decrease due to the thermal and momentum exchange of the suspension cross-flow where the suspension penetrates. In addition, the penetration depth of suspension is not influenced by the standoff distance significantly. The effect of standoff distance on the particles' temperature, velocity and trajectory is discussed. It is shown that many small particles are decelerated and get diverted by the stagnation region. However, particles that move near the centerline reach high velocity and temperature and are less influenced by the flow in the stagnation region. Stokes number is used to study the particle behavior near the substrate systematically. It is shown that although particles with high Stokes number ($St=2.1$) decelerate very little, particles with low Stokes number ($St=0.1$) decelerate dramatically and follow the gas streamlines. Therefore, particles with low Stokes number struck the substrate at large radial distance from the center, and low velocity. Furthermore, by inspecting the particle landing conditions, one can correlate the final coating properties such as coating porosity, adhesion, and deposition efficiency for various substrate standoff distances.

Chapter 3

Numerical Modeling of Suspension HVOF Spray

“Reprinted from the paper published in Journal of Thermal Spray Technology, 2016, volume 25, pp. 451-464, [101], with permission”

Abstract

A three dimensional two-way coupled Eulerian-Lagrangian scheme is used to simulate suspension high velocity oxy-fuel (HVOF) spraying process. The mass, momentum, energy, and species equations are solved together with the realizable $k-\epsilon$ turbulence model to simulate the gas phase. Suspension is assumed to be a mixture of solid particles (mullite powder ($3\text{Al}_2\text{O}_3 \cdot 2\text{SiO}_2$)), ethanol and ethylene glycol. The process involves premixed combustion of oxygen-propylene, and non-premixed combustion of oxygen-ethanol and oxygen-ethylene glycol. One step global reaction is used for each mentioned reaction together with eddy dissipation model to compute the reaction rate. To simulate the droplets breakup, Taylor Analogy Breakup (TAB) model is applied. After the completion of droplet breakup, and solvent evaporation/combustion, the solid suspended particles are tracked through the domain to determine the characteristics of the coating particles. Numerical simulations are validated against the experimental results in literature for the same operating conditions. Seven or possibly eight shock diamonds are captured outside the nozzle.

In addition, a good agreement between the predicted particle temperature, velocity and diameter, and the experiment is obtained. It is shown that as the standoff distance increases, the particle temperature, and velocity reduce. Furthermore, a correlation is proposed to determine the spray cross section diameter and estimate the particle trajectories as a function of standoff distance.

3.1 Introduction

Suspension thermal spraying is an emerging process for generating coatings with superior properties. Nano up to few micron-sized solid particles are suspended in a base fluid, such as water or ethanol, and injected into the high-temperature high-velocity jets [7, 8, 13, 102, 103]. The coatings generated by suspension thermal spray technique have revealed enhanced characteristics, such as superior catalytic behavior, remarkable wear resistance, enhanced thermal insulation, thermal shock resistance, and superhydrophobicity [7, 8, 13, 102-110]. Suspension is mainly used in conjugation with the atmospheric plasma spraying (APS) and high velocity oxygen-fuel (HVOF) spraying techniques [1, 9, 10, 12, 18, 73, 111, 112]. Simulation of suspension HVOF technique is the focus of the current paper.

In this technique, oxygen and fuel are injected into the combustion chamber and burn. The combustion products then go through a convergent-divergent nozzle; consequently a supersonic jet emerges into the surrounding air. An over-expanded/under-expanded flow exiting the nozzle results in forming a series of compression and expansion waves (known as shock diamond) [1, 2, 113-115]. Suspension is usually injected into the jet in axial direction [1, 10, 18, 112]. After injecting the suspension, the jet atomizes the suspension (primary and secondary breakups) and then the liquid evaporation becomes dominant [8]. If the suspension base fluid is a liquid

hydrocarbon such as ethanol, the non-premixed combustion occurs where vapors react with oxygen [1, 116]. Due to the base fluid vaporization, the solid particles or their agglomerations remain in the field where they are heated up by the flame/jet and accelerate toward the substrate [1, 8].

It is worth mentioning that experimental measurements in HVOF process are limited to the nozzle outside. Consequently, simulation techniques seem to be the tool for understanding the physics inside the nozzle. However, presence of compressible turbulent multiphase flow with chemical reactions enhances the complexity of the suspension HVOF simulation. These simulations are important for both scientific and industrial applications to optimize the torch, and to produce coatings with enhanced properties. In the past few years, a number of studies were dedicated to simulate the interactions between suspension and flame. Eulerian-Lagrangian approach have been mainly used in literature to model the suspension HVOF process since concentration of the droplet/particle phase is usually not high in the system. In this method, the gas is modeled as a continuum phase while a discrete phase model (DPM) is used to simulate the droplets/particles heat transfer and motion [1, 21].

In order to simplify the complex phenomena in suspension HVOF process, few numerical studies focused only on the liquid part of the suspension [30-32]. Taleby and Hossainpour [30] studied the effect of various parameters such as ethanol droplets size and injection velocity on the gas flow field. They found that the evaporation region shifted downstream and the evaporation intensity decreased as the droplet injection velocity or the droplet diameter increased. Noting that the droplet breakup was not considered in their study. Gozali *et al.* [31] also investigated the effects of ethanol droplet size, mass flow rate, and injection velocity on gas flow field and droplets vaporization parametrically. Their investigation showed that the suspension HVOF process is

mainly controlled by the liquid feedstock mass flow rate. Due to the large relative velocity between gas and liquid phases, the liquid droplets undergo significant fragmentation in the middle of the combustion chamber. They concluded that the larger droplets undergo more intensive breakup [31]. Gozali *et al.* [32] developed their model to study the liquid feedstock or suspension as a various mixture of ethanol and water. The mixture was modeled as a multicomponent droplet and the suspension evaporation was simulated by a convection/diffusion model. It was shown that for the cases with high ethanol content in the solvent, the maximum evaporation occurs inside the combustion chamber. On the other hand, the evaporation was significantly delayed and took place in all internal regions of the gun for droplets with high percentage of water (more than 50%). Dongmo *et al.* [33, 34] considered suspension as two separate parcels; droplet and particle parcels. Droplets and particles were separately injected into the combustion chamber through the nozzle central port. Both particles and droplets were tracked separately through the domain.

The motivation for the current study is to model multi-component suspension (slurry) droplets including base fluid and solid particles. Consequently, suspension atomization, evaporation, particle trajectory, velocity and temperature are numerically modelled and validated against experimental results [117].

3.2 Mathematical Modeling

In order to simulate the suspension HVOF experiment described in [117], the geometry of DJ2700 torch (Oerlikon Metco, Westbury, NY) is used in this work. The 3D computational domain, boundary conditions and the gun dimensions are shown in Figure (3.1) and Table 3.1. A hexahedral grid which is composed of 1,986,715 elements is used. In this study, the Eulerian-Lagrangian approach with two-way coupling assumption is applied using ANSYS-Fluent® release

14 [29]. First, the pressure, velocity and temperature of the gas phase without suspension injection are simulated. The propylene-oxygen mixture is injected through an annular inlet (see [113]) into the combustion chamber. The mass flow rate of propylene and oxygen are 2.66 and 6.64 g/s, respectively. Nitrogen is also injected through the central inlet with a mass flow rate of 0.313 g/s, serving as coolant and atomizing gas. In addition, air serving as coolant is injected through an annular inlet into the combustion chamber with a mass flow rate of 4.35 g/s. The above mentioned flow rates are the same as what is presented in [117]; Gases initial temperature is 300 K. The nozzle and the combustion chamber walls are modeled with a no-slip, fixed temperature condition (350 K). A turbulence intensity of 10% is used at the inlet boundaries.

To model the gas phase, the compressible form of the mass, momentum, energy and species equations are solved together with an ideal gas equation of state. To simulate the turbulent flow, the realizable k - ε model together with scalable wall functions is used (see [29-32, 118, 119]). The mass and momentum conservation equations (based on the time-averaged (Reynolds-averaged) and density-averaged (Favre-averaged, $\overline{\rho\phi} = \bar{\rho}\tilde{\phi}$)) are as follows

Continuity

$$\nabla \cdot \bar{\rho}\tilde{\mathbf{u}} = 0 \quad \text{Equation 3.1}$$

Momentum

$$\bar{\rho}\tilde{\mathbf{u}} \cdot \nabla \tilde{\mathbf{u}} = -\nabla \bar{p} + \nabla \cdot \bar{\boldsymbol{\tau}} - \nabla \cdot (\bar{\rho}\widetilde{\mathbf{u}'\mathbf{u}'}) \quad \text{Equation 3.2}$$

where \mathbf{u} , \mathbf{u}' , ρ , p , and τ are the gas velocity vector, velocity fluctuation, density, pressure, and viscous shear stress, respectively. When the fluid is Newtonian, the shear stress tensor is given by (the overbar on the mean velocity is dropped)

$$\boldsymbol{\tau} = \mu[(\nabla\mathbf{u}) + (\nabla\mathbf{u})^T] - \left(\frac{2}{3}\mu - \xi\right)(\nabla \cdot \mathbf{u})\mathbf{I} \quad \text{Equation 3.3}$$

where μ , ξ , \mathbf{I} are the dynamic viscosity, the bulk viscosity and the identity matrix, respectively.

Table 3.1 Operating condition

Fuel flow rate and inlet temperature	2.66 g/s	300 K
Oxygen flow rate and inlet temperature	6.64 g/s	300 K
Air flow rate and inlet temperature	4.35 g/s	300 K
Nitrogen flow rate and inlet temperature	0.313 g/s	300 K
Wall boundary conditions	No-slip	350 K
Droplet initial diameter and temperature	120 μm	300 K
Droplet initial velocity and flow rate	6.2 m/s	3 kg/h

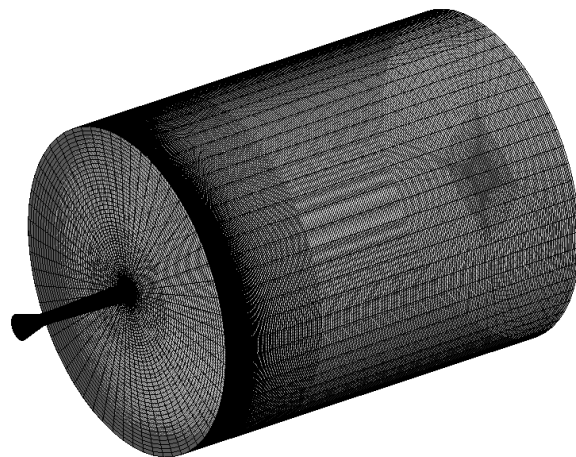
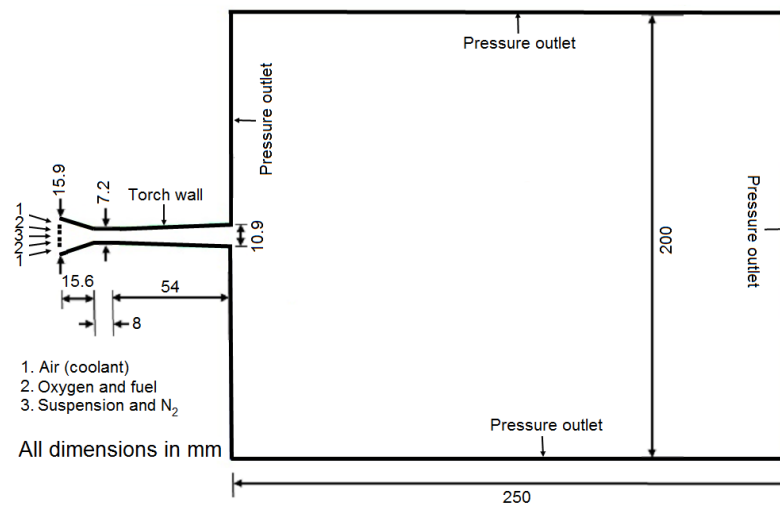


Figure 3.1 Geometry, boundary conditions, and computational mesh

The term $\overline{\rho \mathbf{u}'\mathbf{u}'}$ in the momentum equation is the Reynolds stress [29]. The Boussinesq equation is used to relate this term to the mean velocities as below

$$-\overline{\rho u'_i u'_j} = 2\mu_t S_{ij} - \frac{2}{3}\delta_{ij} \frac{\partial u_k}{\partial x_k} - \frac{2}{3}\rho k \delta_{ij} \quad \text{Equation 3.4}$$

where μ_t is the eddy viscosity and $S_{ij} = \frac{1}{2}\left(\frac{\partial u_i}{\partial x_j} + \frac{\partial u_j}{\partial x_i}\right)$ is the mean strain rate tensor. In the realizable k - ε model, k is the turbulent kinetic energy, $k = \frac{\overline{u'_i u'_i}}{2}$, and ε is the viscous dissipation rate of turbulent kinetic energy, $\varepsilon = \left(\frac{\mu}{\rho}\right) \overline{u'_{i,j} u'_{i,j}}$. The transport equations in the realizable k - ε model are as follows [29]

$$\frac{\partial}{\partial t}(\rho k) + \frac{\partial}{\partial x_i}(\rho k u_i) = \frac{\partial}{\partial x_j} \left[\left(\mu + \frac{\mu_t}{\sigma_k} \right) \frac{\partial k}{\partial x_j} \right] + G_k - \rho \varepsilon - Y_M + S_k \quad \text{Equation 3.5}$$

$$\begin{aligned} \frac{\partial}{\partial t}(\rho \varepsilon) + \frac{\partial}{\partial x_i}(\rho \varepsilon u_i) &= \frac{\partial}{\partial x_j} \left[\left(\mu + \frac{\mu_t}{\sigma_\varepsilon} \right) \frac{\partial \varepsilon}{\partial x_j} \right] + \rho C_1 S \varepsilon - \rho C_2 \frac{\varepsilon^2}{k + \sqrt{\nu \varepsilon}} + \\ &C_{1\varepsilon} \frac{\varepsilon}{k} C_{3\varepsilon} G_b + S_\varepsilon \end{aligned} \quad \text{Equation 3.6}$$

where $\mu_t = C_\mu \rho \frac{k^2}{\varepsilon}$, $C_1 = \max \left[0.43, \frac{\eta}{\eta + 5} \right]$, $\eta = S \frac{k}{\varepsilon}$, $S = \sqrt{2S_{ij}S_{ij}}$ and S_k, S_ε are the source terms.

In the realizable k - ε model, C_μ is not constant and is computed from the below formulas

$$\begin{aligned} C_\mu &= \frac{1}{A_0 + A_s \frac{k U^*}{\varepsilon}}, U^* = \sqrt{S_{ij}S_{ij} + \widetilde{\Omega}_{ij}\widetilde{\Omega}_{ij}}, \widetilde{\Omega}_{ij} = \Omega_{ij} - 2\epsilon_{ijk}\omega_k, \Omega_{ij} = \overline{\Omega_{ij}} - \\ \epsilon_{ijk}\omega_k, A_0 &= 4.04, A_s = \sqrt{6} \cos \phi, \phi = \frac{1}{3} \cos^{-1}(\sqrt{6}W), W = \frac{S_{ij}S_{jk}S_{ki}}{\tilde{S}^3}, \tilde{S} = \\ &\sqrt{S_{ij}S_{ij}} \end{aligned} \quad \text{Equation 3.7}$$

where $\overline{\Omega_{ij}}$ is the tensor of rate-of-rotation observed in a moving reference frame with the angular speed ω_k .

The turbulent kinetic energy production is shown by G_k and given by

$$G_k = -\overline{\rho u_i' u_j'} \frac{\partial u_j}{\partial x_i} = 2\mu_t S_{ij} S_{ij} \quad \text{Equation 3.8}$$

In addition, Y_M is known as dilatation dissipation, which is an important parameter in high-Mach-number flows and shows the effect of compressibility on the turbulence

$$Y_M = 2\rho\varepsilon M_t^2 \quad \text{Equation 3.9}$$

where M_t is the turbulent Mach number, $M_t = \sqrt{\frac{k}{c^2}}$, and c is the sound speed [29].

The energy equation is as follows

$$\frac{\partial}{\partial t}(\rho E) + \frac{\partial}{\partial x_i}(u_i(\rho E + P)) = \frac{\partial}{\partial x_j} \left[\lambda_{eff} \frac{\partial T}{\partial x_j} + u_i(\tau_{ij})_{eff} \right] + S_h \quad \text{Equation 3.10}$$

where $E = e + u^2/2$ is the total energy, $(\tau_{ij})_{eff}$ is the deviatoric stress tensor, and λ_{eff} is the effective thermal conductivity. The term $\frac{\partial}{\partial x_j}(u_i(\tau_{ij})_{eff})$ in the energy equation represents the viscous heating influences. $(\tau_{ij})_{eff}$ is defined as

$$(\tau_{ij})_{eff} = \mu_{eff} \left(\frac{\partial u_j}{\partial x_i} + \frac{\partial u_i}{\partial x_j} \right) - \frac{2}{3} \mu_{eff} \left(\frac{\partial u_k}{\partial x_k} \right) \delta_{ij} \quad \text{Equation 3.11}$$

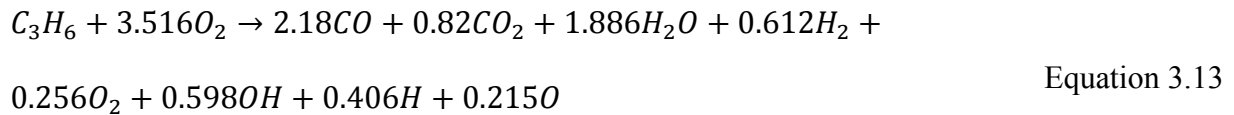
The effective thermal conductivity is also defined as

$$\lambda_{eff} = \lambda + \frac{c_p \mu_t}{Pr_t} \quad \text{Equation 3.12}$$

λ is the molecular thermal conductivity and Pr_t is the turbulent Prandtl number for energy. Similar to the turbulent heat transfer modeling, turbulent mass transfer simulation is based on the turbulent Schmidt number [29]. The segregated solution algorithm with a control volume based technique is used in this study. The discretization of the above equations is based on the second-order upwind scheme. In addition, the velocity and pressure are coupled using the semi-implicit method for pressure linked equations (SIMPLE) algorithm [29].

The combustion process is simulated by eddy dissipation model (also known as turbulent-chemistry interaction model, see [30-32, 113, 119]). This model is widely used to simulate both

premixed and non-premixed combustions in the suspension HVOF process (e.g. [30-32]). In this model the chemical kinetics rates are ignored and the overall reaction rate is controlled by turbulence. In other words, the most common assumption used for simulating turbulent combustion in HVOF is that the chemical reaction time scale is much smaller than the mixing time scale (i.e. Damkohler number is high). The consequence of this assumption is that the fluid in the turbulent flame is close to chemical equilibrium, and models and theories based on the equilibrium assumption are valid. The one-step global reaction (Equation (3.13)), which takes dissociations and intermediate reactions into account, is used for modeling propylene-oxygen combustion reactions



The equilibrium coefficients which depend on the ratio of the fuel to oxygen and the combustion chamber pressure, are calculated by Gordon and McBride code [120]. It should be noted that the mentioned combustion and turbulent models are widely tested against experimental results as shown in [1, 30-32, 113, 119].

The present work is an extension of the model developed by the authors in [19], to a three-component mixture model where the combustion of the base fluid is also considered. The suspension includes 5wt.% mullite powder ($3Al_2O_3 \cdot 2SiO_2$), 65wt.% ethanol and 30wt.% ethylene glycol (see Figure (3.2)). Ethanol and ethylene glycol are two liquid components and the third one carries mullite properties. Two one-step global reactions are used to simulate the ethanol-oxygen (Equation (3.14)) and ethylene glycol-oxygen (Equation (3.15)) combustion reactions. The combustion reactions are simulated by eddy dissipation model [30-32].

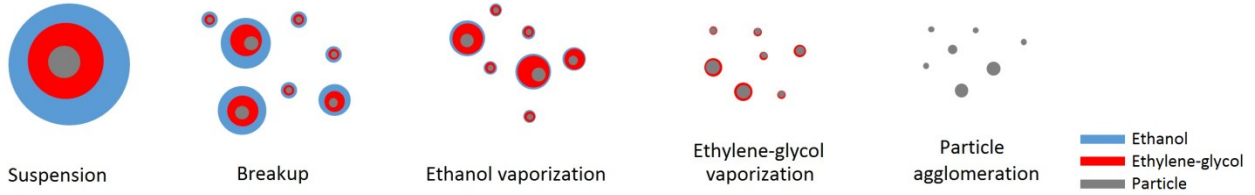
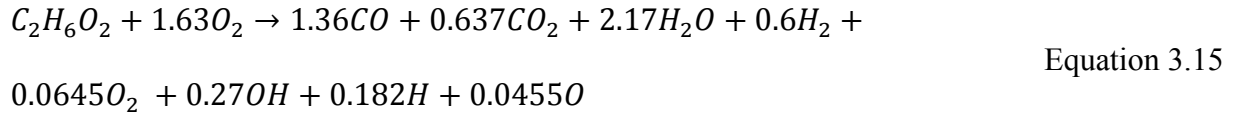
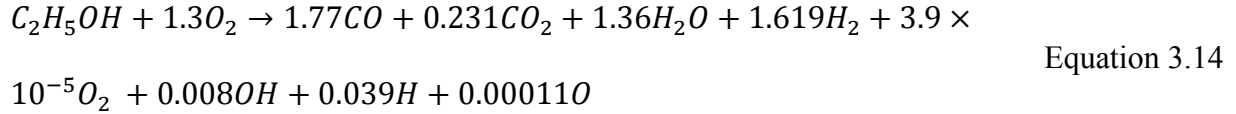


Figure 3.2 The schematic representation of suspension breakup, vaporization, and particle agglomeration in the current model

After solving the gas phase, the discrete phase model is used to simulate the injection of suspension droplets into the combustion chamber. In this study, a discrete injector is used which is composed of ten spherical droplets with a uniform size distribution (here 120 μm). The initial droplet diameter is calculated based on the empirical correlation for the mean droplet size [121]. The droplets are injected axially into the combustion chamber with a mass flow rate of 3 kg/h and with an initial temperature of 300 K.

The properties of the multicomponent droplet such as density and specific heat are based on mixing-laws explained in [32]. The volume-weighted-mixing-law is applied to define the density of multicomponent droplet. The multicomponent droplet mass, m_d , is the sum of the components masses

$$m_d = \sum_i m_i$$

Equation 3.16

and its density, ρ_d , is volume-averaged

$$\rho_d = \frac{1}{\sum_i \frac{m_i}{m_d \rho_i}} \quad \text{Equation 3.17}$$

The density of liquid ethanol, liquid ethylene glycol, and mullite are 790, 1111, and 2500 kg/m³, respectively [122, 123]. The specific heat of multicomponent droplet is based on the mass-weighted-mixing-law

$$C_{mix} = \sum_i Y_i C_i \quad \text{Equation 3.18}$$

The specific heat of liquid ethanol, and liquid ethylene glycol, are 2470, 2415 J/(kg.K), respectively. The data and correlations available in [123-125] are used to simulate the mullite specific heat as a function of temperature.

The suspension surface tension is assumed to be equal to the surface tension of liquid components, i.e. ethanol and ethylene glycol mixture, since the solid particle concentration is low [126-128]. The surface tension of liquid ethanol, liquid ethylene glycol, and mixture are 0.022, 0.048, and 0.025 N/m, respectively [126]. A piecewise-linear function is applied to estimate the droplet surface tension [19]. The suspension surface tension is used as far as the breakup process is dominant and as long as droplet temperature is less than or equal to the ethanol boiling point. For the next step, the surface tension of ethylene glycol is used as long as droplet temperature is less than or equal to the ethylene glycol boiling point. Then, solid particles are tracked through the domain. The same method is used to model the suspension viscosity. The viscosity of liquid ethanol, liquid ethylene glycol, and mixture are 0.0011, 0.0157, and 0.0022 kg/(ms), respectively [122].

The momentum conservation equation for suspension phase involves the drag force

$$F_D = \frac{1}{2} \rho C_D A |u - v| (u - v) \quad \text{Equation 3.19}$$

where ρ, C_D, A, v, u are the gas density, the drag coefficient, the particle projected area, the particle, and the gas velocity, respectively. The following empirical correlation that considers the

effect of Reynolds (Re), Mach (M), and Knudsen numbers ($Kn \sim M/Re$) is used to calculate the drag coefficient

$$C_D = 2 + (C_{D0} - 2)e^{-3.07\sqrt{\gamma}g(Re)M/Re} + \frac{h(M)}{\sqrt{\gamma}M}e^{-Re/(2M)} \quad \text{Equation 3.20}$$

where C_{D0} is the particle drag coefficient in incompressible flow (where $M \ll 1$) and γ is the ratio of the specific heats. Moreover, $h(M)$ and $g(Re)$ are as follows

$$h(M) = \frac{5.6}{1+M} + 1.7 \sqrt{\frac{T_d}{T_c}} \quad \text{Equation 3.21}$$

$$g(Re) = \frac{1+Re(12.278+0.548Re)}{1+11.278Re}$$

where T_d , and T_c are the droplet/particle and carrier gas temperatures, respectively [21].

The heat and mass transfer between multicomponent droplet and gas phase is simulated according to the laws clarified in [1, 32]. The lumped capacity method is used to simulate the drop/particle heat transfer

$$m_d C_d \frac{dT_d}{dt} = hS(T_c - T_d) \quad \text{Equation 3.22}$$

where C_d , S , and h are the drop/particle specific heat, the drop/particle surface area, and the heat transfer coefficient, respectively. The Ranz-Marshall equation is used to estimate the Nusselt number (Nu) and the heat transfer coefficient

$$Nu = \frac{hd}{\lambda_c} = 2 + 0.6Re_p^{1/2} Pr^{1/3} \quad \text{Equation 3.23}$$

where Pr is the gas phase Prandtl number [21]. The following equation is applied to compute the evaporation rate when the droplet temperature is between the vaporization and boiling temperatures

$$\frac{dm_i}{dt} = k_{m,i} S \rho_c \ln(1 + B_{m,i}), B_{m,i} = \frac{Y_{i,s} - Y_{i,\infty}}{1 - Y_{i,s}} \quad \text{Equation 3.24}$$

where $k_{m,i}$ is the mass transfer coefficient of component i , $Y_{i,s}$ and $Y_{i,\infty}$ are the mass fraction of vapor at the droplet surface and in the bulk gas, respectively. The Spalding mass number of

component i , is denoted by $B_{m,i}$ [29]. During droplet evaporation, the heat transfer coefficient is calculated from the below equation

$$Nu = \frac{hd}{\lambda_c} = \frac{\ln(1+B_T)}{B_T} (2 + 0.6Re_p^{1/2} Pr^{1/3}) \quad \text{Equation 3.25}$$

where B_T is the Spalding heat transfer number [29]. Considering the vaporization effect, the droplet heat transfer equation is as follows (h_{fg} is the latent heat of evaporation)

$$m_d C_d \frac{dT_d}{dt} = hS(T_c - T_d) + \sum_i \frac{dm_i}{dt} h_{fg,i} \quad \text{Equation 3.26}$$

During the boiling process, the droplet heat transfer equation is as follows

$$\sum_i \frac{dm_i}{dt} h_{fg,i} = hS(T_d - T_c) \quad \text{Equation 3.27}$$

The particle melting (the mullite melting point is around 2110 K) process is modeled by defining the particle specific heat as a function of temperature. Particle melting estimation is described in detail in authors' previous paper [19].

The droplets secondary breakup is simulated using Taylor Analysis Breakup (TAB) model because the Weber number is relatively low near the injector. TAB model is based on Taylor's analogy [129] between a spring-mass system, and an oscillating-distorting droplet. In this model, the breakup of parent droplet into a number of smaller droplets occurs when the droplet oscillations grow to a critical ratio of the droplet radius. To determine the child droplets size, the parent droplet energy is equated to the child droplets combined energy. Moreover, the mass conservation equation is used to determine the number of child droplets [29, 129].

3.3 Results and Discussions

The general characteristics of the gas flow before injecting the suspension is shown in Figure (3.3). Premixed combustion of oxygen-propylene makes the gas phase temperature and static gage

pressure to reach around 3300 K and 0.56 MPa in the combustion chamber. To simulate the phenomena involved in the experiments, nitrogen is injected through the center port into the combustion chamber. Consequently, the gas temperature near the nozzle centerline is lower than the gas temperature near the fuel/oxygen inlet. In other words, the highest temperature zones are not located very close to the centerline where the particles move (similar results can be found in the literature such as [5, 130, 131]). The gas flow accelerates inside the converging part of the nozzle and gets choked at the nozzle throat. Consequently, the gas flow expands in the diverging part of the nozzle (it reaches around 2000 m/s at the nozzle exit) and a supersonic overexpanded jet develops outside the nozzle.

As it is clearly indicated in Figure (3.3), the gas centerline temperature increases in the converging section of the nozzle until it reaches the maximum value of 2370 K near the nozzle throat. Then the gas temperature reduces in the divergent part of the nozzle and reaches 1850 K at the nozzle exit. Figure (3.3) also reveals that seven or possibly eight shock diamonds, which are a series of oblique shocks and Prandtl-Meyer fans, can be recognized outside the nozzle. Immediately after each shock, the gas temperature and pressure increase significantly and its velocity reduces considerably. Hence, the heat transfer rate from the gas phase to the particles increases in this region. In other words, the shock diamonds should be captured precisely to accurately predict the particle temperature and velocity. It is known from the experiments that seven to nine shock diamonds are observable in a typical HVOF/suspension HVOF process [132]. Therefore, the mesh is capable of resolving the shock diamonds and there is a good agreement between the numerical results and the experimental data.

The gas flow characteristics after suspension injection are also demonstrated in Figure (3.3). Ethanol and ethylene glycol evaporation results in reduction of the gas temperature inside the

combustion chamber (similar behavior is discussed in [30-34, 118, 133]). Noting that the centerline temperature inside the combustion chamber does not change since nitrogen is injected into the chamber for both cases. In addition, the gas temperature in the nozzle throat and its diverging part increases since the non-premixed combustion of oxygen-vapor ethanol and oxygen-vapor ethylene glycol is still active.

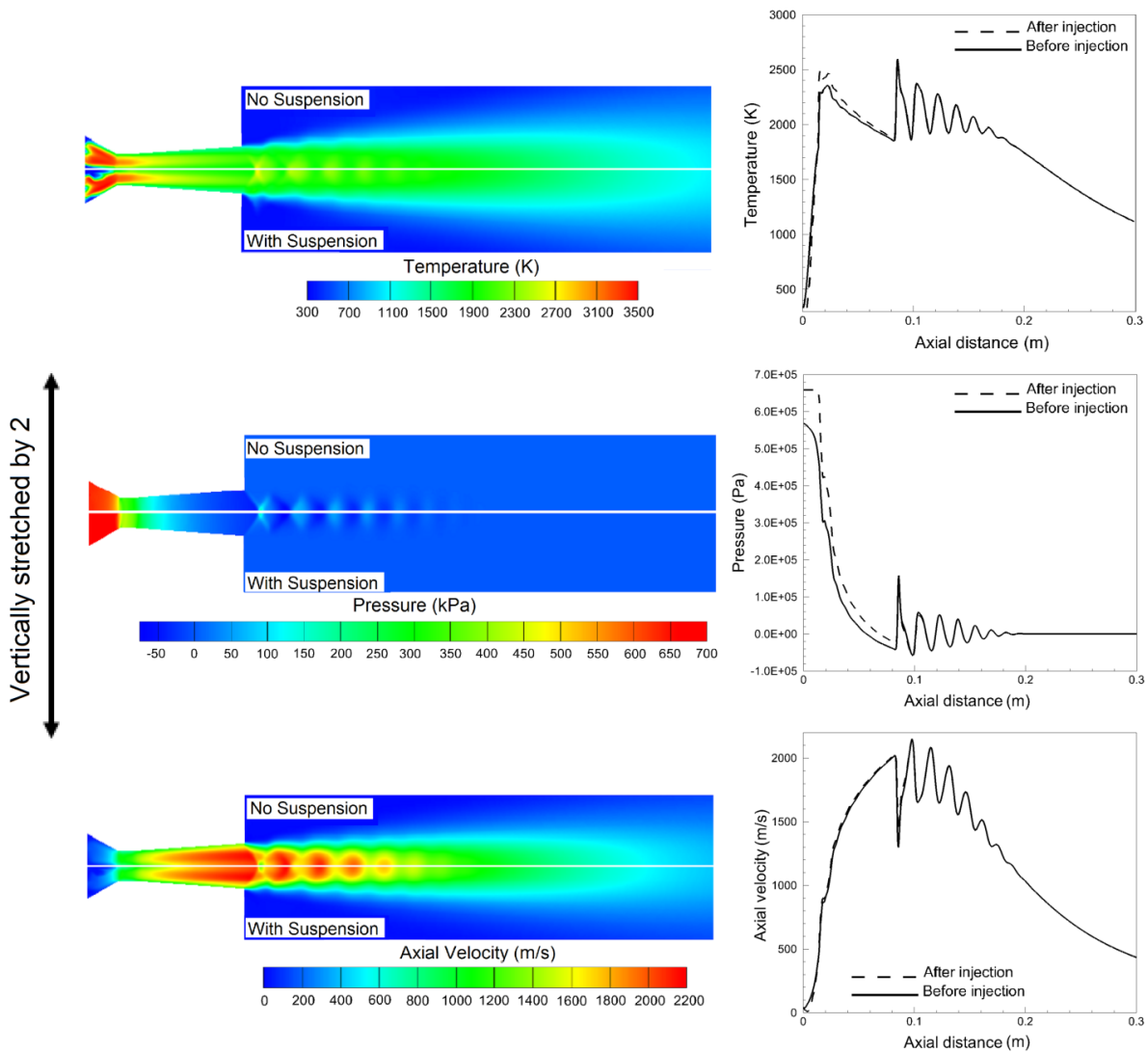


Figure 3.3 Effect of suspension injection on the gas flow; (left) gas flow contours and (right) along centerline

The effect of suspension injection and evaporation/combustion on the gas pressure is one of the key points of this study. It is known from the experiments that when suspension is injected into the combustion chamber, a significant rise of the pressure inside the combustion chamber, and a strong disturbance of the free expanding hot gas stream occur due to the presence of vapor [10, 18, 112]. As it is shown in Figure (3.3), the combustion chamber gage pressure increases to 0.657 MPa due to suspension evaporation/combustion. Berghaus and Marple [117] indicated that the suspension is delivered against the combustion backpressure of up to 0.655 MPa, which is in agreement with the results of the current study. The mass fractions of propylene, ethanol vapor and ethylene glycol vapor are shown in Figure (3.4). As clearly indicated in Figure (3.4), the maximum evaporation occurs inside the combustion chamber. After ethanol vaporization, ethylene glycol evaporation becomes dominant. These outcomes are similar to the results presented by Gozali *et al.* [32].

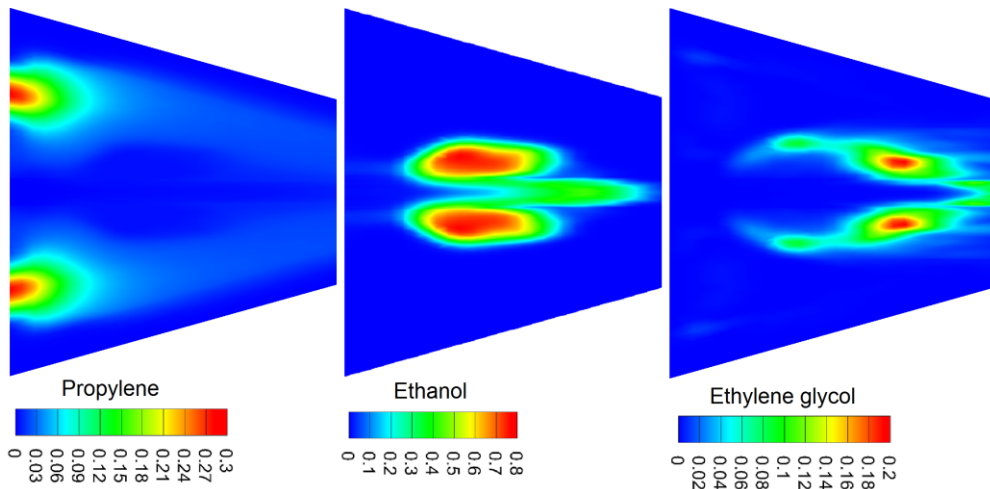


Figure 3.4 Mass fraction of propylene, gaseous ethanol, and gaseous ethylene glycol inside the combustion chamber

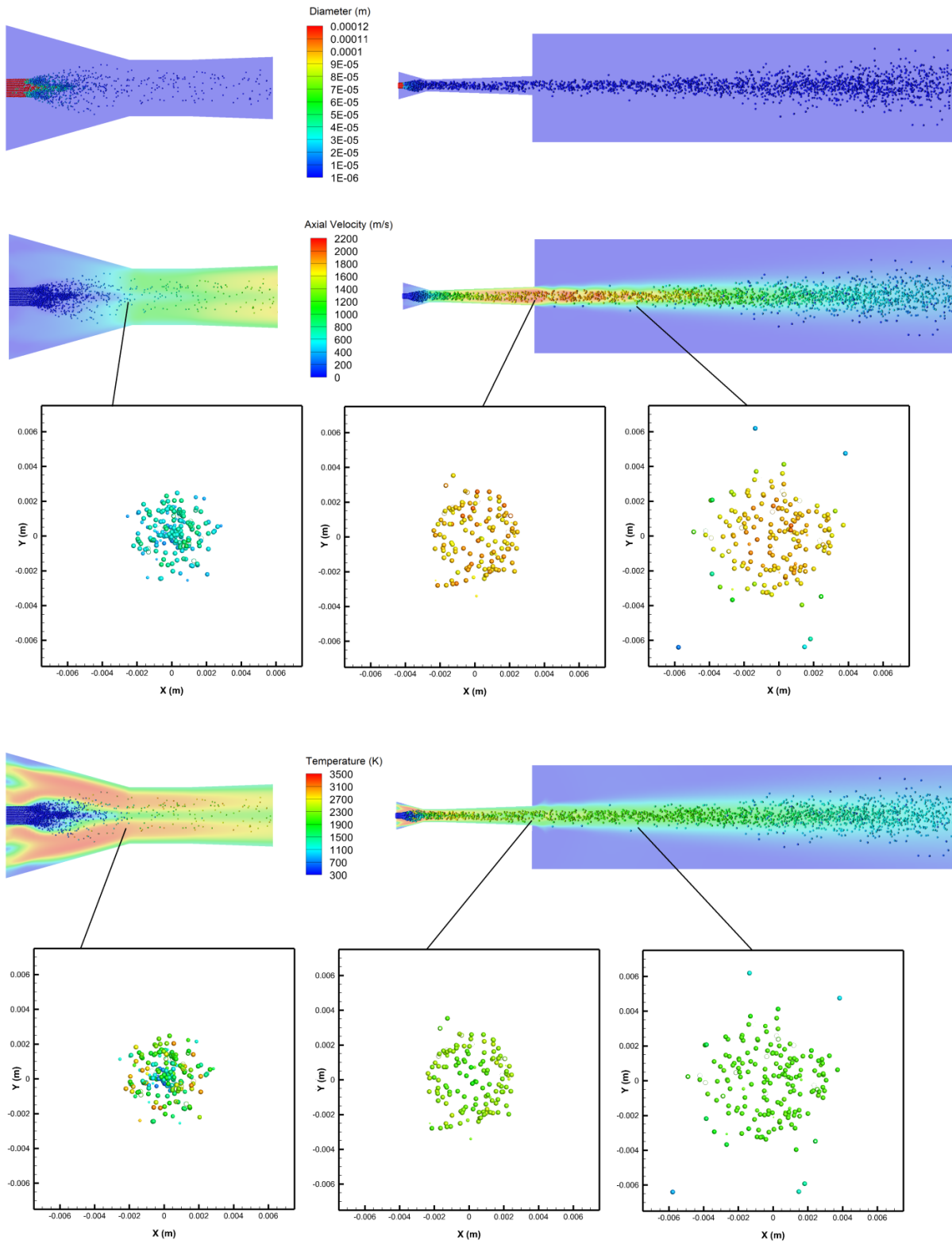


Figure 3.5 Suspension/particle size, temperature, and velocity distributions within the computational domain

Figure (3.5) shows suspension/particle size, temperature, and velocity distributions in the computational domain. The left column of the figure shows the suspension droplets behavior inside the combustion chamber in more details. The suspension droplets experience fragmentation up to the middle of the combustion chamber. It is demonstrated that 120 μm suspension droplets injected into the combustion chamber, undergo fragmentation into small 1-2 μm diameter droplets. After completion of the breakup process, ethanol and ethylene glycol evaporate (see Figure (3.4)) and the coating particles (mullite) are tracked through the domain. To compare the numerical results with the experiments [117], the median particle diameter (d_{50}) is used. In the current study, the median particle diameter is $d_{50}=1.66 \mu\text{m}$, while the median diameter of the solid particles and agglomerates in suspension feedstock was $d_{50}=1.8 \mu\text{m}$ in the experimental study [117]. This means that solid particle diameter is well predicted. Furthermore, particles can reach to maximum temperature of 3170 K in the combustion chamber. Moreover, due to rather small size particles used in suspension HVOF, particle velocity rapidly reaches to the gas velocity (i.e. up to 2000 m/s at the nozzle exit) as shown in Figure (3.5). To study the effect of gas flow especially the shock diamonds on the particle trajectory deviation, the particle distribution at three different planes (i.e. nozzle throat entrance, nozzle exit, and a plane inside the shock diamonds with a standoff distance of 45mm) are also shown in Figure (3.5). As it is clearly demonstrated in Figure (3.5), the particle trajectory deviation generally begins inside the shock diamonds. For the particles moving near the centerline, the trajectory deviation occurs, and for the particles moving away from the centerline, the trajectory deviation magnifies.

The comparison between the gas and particle characteristics inside and outside the nozzle along the centerline is illustrated in Figure (3.6). As it is shown, the particles are repeatedly decelerated and accelerated while passing through the shock diamonds. However, the effect of shock diamonds

on variations of particle temperature is negligible (due to low thermal conductivity and high specific heat capacity of mullite [123-125]). After shock diamonds, particle temperature and its velocity are decreased dramatically.

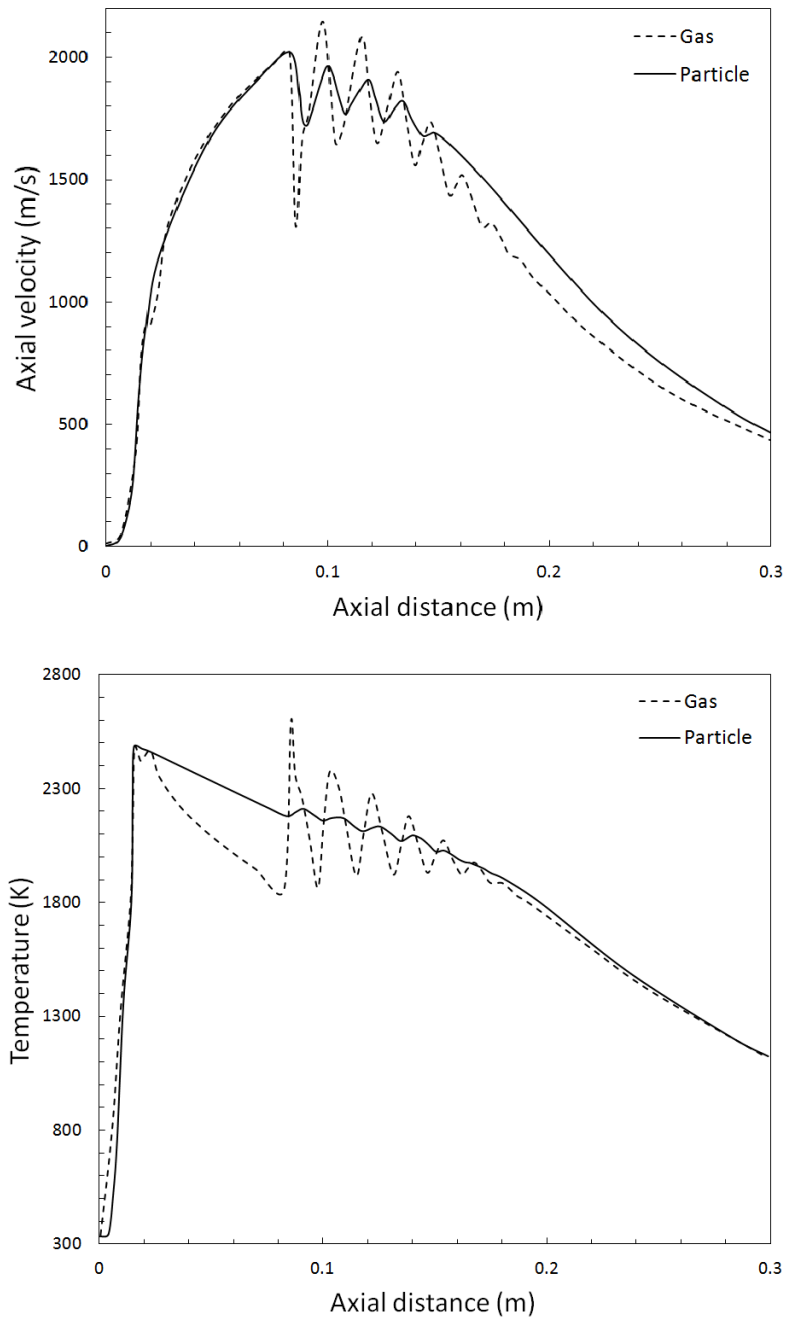


Figure 3.6 Comparison between the gas and particle characteristics along the centerline

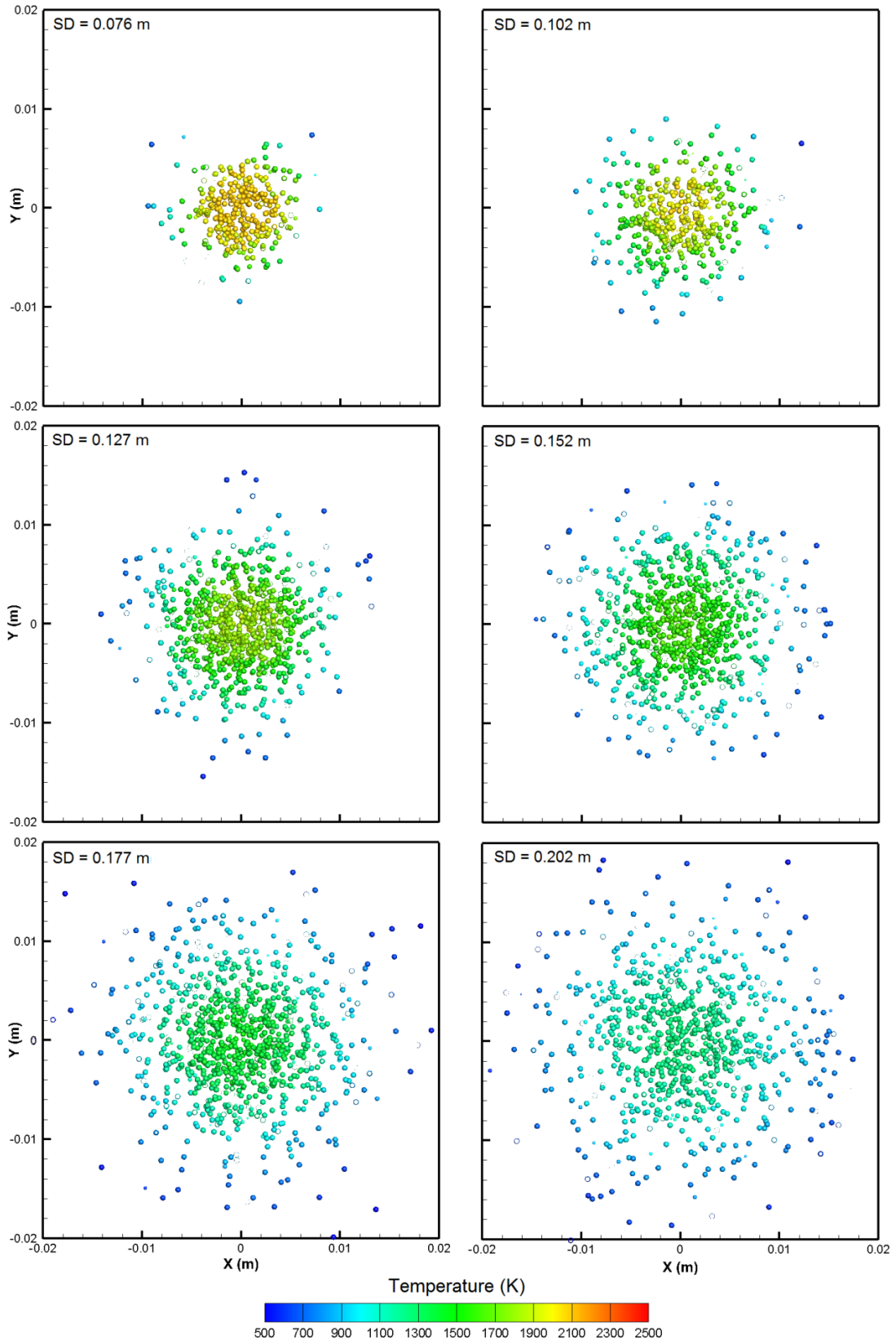


Figure 3.7 Particle temperature and spatial distributions at different standoff distances (SD)

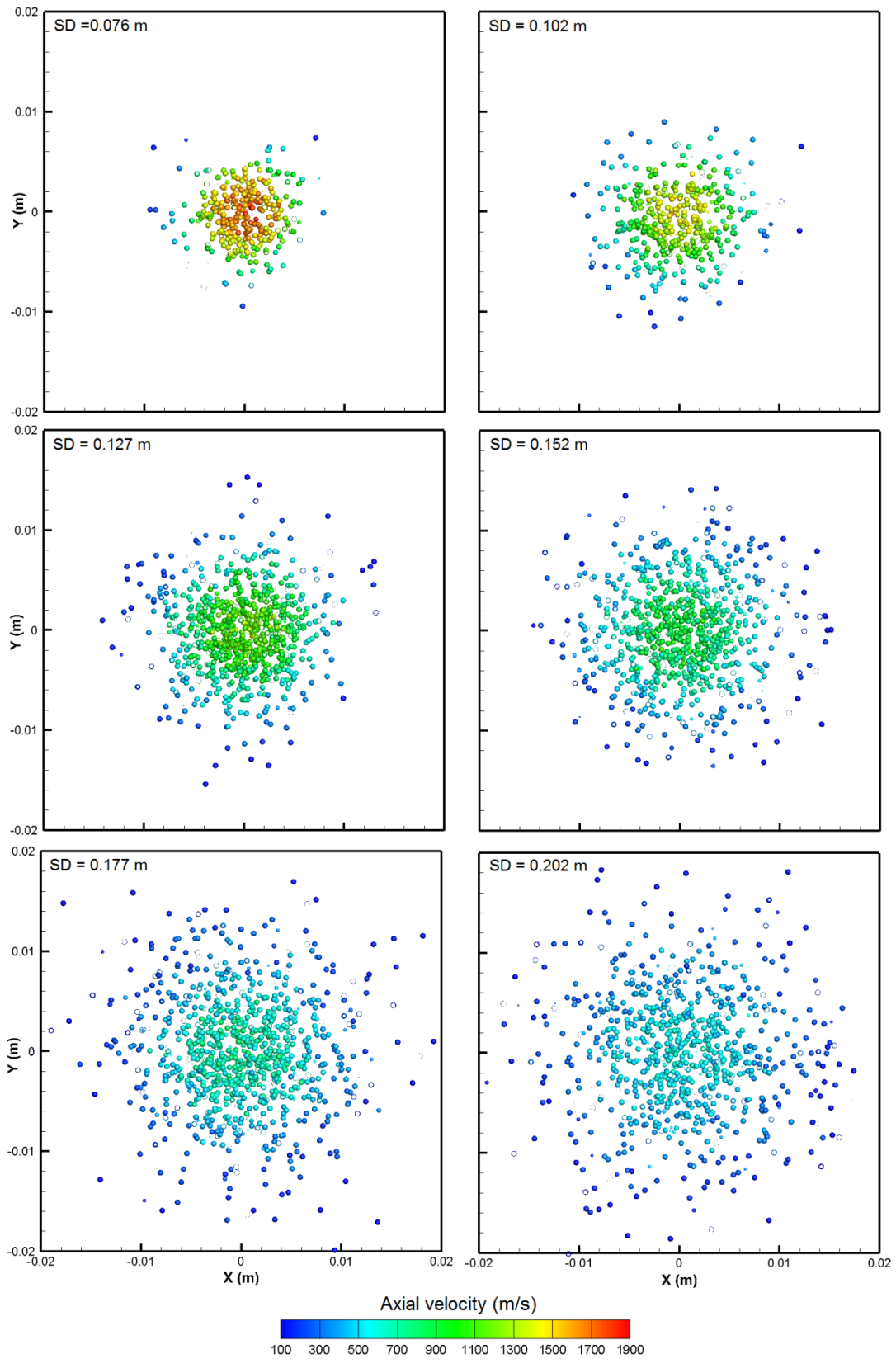


Figure 3.8 Particle velocity and spatial distributions at different standoff distances (SD)

To study the effect of substrate standoff distance, particle velocity, temperature and footprints at standoff distances (SD) between 76 and 202 mm are shown in Figures (3.7) and (3.8). As can be seen, the particle spatial distribution rapidly widens as the standoff distance increases, resulting in nonlinear particle trajectories (contrary to a typical HVOF process). A correlation to determine spray cross section diameter as a function of standoff distance is derived as follows

$$d_{spray} = 0.55(SD)^{1.6} + 0.006 \quad \text{Equation 3.28}$$

where d_{spray} and SD are in meter. In addition, both the particle temperature and the velocity are decreased by increasing the standoff distance. Therefore, it is expected that the coating porosity grows as the standoff distance increases (similar behavior is discussed in [19, 35] for suspension plasma spraying). Berghaus and Marple [117] experimentally proved that an increase in the standoff distance leads to porosity growth because of the reduction in particle velocity and temperature.

Figures (3.9) and (3.10) show the variations in particle velocity and temperature as a function of standoff distance for both experimental and numerical studies. Berghaus and Marple [117] measured the in-flight particle states with a commercial diagnostic system (AccuraSpray[®], Tecnar, St-Bruno, Canada). The ensemble average data representing the in-flight particle conditions in a measurement volume of approximately $\text{Ø}3 \times 25 \text{ mm}^2$ is provided by AccuraSpray system [134, 135]. The velocity was determined by a time-of-flight technique, and the temperature measurement was based on two-color pyrometry. At short standoff distances, (i.e. $SD=76 \text{ mm}$), particle characteristics measurements were impeded by the existence of shock diamonds in the supersonic jet. Therefore, there are large error bars which indicate considerable uncertainty in the measurements close to the nozzle exit. However, confidence to the measurements increases as standoff distance rises. The numerical results are the average of the temperature and velocity of

the particles at each standoff distance. The same measurement volume as experiment is assumed around each standoff distance and the characteristics of the particles that are located inside the measurement volume are saved at different times. The code was run 5 times, and then the particle temperatures and velocities were averaged.

In general, Figures (3.9) and (3.10) show that the numerical results are in good agreement with the experiment and the variation trend seems to be similar. However, there exist differences between experimental and numerical results especially for low standoff distances. Many factors can cause the mentioned deviation. From the experimental point of view, although the in-flight particle sensors such as DPV-2000, Accuraspray, SprayWatch, and SprayCam use similar methods to measure the particle states, the values of particle temperature and velocity given by these sensors can be noticeably different [136-138]. In addition currently used devices are not capable of fully detecting nano particles. Therefore, the present data mostly corresponds to the properties of relatively large particles which lead to uncertainties in measurement. Furthermore, particle agglomeration might occur during suspension evaporation or when suspension is stored in the container. Therefore, the average particles size inside the HVOF torch can be larger than $d_{50}=1.8 \mu\text{m}$ which is given in the experimental study [117]. As the particle size increases, the magnitude of the particle acceleration and velocity decrease. Therefore, the residence time of the particle in the high temperature zone increases and the particle temperature rises. In addition, lack of accurate atomization model can be another reason of the error. Although TAB model is widely used to simulate the secondary breakup in suspension HVOF process, this model is not capable of capturing the suspension nozzle effects on atomization, and primary breakup. Therefore, more accurate models such as Volume of Fluid (VOF) are needed to simulate the atomization process and to estimate the average droplet size precisely [1, 53, 66, 139, 140].

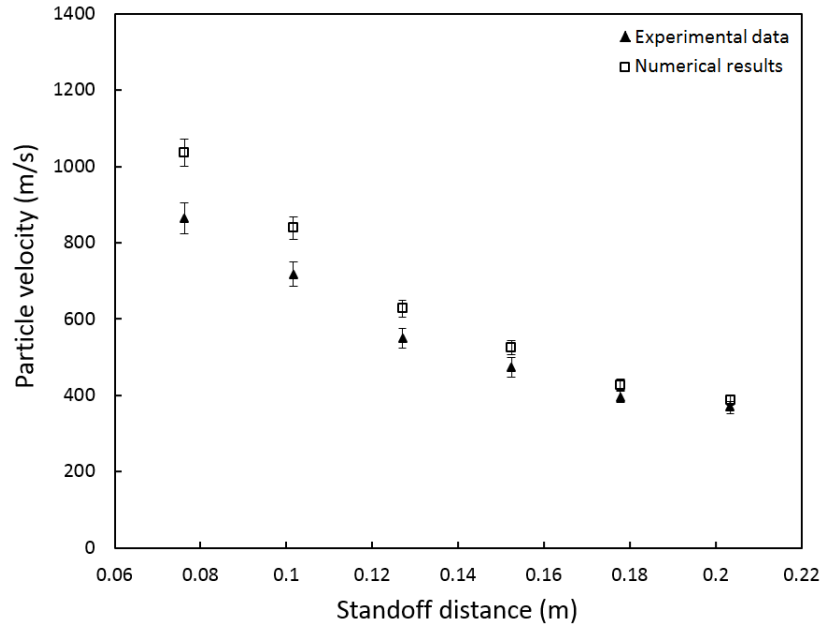


Figure 3.9 Comparison between numerical and experimental [117] results for particle velocity at different standoff distances (*SD*)

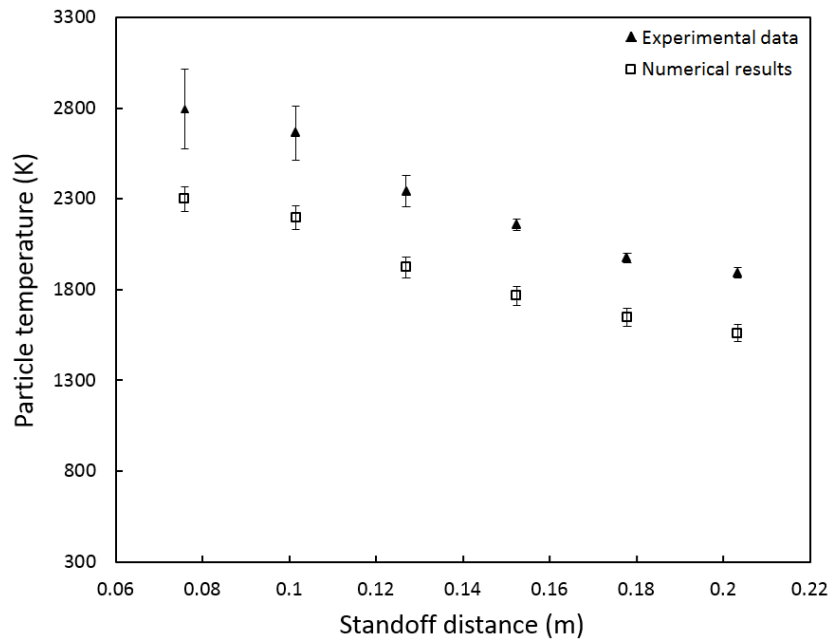


Figure 3.10 Comparison between numerical and experimental [117] results for particle temperature at different standoff distances (*SD*)

3.4 Summary and Conclusions

Suspension HVOF process includes complex phenomena such as reactive compressible multiphase flow with suspension atomization. In this study, a model based on Eulerian-Lagrangian approach is proposed to estimate the droplet/particle temperature, velocity, and trajectory in the suspension HVOF process. A suspension with known concentration is simulated by a multicomponent mixture model. The suspension includes 5wt.% mullite powder ($3\text{Al}_2\text{O}_3 \cdot 2\text{SiO}_2$), 65wt.% ethanol and 30wt.% ethylene glycol to mimic the exact conditions used in the experimental study presented in [117]. Taylor Analogy Breakup (TAB) model is applied to simulate the breakup process. Propylene-oxygen, ethanol-oxygen, and ethylene glycol-oxygen reactions are modeled by eddy dissipation model. Particles are tracked through the domain after completion of the suspension breakup and evaporation/combustion. Gas phase pressure and temperature are well matched with the experiments. A correlation is proposed to determine spray cross section diameter as a function of the standoff distance that indicates the nonlinear behavior of particle trajectories. In general, the predicted particle velocity, temperature and diameter are in good agreement with the experiments [117]. It was shown that as the standoff distance increases, the particle velocity and temperature decrease.

Chapter 4

Numerical Simulation of Primary Breakup of Round Nonturbulent Liquid Jets in Shear-Laden Gaseous Crossflow

“Reprinted from the paper accepted by journal of Atomization and Sprays, [141], with permission”

Abstract

Numerical modeling results for the primary breakup of the round nonturbulent liquid jets in shear-laden gaseous crossflow at atmospheric pressure are presented in this article. A coupled level set and volume of fluid method together with the large eddy simulation turbulence model implemented in the CFD open source solver library (OpenFOAM[®]) are applied to simulate the primary breakup and to track the gas-liquid interface accurately. In the volume of fluid method, the volume fraction is advected algebraically using a compression scheme. To simulate the shear-laden crossflow, linear velocity profiles with various positive and negative slopes are considered at the inlet boundary condition. Based on the average crossflow velocity, two values of Weber number, 50 and 100, and for each of them, two values of liquid to gas momentum flux ratio, 5 and 20, are considered. The effect of crossflow nonuniformity on the liquid jet penetration, the location of column breakup point, and the liquid surface waves are investigated and compared with the experimental and numerical

results in the literature. The results indicate that nonuniform crossflow has considerable effects on the liquid jet behavior especially on its penetration height and column breakup point. While the liquid is injected from the top of the computational domain and the positive y -direction is downward, a parameter is defined as the ratio of gas velocities at the bottom and top of the inlet boundary to display the slope of the linear velocity profiles. The crossflow nonuniformity effect is magnified when the mentioned parameter increases, resulting in a significant increase of the liquid jet penetration height. Moreover, general correlations for liquid penetration height, based on experimental and numerical results, are developed in this study.

4.1 Introduction

Liquid jet in gaseous crossflow has numerous applications such as fuel injection in gas turbines, ramjets, scramjets [40, 45, 142-150], and solution/suspension injection in thermal spray torches to generate nanostructured coatings [1, 19, 35, 101, 106-110, 139]. Over the past decades, there were tremendous experimental and numerical studies on liquid jets behavior in crossflow (e.g. [40-46, 142-153]). In general, liquid jet in subsonic gaseous crossflow can be divided into three categories: 1) injection of nonturbulent liquid jet into a uniform crossflow, 2) injection of turbulent liquid jet into a uniform crossflow, and 3) injection of turbulent liquid jet into a nonuniform crossflow.

Injection of nonturbulent liquid jet into a uniform crossflow was investigated by Mazallon *et al.* [44] and Sallam *et al.* [46] using pulsed shadowgraphy and holography techniques. Four breakup regimes namely column, bag, multimode, and shear breakup were observed. Lee *et al.* [42] studied the behavior of turbulent liquid jets injected into a uniform crossflow. It was shown

that for a turbulent liquid jet, bag and multimode breakup regimes are not observed at low Weber numbers. Moreover, it was revealed that the column breakup distance for the turbulent liquid jet is smaller than that for the nonturbulent liquid jet. Xiao *et al.* [153] used the coupled level set and volume of fluid method along with large eddy simulation (LES) method to model the primary breakup of a liquid jet injected into an air crossflow. The behavior of a nonturbulent liquid jet injected into a nonturbulent crossflow was studied initially. Regular waves were detected on liquid jet surface, and it was demonstrated that the wavelength decreases as the gaseous Weber number increases. The next step was simulation of turbulent liquid jet injection into a turbulent air crossflow. It was revealed that the liquid turbulence rather than the gaseous turbulence determines the liquid jet instabilities and interface characteristics. Herrmann [151] used the balanced force refined level set grid method to investigate the primary atomization of a turbulent liquid jet injected into a crossflow. He applied an algorithm to transfer broken off, small scale nearly spherical drops into a Lagrangian point particle description. All the nondimensional numbers except for the density ratio were matched with the experimental data. It was shown that the liquid jet atomization occurs via two simultaneous breakup mechanisms. In the first mode, instability waves on the jet surface, especially on the windward side, grow and form baglike structures. Then in the second, at the liquid jet sides and near the nozzle exit, corrugations on the jet surface are stretched out into ligaments. Herrmann [41] developed his model to study the effect of density ratio on primary atomization of a turbulent liquid jet in crossflow. It was revealed that the density ratio has significant effects on jet penetration and droplet size distribution. Farvardin and Dolatabadi [154] modeled the primary breakup of biodiesel and diesel jets injected into a crossflow using volume of fluid and large eddy simulation (i.e. constant coefficient one-equation eddy-viscosity model) methods. Their results showed lower penetration height of biodiesel jet comparing to the diesel jet

due to higher viscosity of biodiesel. Li and Soteriou [152, 155] also used the coupled level set and volume of fluid method to simulate the liquid jet atomization in crossflow. Ghost fluid method was also applied to facilitate simulations at high density ratio. In addition, Lagrangian droplet model and Adaptive Mesh Refinement (AMR) were applied to efficiently capture the multiple scales simultaneously. It was shown that AMR approach is capable of capturing the near-field details of liquid jet atomization at notably reduced cost [152]. In their study, the column trajectory, breakup location, and surface wavelength were also calculated at different inlet boundary conditions and compared with the experimental data [155].

Nonuniform crossflow such as swirling and shear-laden was only considered in few experimental studies [47-50, 156-158]. Tambe *et al.* [47, 49, 50] performed experiments to investigate the behavior of liquid jets injected into shear-laden crossflow. By dividing the wind tunnel into two components and introducing two independent streams, quasi-linear gas velocity profiles were produced. They used particle image velocimetry (PIV), phase Doppler particle anemometry (PDPA), and Mie-scattering techniques to measure jets penetration, velocity distribution, volume flux distribution and droplet size. They revealed that spray properties, especially penetration height, are strong function of the gas velocity profile [47, 49, 50]. Becker and Hassa [156] investigated the effect of ambient air pressure and the liquid-to-gas momentum flux ratio (q) on liquid jets injected into a counter-swirling, double annular crossflow. It was shown that the initial liquid placement reacted sensitively to the variation of q . Furthermore, the spray susceptibility to dispersion because of turbulent mixing and centrifugal forces was mainly dependent on droplet diameters. Noting that droplet diameter itself is a function of operating pressure. Gong *et al.* [157] studied the lean direct wall injection (LDWI) concept, where the liquid jets were injected into a swirling flow at various injection angles. They found that for LDWI, the

breakup phenomena were strong functions of jet inclination angle, liquid-to-gas momentum flux ratio, swirl number, and injector diameter. In their study, the optimum jet inclination angles for reaching uniform atomization were presented based on the swirler vane angles. Tambe and Jeng [48] also measured the velocity distribution and penetration of liquid jets injected into a swirling crossflow for various swirl angles, and liquid-to-gas momentum flux ratios. Using cylindrical coordinate system, it was shown that radial penetration amplifies with increasing the momentum flux ratio. On the other hand, increasing the swirl angle resulted in a lower radial and higher circumferential penetrations. Sikroria *et al.* [158] also measured the breakup length and penetration height of liquid jets injected into a swirling crossflow. They indicated that instability column waves have significant effects on jet breakup phenomena in swirling crossflow. The column fracture mode was affected by these disturbances in such a way that the liquid penetration reduced with increasing the momentum flux ratio for some cases. In addition, they showed that the swirling flows were capable of producing shorter breakup lengths, and smaller spray droplet size.

The fact that crossflow in many applications such as thermal sprays [1, 19, 35] is not uniform and includes severe velocity gradients, makes it crucial to study the effect of nonuniformities on liquid jet behavior, and spray properties fundamentally. In this article, near field (where the phase interface cannot be observed brightly by traditional experimental methods) behavior of a liquid jet in shear-laden crossflow, i.e. penetration, deformation, turbulence interaction, and primary breakup is studied numerically. The shear-laden crossflow is the focus of the current work, as it is the simplest nonuniform flow that gives fundamental insights into the process of liquid jets primary breakup. In addition, it can be assumed as a simplified representative for the swirl flow [47].

4.2 Numerical Modeling

4.2.1 Numerical Method

The Volume of Fluid (VOF) solver in OpenFOAM version 2.1.1 (OpenCFD Ltd.), which is a CFD open source solver library, is used to simulate the primary breakup of the liquid jet in shear-laden crossflow. Supplementary details of the VOF method implementation in OpenFOAM can be found in the work of Rusche [67]. The incompressible momentum equation together with volume fraction (α) conservation equation are solved in incompressible VOF solver (InterFOAM). In VOF method, the function α , represents the volume fraction of the cell occupied by liquid. Therefore, $\alpha=0$ and $\alpha=1$ correspond to a cell full of gas and liquid, respectively. Furthermore, $0<\alpha<1$ corresponds to a surface cell and shows the interface location [53, 55]. The volume fraction in the solver is advected algebraically using an artificial compression term to mitigate the effects of numerical smearing of the interface [55]. The surface tension force which is dependent on the surface curvature is included in the momentum equation as the continuum surface force [54, 55]. The governing equations solved in the incompressible VOF (InterFOAM) model are given below

Momentum equation

$$\frac{\partial \rho \mathbf{U}}{\partial t} + \nabla \cdot (\rho \mathbf{U} \mathbf{U}) = -\nabla p + \rho \mathbf{g} + \nabla \cdot (\mu (\nabla \mathbf{U} + \nabla \mathbf{U}^T)) + \sigma \kappa \nabla \alpha \quad \text{Equation 4.1}$$

where \mathbf{U} is the velocity vector, ρ is density, μ is viscosity, t is time, p is pressure, \mathbf{g} is the gravitational acceleration, σ is the surface tension, and κ is the free surface curvature. Noting that the last term on the right hand side of the momentum equation is surface tension force.

The free surface curvature is calculated from the phase fraction, α , as

$$\kappa = -\nabla \cdot \left(\frac{\nabla \alpha}{|\nabla \alpha|} \right) \quad \text{Equation 4.2}$$

Large eddy simulation (LES) turbulence model is coupled with the VOF method to capture vortices in both phases accurately [105, 159, 160]. In LES, by filtering the momentum equation,

the sub-grid scale (SGS) stress tensor comes from the convective term. The constant coefficient one-equation eddy-viscosity model is used to approximate the SGS stress tensor based on the turbulent kinetic energy (k_{sgs}) and SGS kinematic viscosity as follows [105, 154, 161]

$$\boldsymbol{\tau}_{sgs} = \overline{\mathbf{U}\mathbf{U}} - \overline{\mathbf{U}}\overline{\mathbf{U}} = \frac{2}{3}k_{sgs}\mathbf{I} - \frac{\mu_{sgs}}{\rho}(\nabla\mathbf{U} + \nabla\mathbf{U}^T) \quad \text{Equation 4.3}$$

$$\frac{\partial k_{sgs}}{\partial t} + \nabla \cdot (k_{sgs}\overline{\mathbf{U}}) = \nabla \cdot \left((\vartheta + \vartheta_{sgs})\nabla k_{sgs} \right) - \varepsilon - \vartheta_{sgs}\overline{S}^2 \quad \text{Equation 4.4}$$

where \overline{S} , ϑ_{sgs} , and ε are as follows

$$\overline{S} = \frac{1}{2}(\nabla\mathbf{U} + \nabla\mathbf{U}^T) \quad \text{Equation 4.5}$$

$$\vartheta_{sgs} = \Delta c_k k_{sgs}^{0.5}, \quad c_k = 0.07 \quad \text{Equation 4.6}$$

$$\varepsilon = \Delta c_\varepsilon k_{sgs}^{1.5}, \quad c_\varepsilon = 1.05 \quad \text{Equation 4.7}$$

The PISO scheme is applied to calculate the pressure and velocity fields using a geometric-algebraic multigrid (GAMG) solver. The readers are referred to sources such as Deshpande *et al.* [55] for detailed formulations.

Volume fraction equation

$$\frac{\partial \alpha}{\partial t} + \mathbf{U} \cdot \nabla \alpha + \nabla \cdot (\mathbf{U}_c \alpha (1 - \alpha)) = 0 \quad \text{Equation 4.8}$$

To prevent smearing of the interface, an extra artificial compression term (the third term) is defined in the volume fraction equation (Equation (4.8)) and at the same time, avoids the interface reconstruction [55]. This artificial term is active only at the interface region. \mathbf{U}_c is the vector of relative velocity normal to the interface

$$\mathbf{U}_c = \mathbf{n} \min \left[C_\alpha \frac{|\varphi|}{|S_f|}, \max \frac{|\varphi|}{|S_f|} \right] \quad \text{Equation 4.9}$$

where \mathbf{n} , C_α , φ , and S_f are face unit normal flux, compression coefficient, the face volume flux, and cell face area vector, respectively. Based on the work of Rusche [67], $C_\alpha = 1.5$. The face unit normal is given as follows

$$\mathbf{n} = \frac{\nabla\alpha}{|\nabla\alpha + \delta_n|} \quad \text{Equation 4.10}$$

where δ_n is used to avoid zero value at the denominator of \mathbf{n} [55]. The multidimensional universal limiter with explicit solution (MULES) method is used to solve the volume fraction advection equation [55].

In this study, based on the work of Albadawi *et al.* [68], Level Set (LS) method is used to improve the accuracy of the InterFOAM solver in terms of surface tension calculation and interface curvature. It was shown that the interface curvature and the surface tension force computations are considerably improved by their algorithm [66, 68, 162]. It should be noted that in LS method, the free surface is represented by a smooth function (level set function (ϕ)). The interface is captured by the zero level set, while the positive and negative values of level set function define liquid and gas regions, respectively [72].

In the work of Albadawi *et al.* [68], although the volume fraction field and the level set functions are defined, the volume fraction advection equation is solved only. The level set function (ϕ) is initialized in each time step using the advected volume fraction [68]. The volume fraction which equals to 0.5, is defined as the initial zero level set, as below

$$\phi_0 = 1.5 \Delta x (\alpha - 0.5) \quad \text{Equation 4.11}$$

where Δx is the mesh size. This initial level set function has the positive and negative values in the liquid and the gas regions, respectively. The next step is solving the re-initialization equation with a pseudo time (ς) in order to assign the level set function to a signed distance function [66, 68, 70, 72]

$$\frac{\partial\phi}{\partial\varsigma} = \text{sign}(\phi_0)(1 - |\nabla\phi|) \quad \text{Equation 4.12}$$

Computing the interface normal, and curvature (κ), by LS method is simple and accurate [66, 68, 70, 72]. These parameters are calculated as follows

$$\mathbf{n} = \frac{(\nabla\phi)}{|\nabla\phi|} \quad \text{Equation 4.13}$$

$$\kappa = \nabla \cdot \mathbf{n} \quad \text{Equation 4.14}$$

Therefore, the surface tension force is modified and computed as

$$F_\sigma = \sigma\kappa(\phi)\delta(\phi)\nabla\phi \quad \text{Equation 4.15}$$

where δ is Dirac function which is defined as below

$$\delta(\phi) = \begin{cases} 0, & |\phi| > \beta \\ \frac{1}{2\beta} \left(1 + \cos\left(\frac{\pi\phi}{\beta}\right) \right), & |\phi| \leq \beta \end{cases} \quad \text{Equation 4.16}$$

Based on the work of Albadawi *et al.* [68], $\beta = 1.5\Delta x$ is assumed in this study. The fluxes and the material properties such as density and viscosity are calculated based on the following Heaviside function

$$H_v(\phi) = \begin{cases} 0, & \phi < -\beta \\ \frac{1}{2} \left(1 + \frac{\phi}{\beta} + \frac{1}{\pi} \sin\left(\frac{\pi\phi}{\beta}\right) \right), & |\phi| \leq \beta \\ 1, & \phi > \beta \end{cases} \quad \text{Equation 4.17}$$

$$\rho(\phi) = \rho_g + (\rho_l - \rho_g)H_v(\phi) \quad \text{Equation 4.18}$$

$$\mu(\phi) = \mu_g + (\mu_l - \mu_g)H_v(\phi) \quad \text{Equation 4.19}$$

where ρ_g, ρ_l, μ_g and μ_l are the gas density, liquid density, gas viscosity, and liquid viscosity, respectively [66, 68, 70, 72]. The solver algorithm is summarized in Figure (4.1).

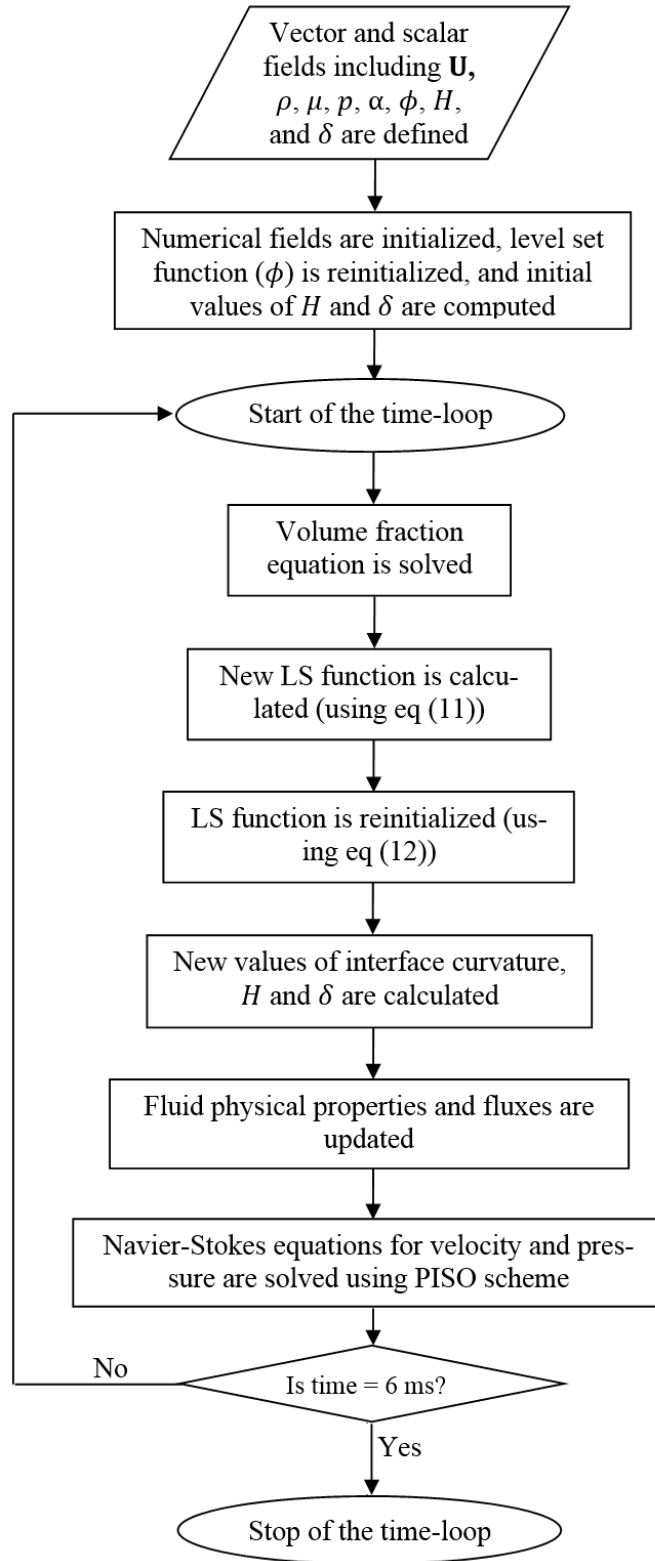


Figure 4.1 Flowchart of the S-CLSVOF solver in OpenFOAM proposed by Albadawi *et al.* [68]

4.2.2 Simulation Configuration

The computational domain and boundary conditions are schematically shown in Figure (4.2). The coordinate origin is at the top wall of the domain and the positive y -direction is downward. No-slip boundary condition is used for the top and bottom walls. Linear air velocity profiles with various positive and negative slopes are considered as the inlet boundary condition to simulate the shear-laden crossflow as below

$$U_x(y) = \left(\frac{U_{x,a} - U_{x,u}}{L} \right) y + U_{x,u} \quad \text{Equation 4.20}$$

where U_x is the inlet air velocity at x -direction, L is the height of the computational domain (=20 mm), $U_{x,u}$ and $U_{x,a}$ are the crossflow velocities at the top and bottom of the inlet boundary, respectively. Based on the work of Tambe *et al.* [47, 49, 50], the crossflow velocity ratio (U_R) and the crossflow average velocity ($U_{x,avg}$) are defined as follows

$$U_R = U_{x,a} / U_{x,u} \quad \text{Equation 4.21}$$

$$U_{x,avg} = (U_{x,u} + U_{x,a}) / 2 \quad \text{Equation 4.22}$$

In this study, a nonturbulent water jet that is obtained from nozzles with a small length/diameter ratio or supercavitating nozzles [44, 46, 149] is considered. Therefore, the water behavior inside the nozzle is not simulated. Instead, a circular hole on top of the domain is considered as the nozzle exit (the nozzle exit diameter (d_j), is 0.5 mm). Uniform velocity boundary condition is assumed at the nozzle exit (the water velocity at the circular hole is V), that illustrates air crossflow is the main reason of the primary breakup processes during the present study (see [46] and [152] for more information about the primary breakup of nonturbulent liquid jets in crossflow and the validation of this assumption). The gas Weber number ($We = \rho_g U_{x,avg}^2 d_j / \sigma$) and liquid-to-gas momentum flux ratio ($q = \rho_l V^2 / \rho_g U_{x,avg}^2$) are defined based on the average

crossflow velocity [47, 49, 50]. Similar to the experimental study of liquid jet injection in shear-laden crossflow [47, 49, 50], Weber numbers of 50 and 100, and two values of q , 5 and 20, are considered. Values of $U_{x,a}$, $U_{x,u}$, average U_x , U_R , We , and q for different cases are given in Table (4.1). Moreover, the inlet/outlet boundary condition is imposed on the lateral sides of the domain.

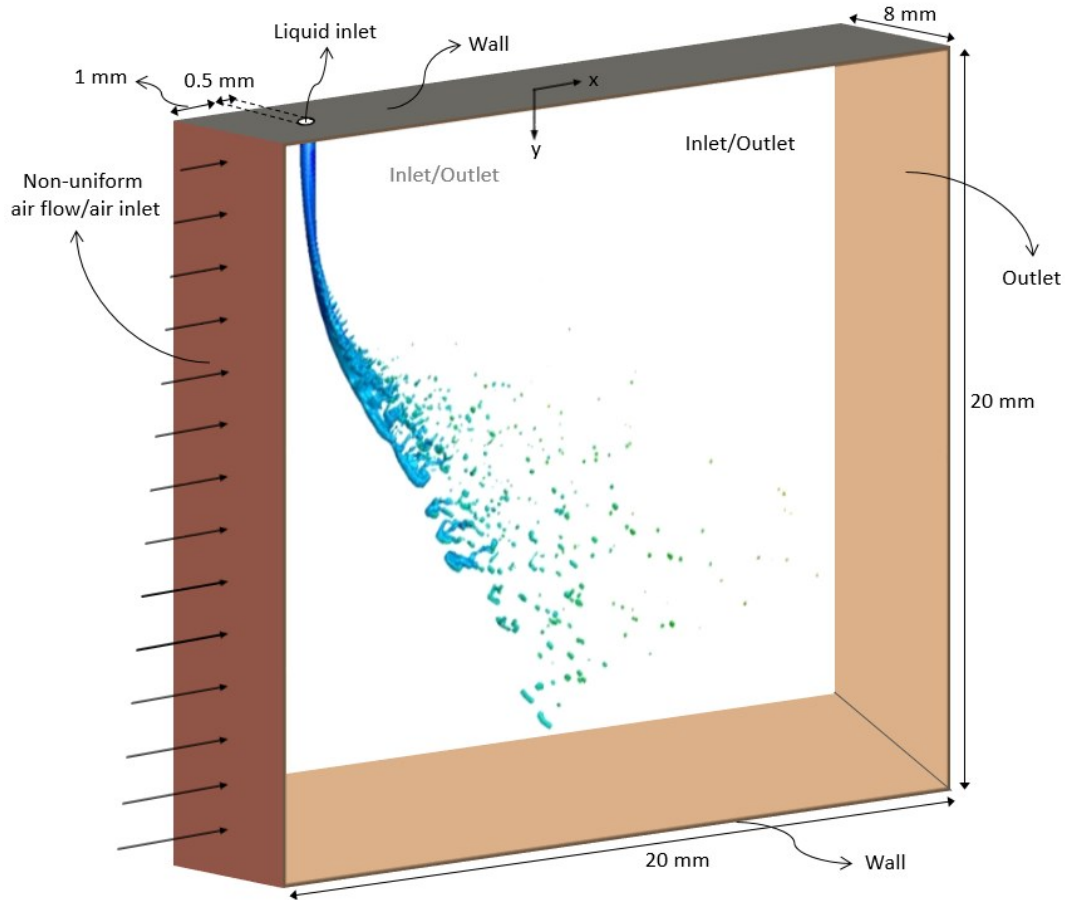


Figure 4.2 Computational domain and boundary conditions

The mesh is hexahedral, and at the initial time step, its size is about 0.08 mm (the minimum and the maximum grid sizes are 0.075 and 0.084 mm, respectively). Similar to our previous published works [105, 154, 161], dynamic adaptive mesh refinement method (interDyMFoam solver in OpenFOAM) with three refinement levels is used to refine the size of the cells located at

gas-liquid interface (i.e. where α is between 0.01 and 0.99). Figure (4.3) shows the original mesh, dynamic refined mesh of cells located at the interface, and details of the mesh refinement. It should be noted that turbulence in the single phase regions is simulated using LES model. However, none of the terms arising from filtering the interface (e.g. subfilter volume fraction transport or subfilter surface tension) are modeled. Instead, the interface is directly resolved and there is no special LES treatment for the interface [41, 151]. In this study, the running time for the numerical cases is 6 ms, and the numerical data is saved every 0.04 ms. The maximum Courant number in this study is 0.15.

Table 4.1 Values of $U_{x,a}$, $U_{x,u}$, $U_{x,avg}$, U_R , We , and q for various cases

Case No.	$U_{x,a}$ (ms ⁻¹)	$U_{x,u}$ (ms ⁻¹)	$U_{x,avg}$ (ms ⁻¹)	$U_R = U_{x,a}/U_{x,u}$	We	q
1	52.3	104.7	78.5	0.5	50	5
2	78.5	78.5	78.5	1	50	5
3	104.7	52.3	78.5	2	50	5
4	52.3	104.7	78.5	0.5	50	20
5	78.5	78.5	78.5	1	50	20
6	104.7	52.3	78.5	2	50	20
7	36.9	184.5	110	0.2	100	5
8	73.8	147.6	110	0.5	100	5
9	110	110	110	1	100	5
10	147.6	73.8	110	2	100	5
11	184.5	36.9	110	5	100	5
12	36.9	184.5	110	0.2	100	20
13	73.8	147.6	110	0.5	100	20
14	110	110	110	1	100	20
15	147.6	73.8	110	2	100	20
16	184.5	36.9	110	5	100	20

Figures (4.4-4.6) show the prediction of liquid breakup, the surface wavelength (λ_s), and the column breakup point location (x_b) at different refinement levels (i.e. without refinement, with two refinement levels, and with three refinement levels). The mentioned parameters are defined clearly in the results section of this paper. However, the main goal of these figures is to present

some numerical convergence tests with respect to grid size. In these figures, time, U_R , We , and q are equal to 6 ms, 1, 100, and 20, respectively. As shown in Figure (4.4), by increasing the number of refinement levels (i.e. reducing the size of the cells located at the interface), the overall behavior of breakup and the structure of ligaments and droplets are captured more accurately. Figures (4.5) and (4.6) show that the predicted λ_s and x_b in the current work using three refinement levels are in excellent agreement with the results of Xiao *et al.* [153] (the number of cells in their study is around 20 million) and are within the experimental data domain. The computational time for the mentioned case ($U_R=1$, $We=100$, and $q=20$) at different refinement levels is also presented in Figure (4.7). The simulations are performed using 64 processors on the supercomputer of CalculQuebec. It is clearly demonstrated that, by increasing the number of refinement levels, the computational time increases significantly. Four levels of refinement has not been applied here, the reason is that it is time consuming and three levels of refinement can provide a good agreement between numerical and experimental results.

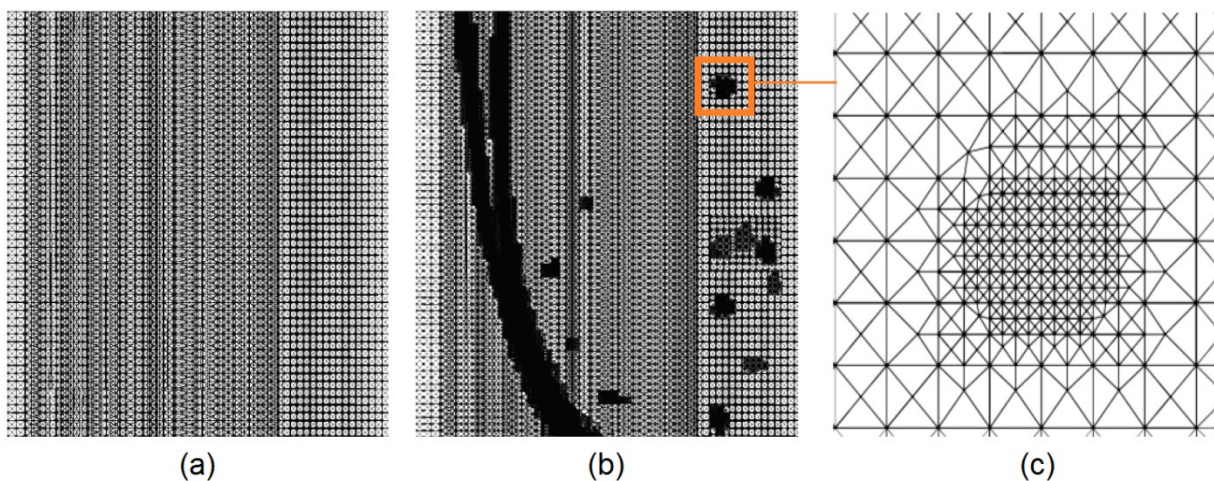


Figure 4.3 Dynamic adaptive mesh refinement method; (a) the original mesh, (b) dynamic refined mesh of cells with α between 0.01 and 0.99, and (c) mesh refinement close-up

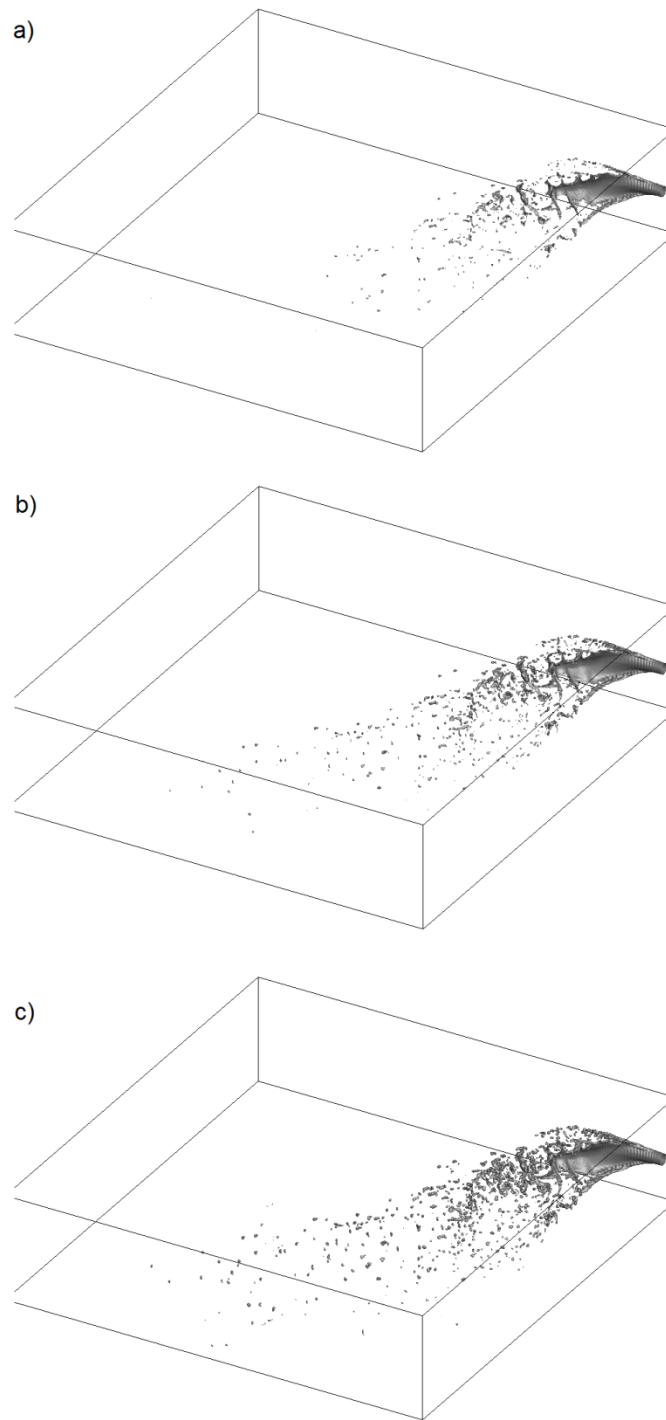


Figure 4.4 Prediction of liquid breakup and structure of ligaments and droplets (time=6 ms, $U_R=1$, $We=100$, and $q=20$) as a function of refinement levels; a) without refinement, b) with two refinement levels, c) with three refinement levels

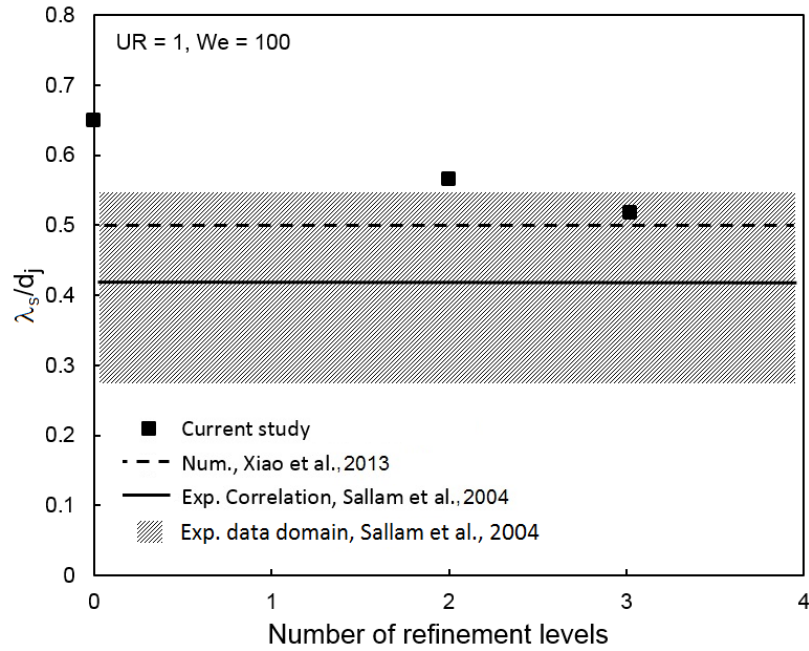


Figure 4.5 Prediction of surface wavelength as a function of refinement levels (time=6 ms, $U_R=1$, $We=100$, and $q=20$)

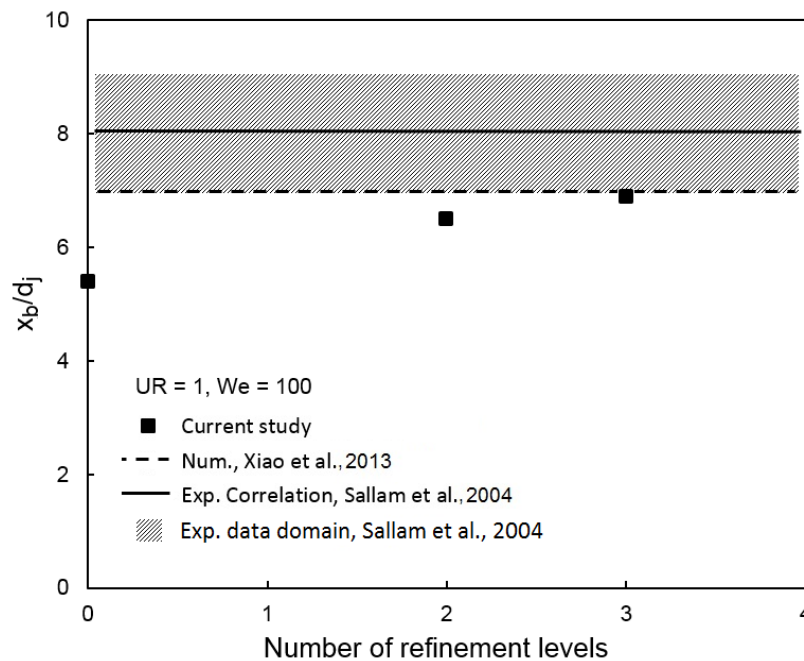


Figure 4.6 Prediction of column breakup point location as a function of refinement levels (time=6 ms, $U_R=1$, $We=100$, and $q=20$)

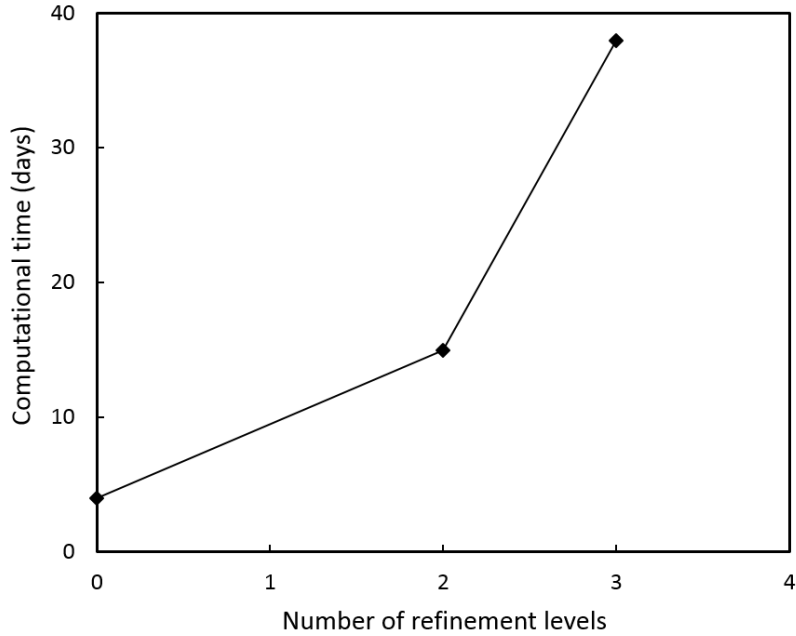


Figure 4.7 Computational time as a function of refinement levels ($U_R=1$, $We=100$, and $q=20$)

4.3 Results and Discussions

In Figures (4.8) and (4.9), the isosurface of $\phi = 0$ is presented to show the water structures at different We , q and U_R (time is equal to 6 ms). Noting that $U_R < 1$ means $U_{x,a} < U_{x,u}$ (U_x decreases with increase of y for $U_R < 1$) and vice-versa. In addition, $U_R = 1$ shows a uniform crossflow. In the current work, similar to other studies [40, 47, 142, 148, 149, 153], the jet penetration is defined as the lower periphery of the water jet. Clearly, as U_R increases, jet penetration increases. For $U_R < 1$, the crossflow velocity near the water jet nozzle is high, therefore, the local q is low and the jet trajectory changes rapidly. Consequently, the jet penetration is low. On the other hand, for $U_R > 1$, the jet penetration is high because the gas velocity and local q near the jet nozzle are low and high, respectively. Figures (4.8) and (4.9) show that as the jet penetration increases, the height of the spray core and the spray coverage area increase. Spray core is known as a small region near the spray plume center where the volume flux is high. In this

region, a large number of slow moving big droplets/ligaments exist. This region is surrounded by relatively small droplets [47].

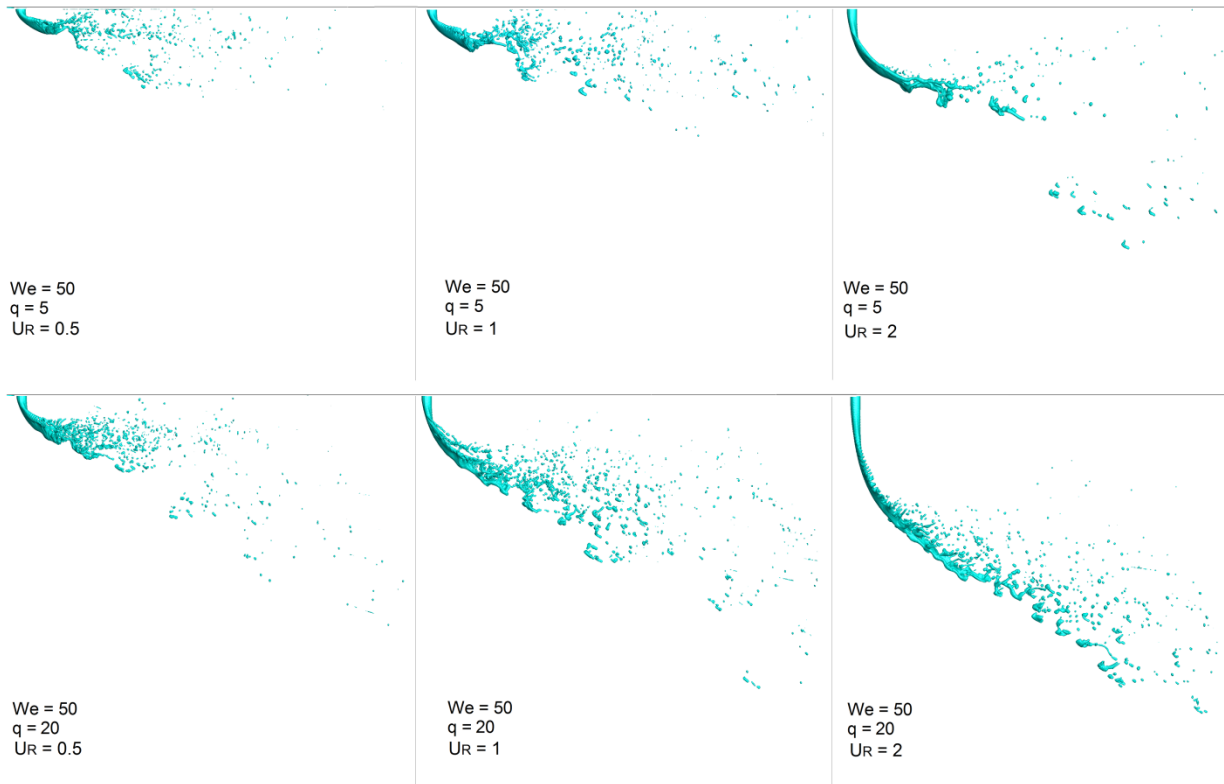


Figure 4.8 Predicted liquid structure for $We=50$, and different q and U_R

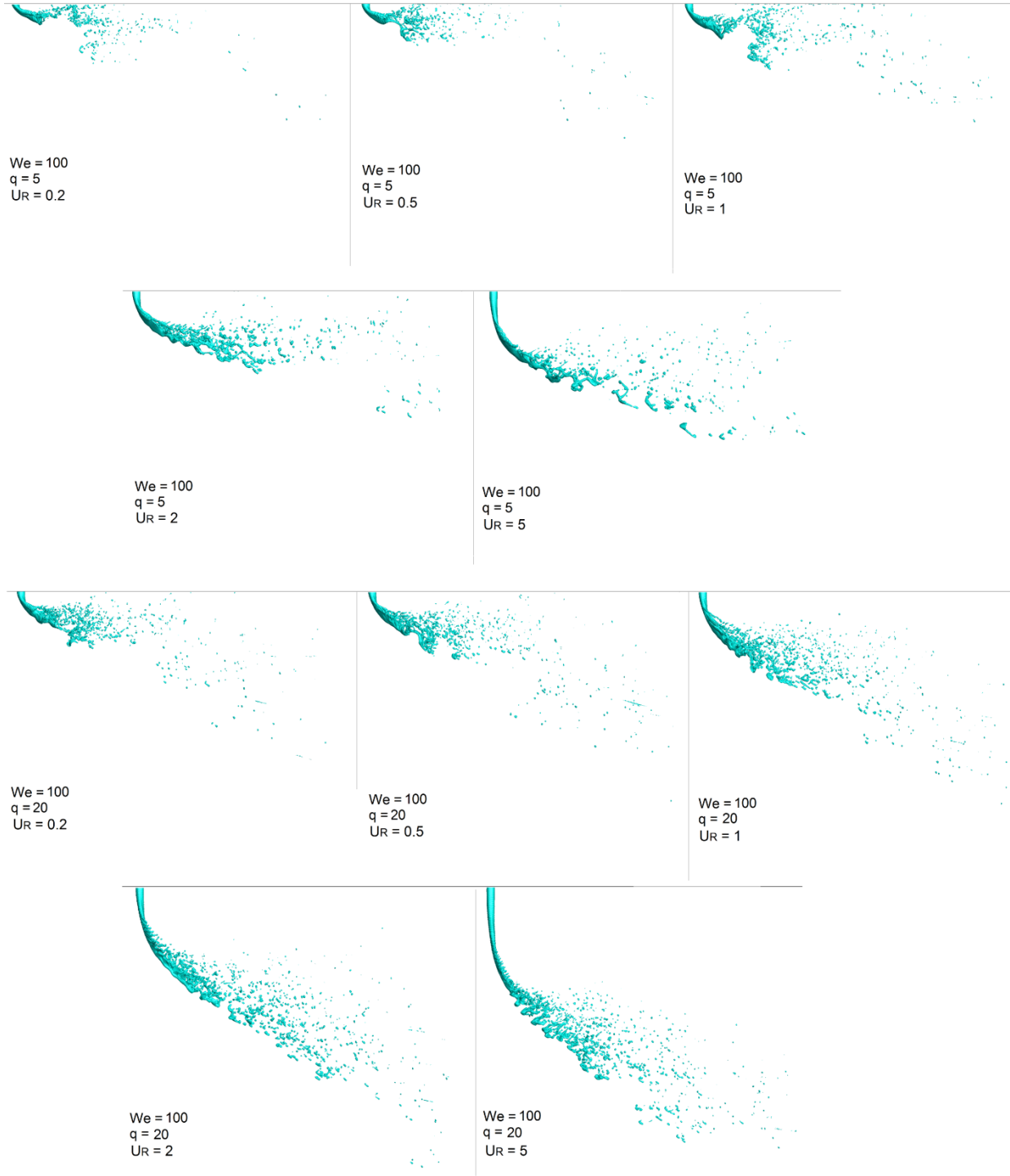


Figure 4.9 Predicted liquid structure for $We=100$, and different q and U_R

Figure (4.8) shows that when Weber number is 50, q is 5, and U_R is 1, the liquid breakup regime is multimode as was also detected by Sallam *et al.* [46]. In addition to thin bags formation, liquid sheets ejection from the liquid column surface is observed. However, the thin liquid bags cannot be fully captured due to the limitations of mesh resolution. As U_R reduces, although the local Weber number increases, the liquid column deflection increases (i.e. the liquid penetration decreases) which causes the liquid sheets formation to not change significantly compared to the case of $U_R = 1$. Noting that the thin liquid bags are still distinguishable and their size seems to decrease. As U_R increases, the local Weber number decreases and the liquid bags fragmentation is more recognizable. Furthermore, Figure (4.8) shows that as q increases, the liquid sheets ejected from the liquid column surface are observed more, due to the increase of penetration height. By increase of the Weber number from 50 to 100 (see Figure (4.9)), the same scenario that was explained above occurs, however this time the liquid sheets formation is observed more frequently.

Figure (4.10) shows the jet surfaces and the wave structures on the surfaces from the incoming air direction for different We , q , and U_R (time is equal to 6 ms). In Figure (4.11), the wave structures on the jet surfaces for high U_R cases (i.e. $U_R = 2$ and 5) from two directions are revealed. As clearly shown, different local flow conditions cause the surface wavelength along the jet to vary spatially. Figure (4.11) shows that for high U_R cases such as $U_R = 2$, the surface wavelength increases along the jet due to different local flow strength and increase of air velocity. It is also clear that as U_R increases, the surface wavelength increases as well. In addition, the variation of the surface wavelength along the jet becomes more significant as U_R increases.

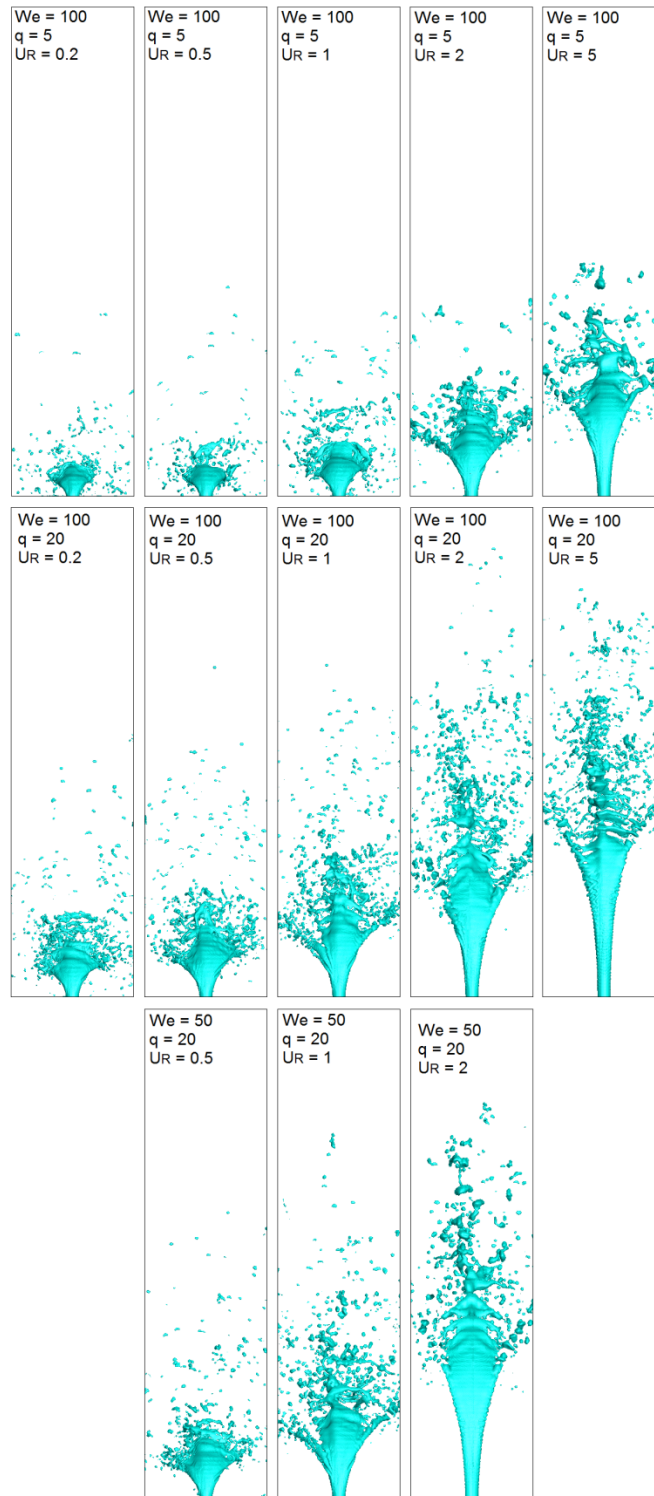


Figure 4.10 Predicted liquid structure for different We , q , and U_R ; view from the incoming air direction

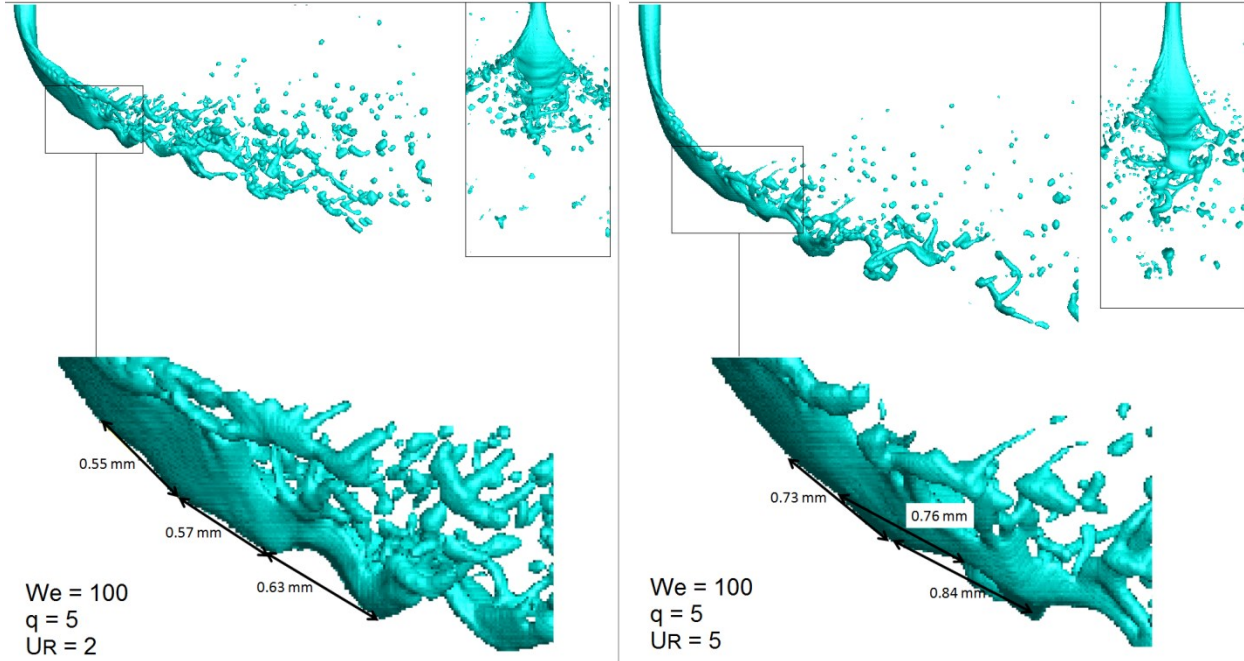


Figure 4.11 Surface wave structures and wavelengths for high U_R cases; top right corner: view from the incoming air direction

A comparison between the results of this work and the experimental data [47] in terms of liquid penetration height is presented in Figure (4.12). In the experimental work of Tambe [47], 200 image pairs were captured for each case. The raw images then were averaged, and the jet penetration was obtained from the averaged image. In this study, to extract the jet penetration trajectory from the numerical results, the 3D liquid structure was first converted into 2D images. Every 0.04 ms, the coordinates of the cells (x_i, y_i, z_i) containing liquid ($\phi \geq 0$) are saved. Then their coordinate in the z direction is set to zero. Subsequently, the cells coordinates are sorted ascendingly in the x direction. Using the same concept as described in the experimental work of Tambe [47], an average of 150 images is taken and the jet trajectory is acquired from the averaged image. As shown in Figure (4.12), although there is a good agreement between the numerical and

experimental results, the numerical simulation underestimates the jet penetration especially for high q and U_R . The possible reasons are discussed in the following paragraphs.

From the experimental point of view, as mentioned by Lubarsky *et al.* [163], the liquid penetration trajectories obtained from various experimental studies, significantly differ from each other. One of the main reasons that causes this significant discrepancy is the injector design and its location in the crossflow. It is shown that the liquid turbulence inside the injector (the internal turbulence can be created by the sharp edge of the orifice entrance) noticeably alters the liquid jet structure in the crossflow, Sauter Mean Diameter (SMD), location of the column breakup point (CBP), and the spray penetration trajectory. For instance, Lubarsky *et al.* [163] revealed that changing the orifice entrance from a sharp edge to a round one, causes the spray penetration to increase by 12%. In addition, the numerical simulation performed by Xiao *et al.* [153] indicated that assuming the laminar boundary condition for the liquid phase at the nozzle exit (at the circular hole) results in underestimation of the jet penetration. They showed that taking account of the turbulent boundary condition, causes the results of the experimental and numerical studies to be matched perfectly [153]. In other words, variations of the inlet liquid profile might be the main reason of the experiment-simulation discrepancies in liquid penetrations. As discussed by Li and Soteriou [155], the shape of inlet liquid profile affects the downward liquid momentum. As mentioned earlier in the present work, a uniform velocity profile is used in the simulations whereas a turbulent inlet profile existed in the experiment. Under the same flow rate, the experimental inlet provides higher liquid momentum and causes higher liquid penetration [155].

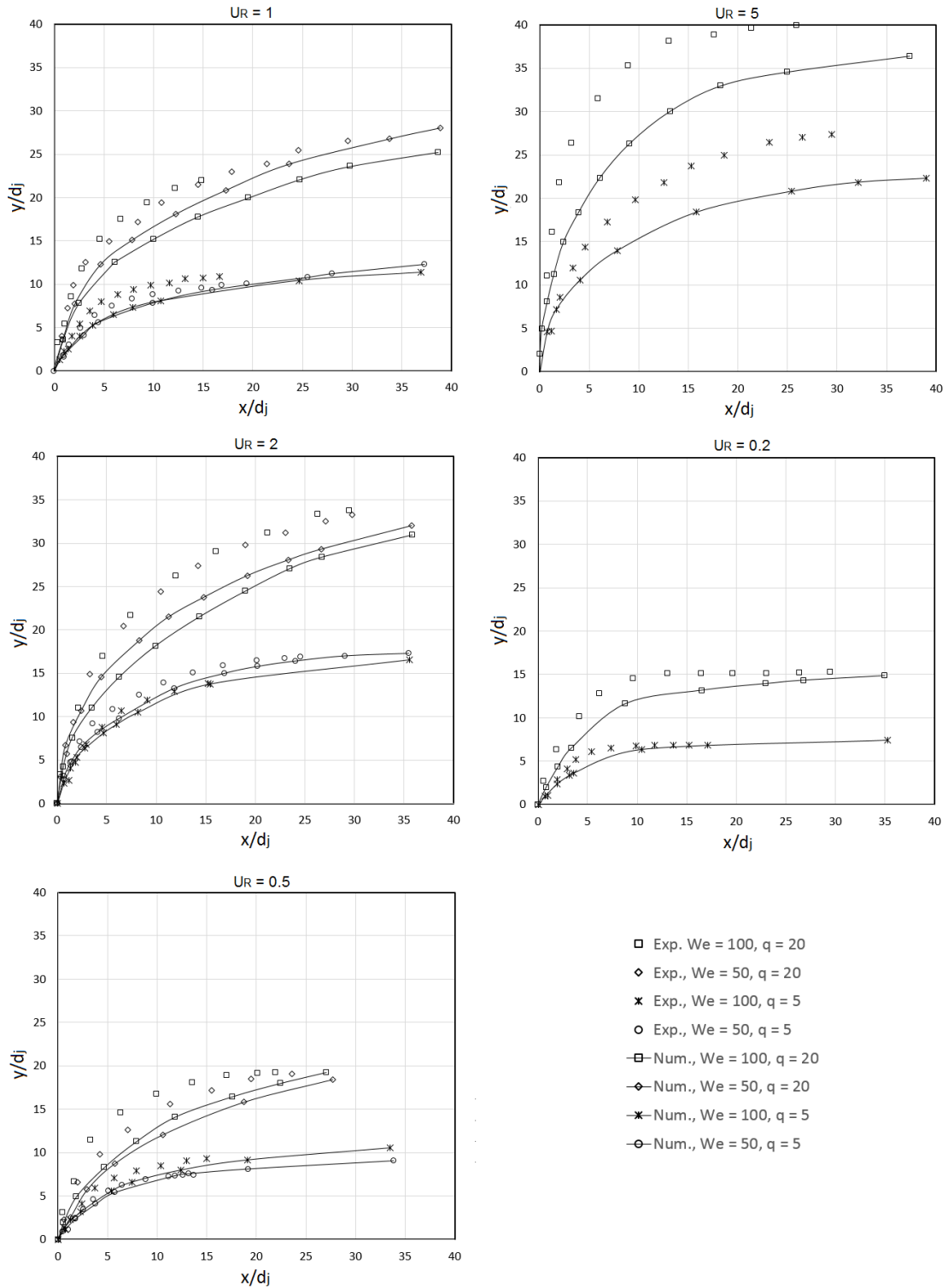


Figure 4.12 Comparison of predicted liquid penetration height with the experimental observations [47]

The crossflow turbulence and wall boundary layer also have influences on the jet penetration. In the experimental work of Tambe [47], at the location of water injection, the crossflow velocity profiles revealed that the boundary layer thickness on both top and bottom walls could reach 3 mm. However, in this study, the wall boundary layer at the location of liquid injection is much less (at most 0.1 mm), which is consistent with the Blasius solution for laminar flow over a flat plate. It is obvious that as the wall boundary layer increases, the liquid jet penetration increases and the numerical results will be in a better agreement with the experiments.

In the experimental work of Tambe [47], the gas velocity profiles were quasi-linear, and linear regression was used to approximate them. Near the test chamber center, the real velocity was lower than what was linearized and approximated. On the other hand, near the upper and lower walls, the actual velocity was higher than the approximated one. As the difference between $U_{x,b}$ and $U_{x,u}$ increased (i.e. U_R decreases if $U_R < 1$ or increases if $U_R > 1$), the deviation from the linear assumption was more obvious. This estimation can be another reason for the above mentioned discrepancy.

Figure (4.12) also illustrates that as U_R increases, the penetration height increases significantly. By increasing U_R from 0.2 to 5, the jet penetration increases over 140%. It is also revealed that jet penetration increases with q as expected. Furthermore, the effect of We on the jet penetration is presented in Figure (4.12). As can be seen, a change in We has marginal effects on the jet penetration. As discussed by Lubarsky *et al.* [163], by increasing the Weber number, the average size of the droplets reduces. Since smaller droplets accelerate faster in the crossflow direction, the liquid jet penetration decreases.

The investigation of liquid penetration height and trajectory shape are the main objectives of this study. Most of the spray trajectory correlations available in the literature pose the transverse

penetration (y/d_j) as a function of the momentum flux ratio (q) and the streamwise distance (x/d_j). However, there exist a few studies, dedicated to the effect of Weber number on penetration. A logarithmic function or an exponential function for x have been proposed. As discussed by Tambe [47], in general, the function templates used for spray trajectories are as follows

$$\frac{y}{d_j} = c \left(\frac{x}{d_j} \right)^m q^n \quad \text{Equation 4.23}$$

$$\frac{y}{d_j} = c \left(\frac{x}{d_j} \right)^m q^n We^f \quad \text{Equation 4.24}$$

$$\frac{y}{d_j} = cq^n \ln \left(1 + m \frac{x}{d_j} \right) \quad \text{Equation 4.25}$$

where the parameters c , m , n , and f are unknown constants and are obtained by fitting processes.

Tambe [47] used the jet trajectories of all measured cases and fit two empirical correlations to predict liquid penetration in shear-laden crossflow

$$\frac{y}{d_j} = 2.17q^{0.43} \ln \left(1 + 2 \frac{x}{d_j} \right) \quad \text{Equation 4.26}$$

$$\frac{y}{d_j} = 0.52 \left(\frac{x}{d_j} \right)^{0.34} q^{0.34} We^{0.42} \quad \text{Equation 4.27}$$

However, it was explained that none of the above correlations are applicable due to wide range of data and high standard deviation. In this work, instead of using the jet trajectories of all measured cases and fitting a specific curve, another approach is employed. For each U_R (e.g. $U_R = 2$), the jet trajectories data are put in a log-log diagram shown in Figures (4.13). Then, the algorithms available in MATLAB are used to find the best fit (the maximum standard deviation is 0.043). As can be seen in Figures (4.13), changing U_R causes the trajectory curve to shift and the line slope to vary slightly. This phenomenon suggests that the parameters c , m , n , and f , are not constants and should be dependent on U_R . The following function template is used here since the effect of We on the spray trajectory is negligible

$$\frac{y}{d_j} = f(U_R) \left(\frac{x}{d_j}\right)^{g(U_R)} q^{h(U_R)} \quad \text{Equation 4.28}$$

For the experimental data [47], the best fits are as follows

$$f(U_R) = 10^{(0.0083U_R^3 - 0.081U_R^2 + 0.3U_R - 0.11)} \quad \text{Equation 4.29}$$

$$g(U_R) = 0.0051U_R + 0.49 \quad \text{Equation 4.30}$$

$$h(U_R) = -0.0051U_R + 0.51 \quad \text{Equation 4.31}$$

or

$$\left(\frac{y}{d_j q}\right) = 10^{(0.0083U_R^3 - 0.081U_R^2 + 0.3U_R - 0.11)} \left(\frac{x}{d_j q}\right)^{(0.0051U_R + 0.49)} \quad \text{Equation 4.32}$$

It is clear that for U_R between 0.2 and 5, $0.0051U_R + 0.49 \cong 0.5$. Therefore, the above correlation can be simplified as

$$\frac{y}{d_j} = 10^{(0.0083U_R^3 - 0.081U_R^2 + 0.3U_R - 0.11)} \left(\frac{xq}{d_j}\right)^{0.5} \quad \text{Equation 4.33}$$

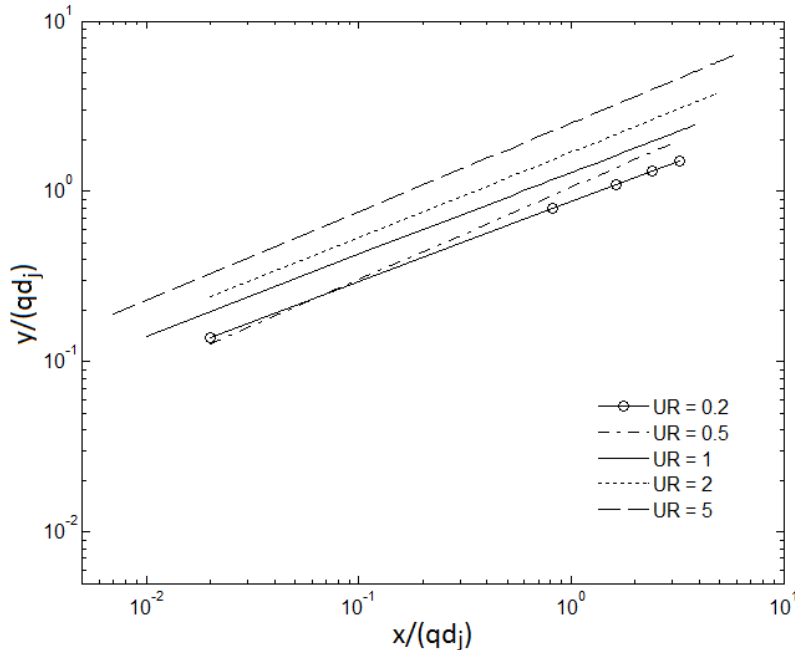


Figure 4.13 Liquid penetration heights obtained from experimental data [47]

Interestingly, this correlation is well matched with the theoretical results of Wu *et al.* [149]. They showed that for liquid jet in uniform crossflow, $y/d_j = c(xq/d_j)^{0.5}$, and found that $c = 1.37$ predicts the best fit with their experimental data. It can be concluded that for nonuniform crossflow, we have the same correlation, $y/d_j = c(xq/d_j)^{0.5}$, although c is no longer constant and depends on the crossflow velocity profile. For uniform crossflow (i.e. $U_R = 1$), our correlation changes to $y/d_j = 1.31(xq/d_j)^{0.5}$ which is in a good agreement with the result of Wu *et al.* [149]. The maximum standard deviation for Equation (4.33) is 0.063.

The breakup of round nonturbulent liquid jets in uniform crossflow was experimentally investigated by Mazallon *et al.* [44] and Sallam *et al.* [46]. In the experiments of Sallam *et al.* [46], the boundary layer thickness near the nozzle exit was around 0.5 mm which was smaller than 10% of the distance along the liquid jet for all measurement conditions in their work. Therefore, the effect of wall boundary layer on the experimental results were trivial. As mentioned above, in this work, the wall boundary layer thickness near the nozzle exit is at most 0.1 mm. Accordingly, the numerical results obtained from this study are compared and validated with the experimental data from the work of Sallam *et al.* [46]. In addition, as mentioned above, Li and Soteriou [152] and Xiao *et al.* [153] numerically studied the behavior of round nonturbulent liquid jets in uniform crossflow using coupled level set and volume of fluid method. Consequently, the results of the current work are compared with the results presented in their studies [152, 153].

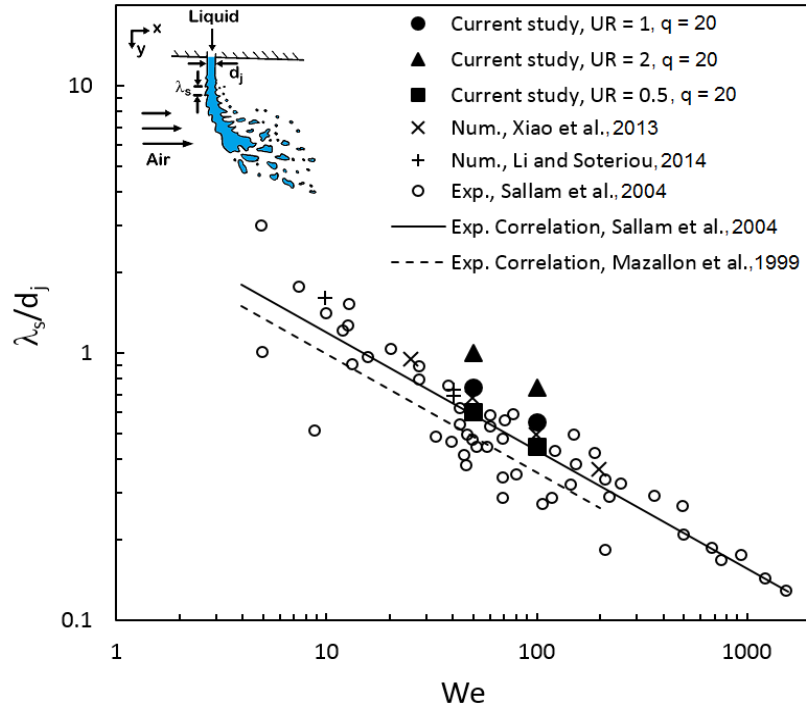


Figure 4.14 Comparison of the predicted liquid surface wavelength in the current study with the experimental [44, 46] and numerical [152, 153] results for the uniform crossflow; the effects of We and U_R on liquid surface wavelength

Mazallon *et al.* [44] and Sallam *et al.* [46] measured the wavelength of liquid surface disturbances/waves during the primary breakup process. As shown in Figure (4.14), the wavelength (λ_s) of these disturbances was defined as the vertical distance between the peaks for the liquid column breakup. Due to better observation, the wavelength was measured on the upstream side of the liquid jet. It is clear from Figure (4.14) that as Weber number increases, the parameter λ_s/d_j decreases. In addition, for $U_R = 1$ (uniform crossflow), there is a good agreement between the results of the current study and the existing numerical and experimental data in the literature [44, 46, 152, 153]. The reduction of U_R causes the parameter λ_s/d_j to decrease and vice versa (noting that the local We near the nozzle exit increases as U_R decreases). Furthermore, Figure

(4.15) illustrates the effect of q on λ_s/d_j at a constant We . In addition to the numerical results of Xiao *et al.* [153], the experimental data domain near $We = 100$ along with the empirical correlation for liquid jet in uniform crossflow [46] are shown in this figure. As can be seen, the increase in q results in the increase of λ_s due to the effects of local flow changes.

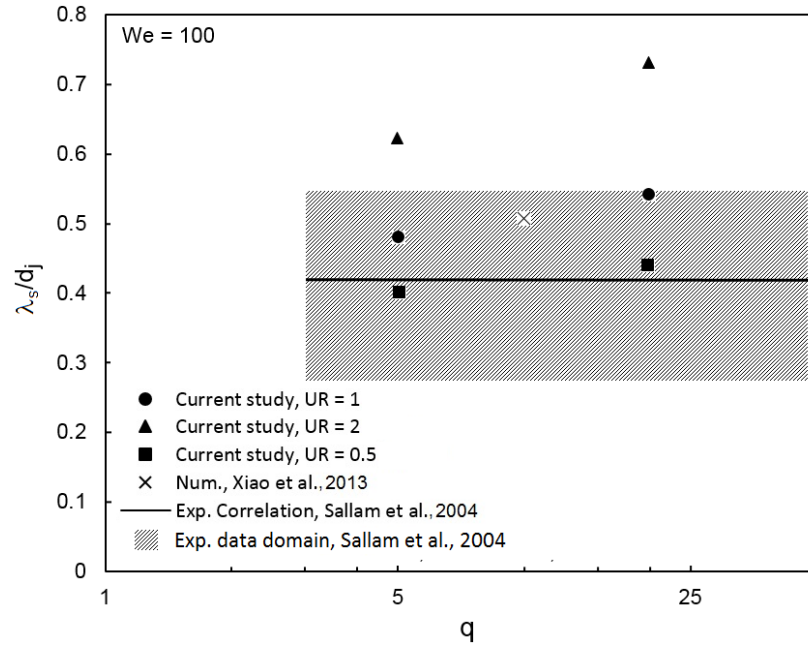


Figure 4.15 Comparison of the predicted liquid surface wavelength in this study with the experimental [46] and numerical [153] results for the uniform crossflow; the effects of q and U_R on liquid surface wavelength

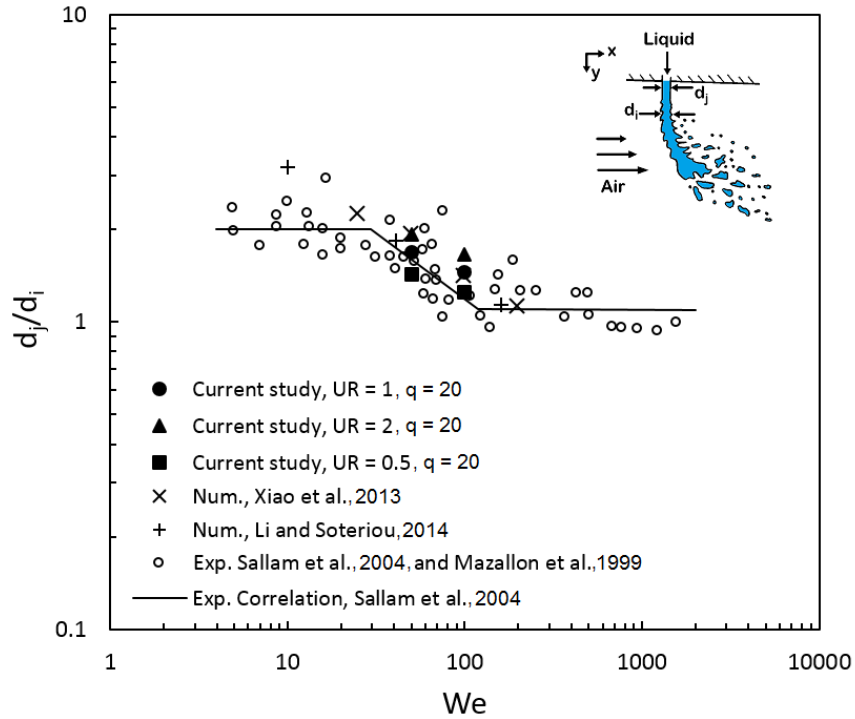


Figure 4.16 Comparison of the predicted liquid jet dimension at onset of breakup with the experimental [44, 46] and numerical [152, 153] results for the uniform crossflow; the effects of We and U_R on d_i

It is shown both experimentally and numerically that the liquid column deformation is relatively universal at the onset of breakup for the round nonturbulent liquid jets in uniform crossflow [44, 46, 153]. Before the onset of breakup, the liquid cross sectional area is preserved, so that the dimensions of the cross stream and streamwise of the liquid jet increases and decreases, respectively. Therefore, as shown in Figure (4.16), Sallam *et al.* [46] and Mazallon *et al.* [44] simplified the liquid deformation measurements to merely consider the streamwise dimension of the liquid jet at the onset of breakup. In Figure (4.16), d_i stands for the liquid jet dimension in the crossflow direction (i.e. streamwise) at the onset of droplet formation. As shown in this figure, for uniform crossflow, the numerical results of the current study are consistent with the experimental

observations and the numerical values reported in [44, 46, 152, 153]. As U_R decreases, the local Weber number near the nozzle exit increases. Therefore, the breakup begins earlier prior to significant deformation of the liquid column (i.e. by decreasing U_R , d_i increases). Moreover, Figure (4.17) shows the effect of q on d_i . Similar to Figure (4.15), Weber number is equal to 100. In addition, the experimental data domain and the numerical results of Xiao *et al.* [153] are presented in this figure. As shown, changing q from 5 to 20 results in slight increase of d_i .

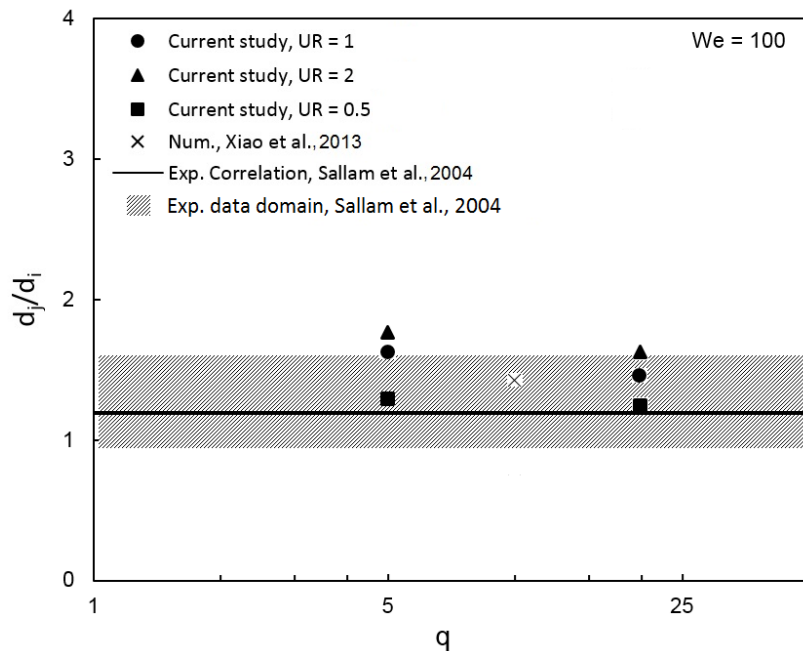


Figure 4.17 Comparison of the predicted liquid jet dimension at onset of breakup with the experimental [46] and numerical [153] results for the uniform crossflow; the effects of q and U_R on d_i

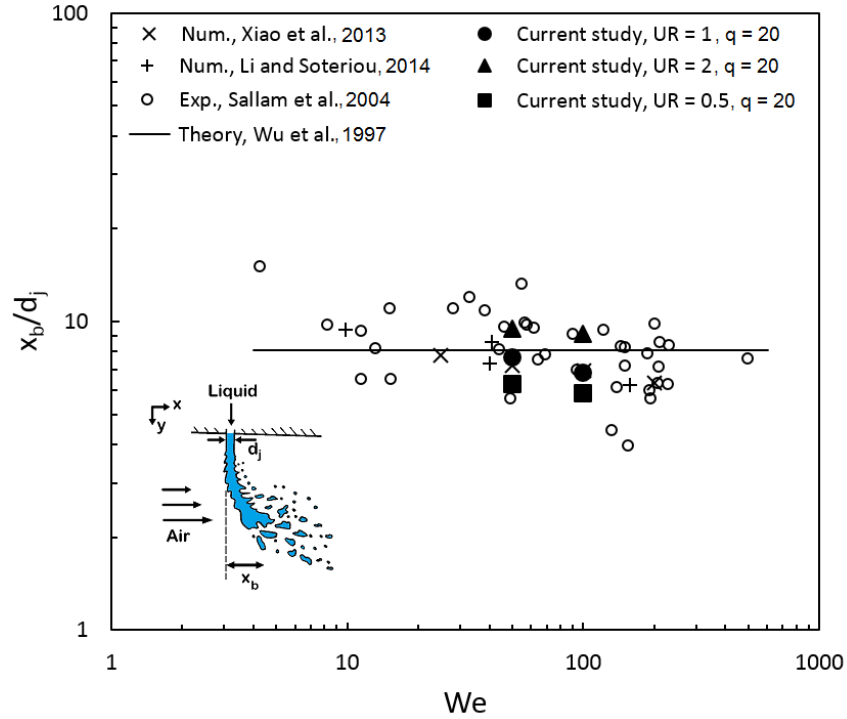


Figure 4.18 Comparison of the liquid column breakup point location (in crossflow direction) predicted in the current study with the experimental [46], theoretical [149] and numerical [152, 153] results for the uniform crossflow; the effects of We and U_R on x_b

The location of the column breakup point (CBP), is another parameter that characterizes the liquid jet primary breakup in the crossflow. At CBP, the liquid column ceases to exist and disintegrates into ligaments and droplets. Figures (4.18-4.20) show the comparison between the results of this study and the experimental, theoretical, and numerical data from the literature [46, 149, 152, 153] in terms of CBP location (x_b, y_b). In this article, for different U_R, q , and We , the CBP location is found for the 25 last saved data. Then, the average of this 25 numbers is shown in Figures (4.18-4.20). The numerical results presented in this work for the uniform crossflow are in a good agreement with the experimental, numerical, and theoretical results in the literature [46, 149, 152, 153]. Similar to the numerical results described in the literature [152, 153], the

simulations of this work reveals that x_b decreases slightly with increase of We (see Figure (4.18)). In addition, x_b decreases with U_R since the local We near the nozzle exit increases. Figure (4.19) reveals the effects of q on x_b when We is equal to 100. As shown, increasing q causes x_b to increase slightly. Figure (4.20) shows that as q increases, y_b increases considerably due to increase of the penetration height. Our simulations show that for non-uniform crossflow, as U_R decreases, since the penetration height decreases, y_b reduces significantly.

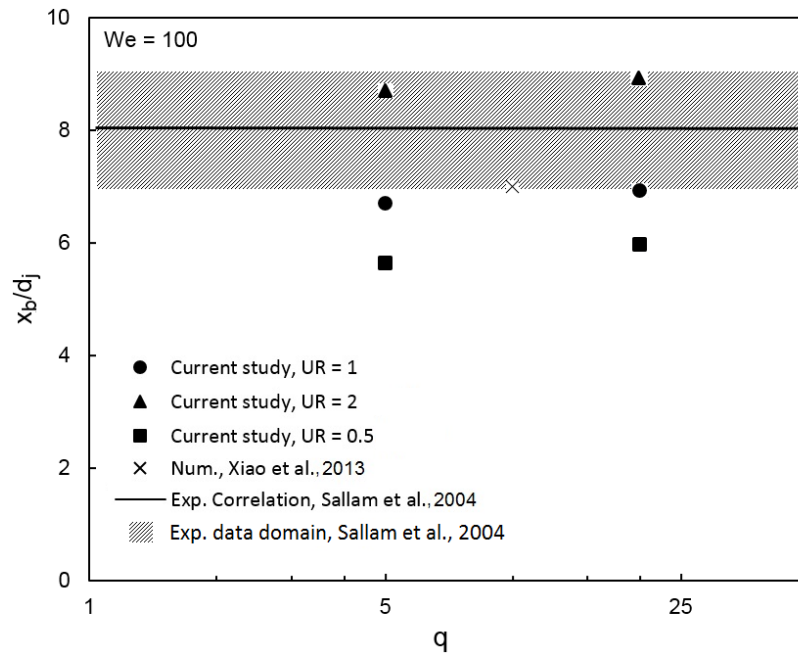


Figure 4.19 Comparison of the liquid column breakup point location (in crossflow direction) predicted in this study with the experimental [46] and numerical [153] results for the uniform crossflow; the effects of q and U_R on x_b

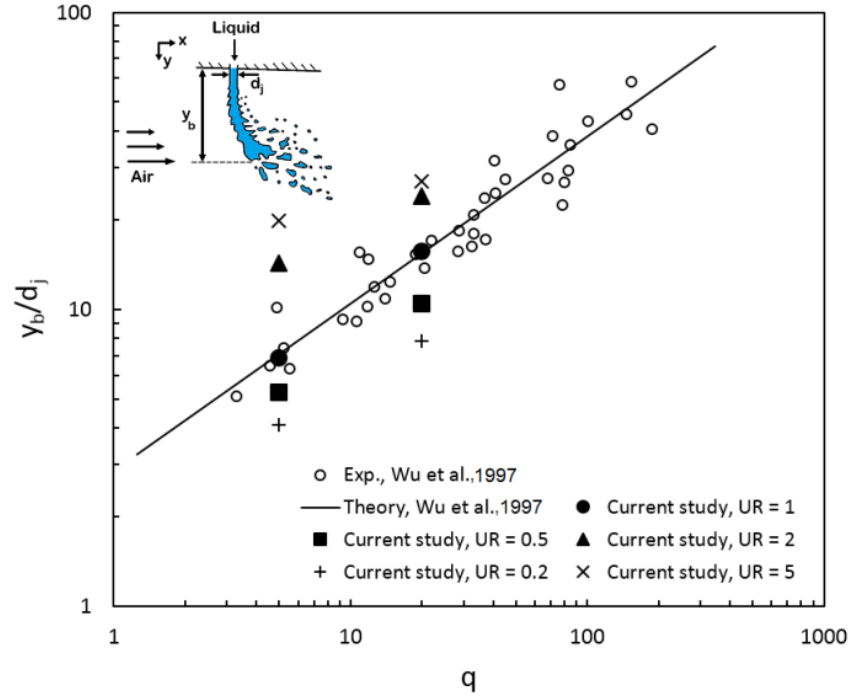


Figure 4.20 Comparison of the liquid column breakup point location (in direction of the liquid injection) predicted in the current study with the experimental, and theoretical results [149] for the uniform crossflow

4.4 Summary and Conclusions

Study of liquid jets in nonuniform crossflow is of utmost importance due to their various industrial applications such as in fuel injection in gas turbines, and solution/suspension injection in thermal spray torches. Hence, in this paper, the primary breakup of the round nonturbulent liquid jets in shear-laden gaseous crossflow is studied numerically using a simple coupled level set and volume of fluid (S-CLSVOF) method together with the large eddy simulation (LES) turbulence model. The ratio of the crossflow velocities at the bottom and top of the inlet boundary (U_R) is defined as a parameter to display the slope of the velocity profiles. The gas Weber number (We) and liquid to gas momentum flux ratio (q) are defined based on the average crossflow velocity.

The comparison between the numerical results obtained in this paper and the available experimental and numerical data in the literature indicate that the mentioned SCLSVOF-LES methodology enables accurate prediction of the near field behavior of the liquid jet in crossflow. The results indicate that as U_R or q increases, the liquid jet penetration increases significantly. On the other hand, as We increases, the jet penetration decreases slightly. General correlation for liquid penetration height is developed based on the experimental data [47]. It was shown that, for different crossflow velocity profile, the dimensionless penetration height is proportional to $\sqrt{xq/d_j}$. In addition, it was found that different local flow condition results in spatial variation of surface wavelength along the jet. However, the wavelength of liquid surface disturbances reduces as U_R decreases. Finally, the numerical results reveal that the location of column breakup point in liquid injection direction reduces significantly as U_R decreases.

Chapter 5

Penetration and Breakup of Liquid Jet in Transverse Free Air Jet with Application in Suspension-Solution Thermal Sprays

“Reprinted from the paper published in journal of Materials and Design, 2016, volume 110, pp. 425-435, [164], with permission”

Abstract

The penetration and breakup of water jets in transverse free air jets are experimentally studied at room conditions. After coming out of an orifice and forming a cylindrical jet, water interacts with a free air jet and disintegrates. In the current work, the effects of the instabilities of cylindrical liquid jets, the distance between the liquid orifice and gas nozzle, and the ratio of liquid orifice diameter to the gas nozzle diameter, on the breakup mechanisms and liquid structure are investigated. Moreover, general correlations for spray trajectory and location of the liquid column breakup point are developed. Experimental results indicate that the breakup mechanisms are mainly controlled by the gaseous and liquid Weber numbers. Like other studies, four breakup regimes, namely capillary, bag, multimode, and shear breakup are observed. It is found that, due to the presence of instabilities on the cylindrical liquid jet, large ligaments are formed close to the interaction point of liquid and gas flows.

Furthermore, results indicate that the location of liquid column breakup point are mainly dependent on the momentum flux ratio, and perturbations on the liquid jet. This fundamental study is essential to investigate the spray structure of a suspension-solution jet in plasma spray.

5.1 Introduction

In thermal spray processes, molten, semi-molten or solid particles that are heated and accelerated by a high-temperature high-velocity jet/flame, are deposited on a substrate. The well-adhered and dense coating is formed by the impact and deformation of the so called particles on the substrate. Different types of coatings such as wear resistance, corrosion resistance, and thermal barrier are extensively generated for industrial applications using thermal spray techniques [1, 2, 165].

Coating with nano and submicron sized particles that has become center of attention recently, is the main trend in development of emerging thermal spray processes. The main reason is the superior performance of nanostructured and fine microstructured coatings such as noticeable superhydrophobicity behavior, remarkable wear resistance, enhanced catalytic behavior, improved thermal insulation and thermal shock resistance [7, 105-110, 139, 166-168]. Nevertheless, it is difficult to generate nanostructured coatings using conventional thermal spray techniques. One of the main reasons is the particle feed line clogging due to particles agglomerations [19, 35, 36, 101]. One way of addressing the mentioned issue is to inject a combination of fine solid particles and a base fluid such as water or alcohol (e.g. ethanol) into thermal spray torches directly. This technique is known as suspension thermal spray. Another common method is called solution precursor thermal spray. In this technique, solutions such as metal-organics (e.g. aluminum nitrate) are

injected into the torches. These solutions react inside the flame/jet and create very fine solid particles [8, 12, 19, 35, 36, 73, 101, 102, 169, 170].

Suspension/liquid is usually injected into the jet/flame radially [8, 12, 19, 35, 36, 73, 102, 169, 170]. Figure (5.1) illustrates the radial injection of suspension/liquid into a plasma plume. After suspension/liquid column disintegration and formation of ligaments and droplets, the liquid phase evaporation/reaction becomes dominant. Consequently, the solid particles or their agglomerations remain in the field [8, 73, 102, 169, 170]. It is clear that the suspension/liquid breakup process has significant effects on particle in-flight behavior and coatings quality [12, 19, 35, 36]. Hence, it is essential to understand the mechanisms that control the suspension/liquid jet breakups and the resulting distribution of the suspension/liquid droplets.

There are tremendous experimental and numerical studies on interaction of liquid jets with gaseous crossflow in literature [43, 142, 143, 148, 152, 153, 163, 171-174]. In general, liquid jet in crossflow can be divided into three main categories: 1) nonturbulent liquid jet injection into a uniform crossflow, 2) turbulent liquid jet injection into a uniform crossflow, and 3) liquid jet injection into a nonuniform crossflow (e.g. shear-laden, and swirling). Using pulsed shadowgraphy and holography, Mazallon *et al.* [44] and Sallam *et al.* [46] investigated the behavior of a nonturbulent liquid jet in a uniform crossflow. Based on the gaseous Weber number, four breakup regimes were observed: column, bag, multimode, and shear breakup. The behavior of turbulent liquid jet in uniform crossflow was studied by Lee *et al.* [42], using a liquid injector with a large length-to-diameter ratio. They argued that, at low Weber numbers, the bag and multimode breakup regimes are not observed for the turbulent liquid jet. Furthermore, it was revealed that the distance of liquid column breakup and the breakup time for the turbulent liquid jet are smaller than those for the nonturbulent liquid jet. Recently, Tambe *et al.* [47, 49, 50] studied the liquid injection into

a nonuniform crossflow where the gas velocity profile was quasi-linear. The crossflow was made by dividing the wind tunnel into two components and introducing two independent streams into the wind tunnel. They showed that the gas velocity profile has significant effects on liquid jet behavior, jet penetration depth, and the droplet size distribution. The main reason is the significant variation of the gaseous Weber number, and the jet-to-crossflow momentum flux ratio in the liquid injection direction due to gas flow velocity gradient [47, 49, 50].

It is clearly shown in Figure (5.1) that the suspension/liquid and gas materials, and the nozzles configurations involved in thermal spray processes are different from those used in typical experiments of liquid jet in crossflow. In suspension thermal spray, the liquid-to-gas density ratio is around 50000 and the thermophysical properties of suspension such as surface tension and viscosity are functions of time. However, in classic studies of liquid jet in crossflow, the density ratio is much lower and the liquid properties do not change significantly. It is also worth mentioning that, in typical studies of liquid jet in crossflow, experiments are performed in wind tunnels, or at the engine conditions, where the injector nozzle exit mounted flush in the test section wall. Noting that the main application of these studies is in propulsion systems including turbojet, ramjet, and scramjet engines [42-50, 142-145, 148, 149, 152, 153, 163, 171-174]. However, as it is demonstrated in Figure (5.1), in thermal spray processes, suspension/liquid usually comes out of a cylindrical nozzle and forms a continuous jet. Then suspension/liquid jet penetrates into a free gas jet. The diameters of liquid injector orifice and the gas nozzle exit are usually around 0.15 ± 0.05 and 7 ± 2 mm, respectively [12, 19, 35, 36]. It is clear that, when suspension/liquid jet interacts with the high speed gas flow, the cylindrical suspension/liquid jet perturbations and instabilities may have significant influences on breakup mechanisms, ligament formation and final droplet size distribution. The mentioned instabilities are originating from the liquid nozzle and interaction of

cylindrical liquid jet with the surrounding gas. In other words, in addition to liquid Weber and Ohnesorge numbers, the distance between the liquid injector and gas nozzle exit (i.e. the instabilities growth) may have noticeable effects on breakup mechanisms and liquid penetration height [19, 175-177]. Moreover, the gas flow velocity at the torch exit is non-uniform, oscillatory, and chaotic which makes the breakup mechanism even more complex [8, 12, 73, 102, 169, 170, 178-180]. Furthermore, the gas temperature outside the torch changes significantly in both axial and radial directions and is oscillatory. Therefore, the gas density changes considerably which affects the liquid breakup behavior [8, 12, 19, 35, 36, 73, 102, 169, 170].

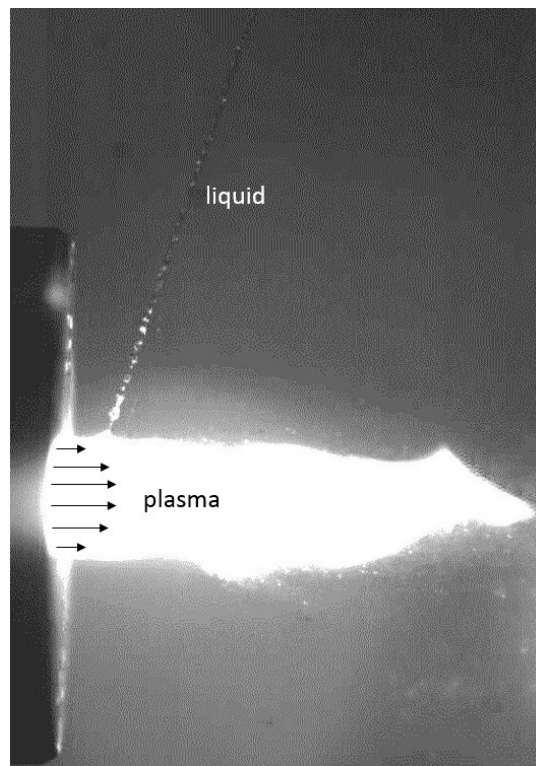


Figure 5.1 Liquid (water) radial injection into the plasma plume

As it is clarified in the above discussion, there are various parameters that affect the behavior and breakup mechanisms of liquid jets injected radially into the jets/flames in thermal spray

processes. However, since the main goal of thermal sprays is to generate dense coatings, based on the coatings quality, the optimum conditions for a few parameters have been experimentally and numerically achieved. For instance, it is known that the axial distance (i.e. in the direction of the gas flow) between the torch exit and the location of liquid-gas interaction should be around 1-3 mm [19]. Furthermore, the distance between the liquid injector and the location of liquid-gas interaction should be less than the breakup length of a cylindrical liquid jet. In this case, the continuous liquid jet, not droplets, penetrates into the gas crossflow. In addition, it is numerically shown that a dense coating is produced when most of the droplets, generated from liquid breakup, move near the gas nozzle centerline [19, 35, 36]. Apparently, to control the spray trajectory and droplet size distribution, more detailed qualitative observations together with quantitative data are needed.

With respect to the operating conditions explained above, atomization of liquid jets in transverse plasma flow is investigated in more details in a few experimental and numerical works [38, 39, 74, 178-184]. It should be mentioned that, although these studies have resulted in great observations, the fundamental physics of liquid breakup in the plasma crossflow has not been fully understood and described yet. For example, Figure (5.2) shows the instantaneous images of water jets in plasma crossflows [179]. As shown, there are large ligaments very close to the interaction point of water jet and plasma flow. Then these large ligaments break up and form much smaller droplets. The presence of these ligaments are very important since they control the droplet size distribution, and spray/droplets trajectories and evaporations. Therefore, the study of breakup physics is essential to find out why this type of liquid structure exist in the process and how it can be controlled. In general, six nondimensional numbers namely gaseous Weber number, momentum flux ratio (or liquid Weber number), gas flow Reynolds number, liquid Reynolds number, liquid-

to-gas density ratio, and the ratio of liquid orifice diameter to the gas nozzle diameter, are defined to explain the behavior of liquid jets in crossflow [1, 41, 45, 141, 150, 151, 185-197]. However, in addition to the above nondimensional numbers, the liquid turbulence, gas turbulence and nonuniformity, and injection angle are important parameters and have significant influences on the results [41, 42, 49, 50, 141, 163, 194-197]. As stated above, the suspension-solution plasma spray process is very complex and the mentioned liquid structure can be due to many reasons such as liquid column instabilities and perturbations, gas flow nonuniformity and oscillations, high liquid-to-gas density ratio, or all the mentioned parameters together. It should be also noted that doing experimental studies in plasma condition is challenging and the uncertainty of the results is too large.

To understand the breakup physics of liquid jet in plasma crossflow and to control the process, the effect of each mentioned parameter (i.e. nondimensional numbers, turbulence, and angle effects) on the liquid behavior should be investigated fundamentally. Therefore, controlling the process, which is challenging today, would be knowledge-based and easier. This approach is also used by the researchers in the field of propulsion [41-50, 141, 148-153, 163, 192-197]. For example, the effect of gas flow nonuniformity on the nonturbulent liquid jet behavior in crossflow is studied fundamentally by Jadidi *et al.* [141]. They showed that the gas flow nonuniformity significantly affect the spray penetration height and does not have considerable influence on the axial position of liquid column breakup point [141]. In this study, the main focus is on understanding the effects of liquid column instabilities and perturbation, the ratio of gas nozzle diameter to liquid orifice diameter, and the distance between liquid and gas nozzles, on the spray structure. Therefore, the experiments are done at room conditions without any gas flow fluctuations. Additionally, the non-dimensional numbers are used to study the mechanisms of

primary breakup and liquid fragmentation fundamentally, and to develop general correlations for spray penetration, and liquid column breakup point (CBP). Using the non-dimensional numbers, the results of this study can be linked to the suspension-solution plasma spray conditions. The CBP and spray penetration height are two main parameters that characterize the liquid jet disintegration in the crossflow [42-47, 49, 50, 148, 149, 163]. These are also key parameters for controlling the droplets trajectories, evaporation rates, and consequently coatings quality [12, 19, 35, 36, 38, 39, 74, 178-183]. The effect of other parameters such as injection angle and density ratio on the spray structure are considered as future works.

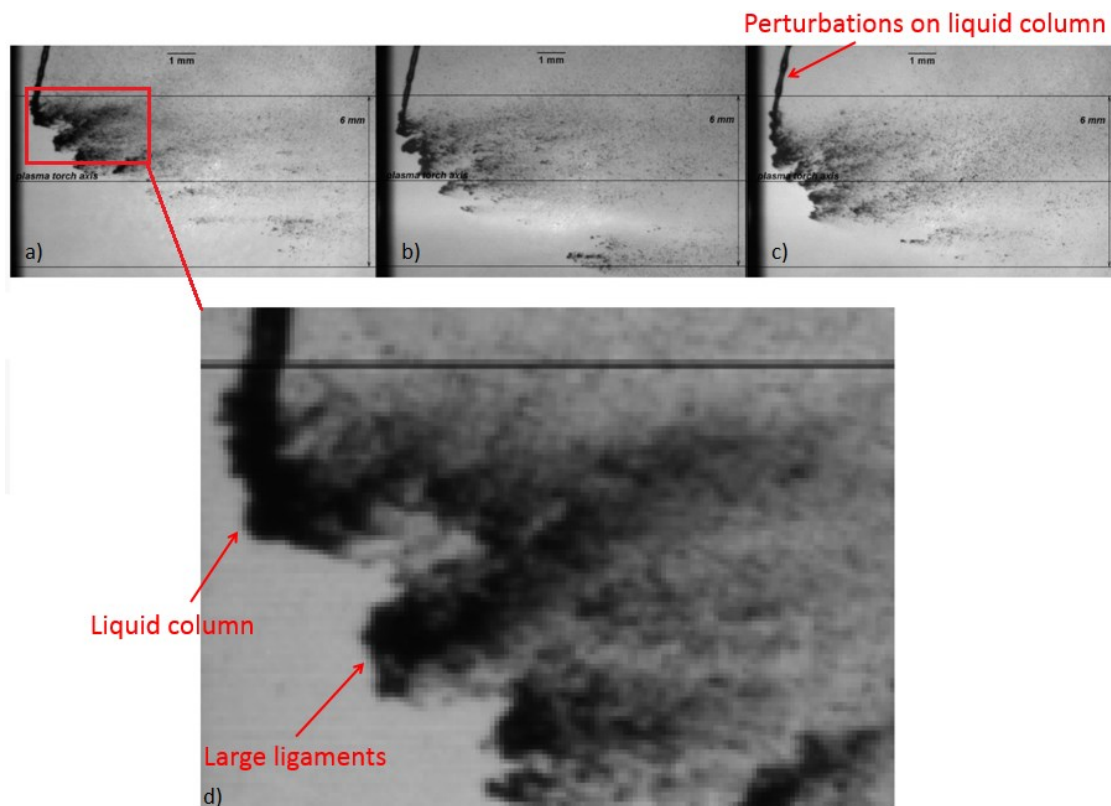


Figure 5.2 Instantaneous images of the interaction of a continuous water jet with dc plasma flow:

a) water pressure=0.25 Mpa, b) water pressure=0.45 Mpa, c) water pressure=0.65 Mpa, d)

breakup close-up [179]

Another motivation of this work is from the recent numerical studies that was devoted to modeling the primary breakup of water jet in plasma spray conditions using Volume of Fluid method [38, 39, 74, 181, 182]. Although the plasma flow (e.g. density and temperature) was modeled accurately and its velocity was nonuniform, the mentioned liquid structure (e.g. large ligaments near the interaction point) was not captured. It should be noted that the liquid column instabilities were ignored in the numerical simulations. Therefore, in this study, the effects of cylindrical liquid jet instabilities and perturbations on the spray structure and ligament formation are studied and the empirical correlations, which can be used for validation of computational fluid dynamics (CFD) codes [19, 35, 36, 38, 39, 66, 74, 181-183] are developed.

5.2 Experimental Setup

The current experimental setup to study the injection of liquid jets into transverse free air jets, consists of a liquid injector and a tube to introduce air flow from a high pressure tank. Figures (5.3) and (5.4) show the schematic details of experimental setup and configurations of liquid injector and air tube. Liquid jets are injected vertically downward. The liquid injection system includes a tank, a flow meter, and a nozzle unit. Distilled water is filled into the tank and pressurized with high-pressure air, prior to start of the experiment. Water flow rate is measured by a flowmeter and is used to calculate the water average velocity, U_l , at the nozzle exit. Two liquid nozzles with exit diameters (d) of 0.5 and 1 mm are manufactured for the experiments. The nozzles passages have the inlet diameter of 12 mm, followed by a 45-deg taper to the mentioned nozzle exit diameters, followed by a straight section with a length of 3 mm.

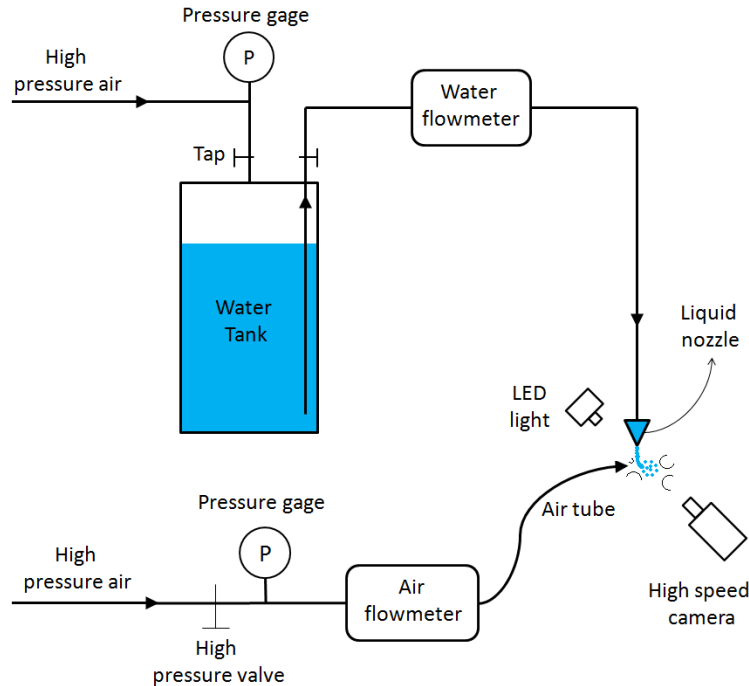


Figure 5.3 Schematic of experimental setup

The air flow is controlled by a high-pressure valve. Two air tubes with exit diameters (D) of 4 and 9.8 mm, and length-to-diameter of 170, are used to generate fully developed flow. Fully developed flow is used in this study because the gas flow in the steady mode of plasma torch is almost fully developed at the gun exit [19, 35, 36, 38, 39, 74, 181-183]. Air tube thickness is around 1.3 mm. The maximum air velocity is measured by a pitot tube at the center point of the air tube exit. The air average velocity is then calculated based on the fully developed pipe flow formulas. The air average speed, U_g , in fully developed laminar pipe flow is one-half of the maximum velocity, and in fully developed turbulent pipe flow, based on the one-seventh power-law velocity profile assumption, is 0.817 of the maximum velocity [198]. In addition, a flowmeter is used to measure the air flow rate to check the accuracy of the calculated air speed.

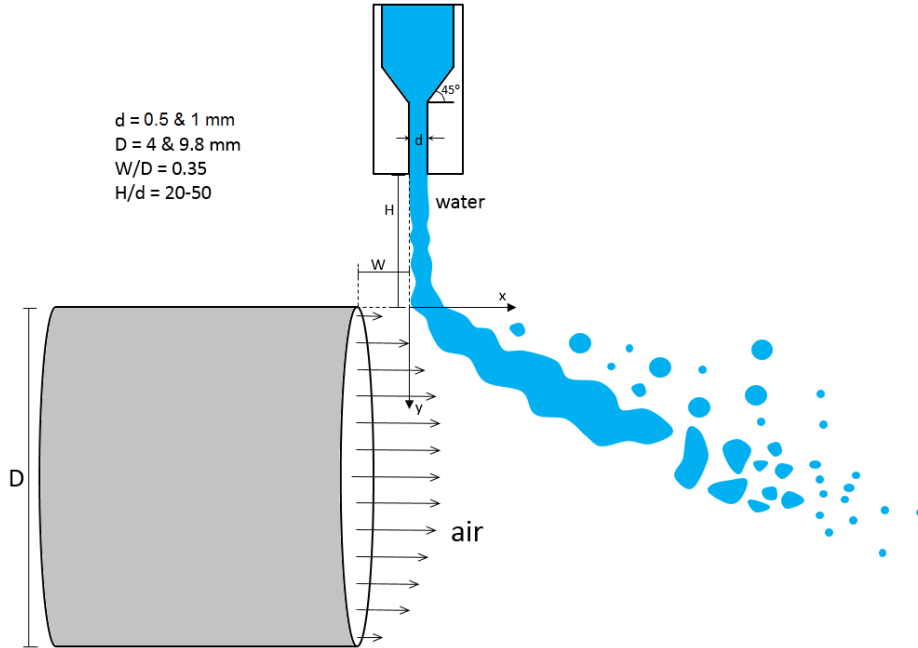


Figure 5.4 Configuration of liquid injector and air tube to study the water jets injection into transverse free air jets

Breakup properties and near field structures are visualized and investigated using a Photron SA1.1 high speed camera (Photron, California, USA) operating at 5,000 frames/s with a resolution of 1024×1024 and an UltraZoom 6000 lens (Navitar, New York, USA). Using an LED light (Schott, California, USA), the shadowgraphy technique (backlighting) is performed to capture instantaneous images of the spray. These images are analyzed and statistically processed to provide the average spray trajectories and the distances to the liquid column breakup point. The optical tools are installed on a traversing mechanism while the liquid injector and air tube are fixed to an optical table.

The axial and vertical distances between the liquid nozzle exit and the air tube are named W and H , respectively (see Figure (5.4)). In this study, W/D is constant and equal to 0.35 ± 0.03 , and H/d varies between 20 and 50. Moreover, H is less than $3/4$ of the breakup length of a cylindrical

liquid jet in still air (see references [175, 176] for detailed discussion on the stated breakup length). The mentioned numbers are set with respect to the values used in typical suspension-solution thermal sprays. Air speed is varied to attain different gaseous Weber numbers ($We = \rho_g U_g^2 d / \sigma$ where ρ_g is gas density, and σ is the liquid surface tension) in the range of 1 to 230. In addition, liquid-to-gas momentum flux ratios ($q = \rho_l U_l^2 / \rho_g U_g^2$ where ρ_l is the water density) are between 1.7 and 138. To achieve acceptable results with an excellent degree of accuracy, each test is repeated five times and the outcomes are reported based on the average of these five tests.

5.3 Results and Discussion

In this section, the results of near field breakup processes in terms of breakup regimes, liquid penetration heights and column breakup points are discussed. In general, the spray field is divided into three modes: intact liquid column, ligaments, and droplets [148, 149, 163]. The primary breakup is referred to as development of hydrodynamics instabilities on the liquid column and generation of ligaments and droplets. The secondary breakup is known as the ligaments fragmentation into small droplets [163]. When the liquid jets are injected downward, the lower surface trajectory of jets in a cross flow is considered as the penetration height or spray trajectory. The liquid column breakup point (CBP) is referred to as the location where the column ceases to exist [42-50, 142, 143, 148, 149, 152, 153, 163, 171-174].

Gaseous Weber number, We , and jet-to-crossflow momentum flux ratio, q , are the most relevant parameters to define the breakup regimes in the process of liquid jet in crossflow. As explained by Wu *et al.* [149], Mazallon *et al.* [44], and Sallam *et al.* [46], based on the gaseous Weber number, four breakup regimes, namely capillary, bag, multimode, and shear breakup, are observed. For instance, Wu *et al.* [149] used wind tunnel experiments to show that the enhanced

capillary breakup occurs when $We < 12$. The reason is that in this condition the liquid surface tension forces are large compared to the aerodynamic forces. In this regime, the liquid column is curved by the aerodynamic forces, that accelerates the breakup caused by the capillary forces. When Weber number is between 12 and 45, aerodynamic forces begin to control the breakup process. Thin bag-shaped membranes similar to bag breakup of a spherical droplet are formed. As Weber number increases ($45 < We < 80$), the liquid column fractures with a mechanism similar to the multimode regime in secondary breakup. Shear-type breakup together with thin bag-shaped membranes can be identified at several locations. As Weber number increases ($We > 80$), the shear breakup becomes dominant. In this regime, droplets are stripped off from the surface of liquid column or ligaments by shear [149]. It is worth mentioning that, Mazallon *et al.* [44] and Sallam *et al.* [46] suggested different critical Weber numbers for transition between the breakup regimes (see Table (5.1)). In addition, Wu *et al.* [149], Mazallon *et al.* [44], and Sallam *et al.* [46] showed that as liquid velocity increases (i.e. increase of q or liquid Weber number), waves on the leeward side of the liquid column (the leeward waves) generates small droplets. This process is known as surface breakup [44, 46, 149, 163]. Noting that droplets generated by surface breakup are smaller than those from column breakup [149, 163].

Table 5.1 Gaseous Weber number to define breakup transition criteria for liquid jet in crossflow

	capillary-to-bag	bag-to-multimode	multimode-to-shear
Wu <i>et al.</i> [149]	$We \sim 12$	$We \sim 45$	$We \sim 80$
Mazallon <i>et al.</i> [44]	$We \sim 5$	$We \sim 60$	$We \sim 110$
Sallam <i>et al.</i> [46]	$We \sim 4$	$We \sim 30$	$We \sim 110$
Current study (based on the air average velocity), $D/d = 19.6$	$We \sim 3.5$	$We \sim 22$	$We \sim 65$
Current study (based on the air maximum velocity), $D/d = 19.6$	$We \sim 5$	$We \sim 33$	$We \sim 100$

The observed four breakup regimes in this study are shown in Figure (5.5). In this figure, $H/d = 35$ and $D/d = 19.6$. Figures (5.5a), (5.5b), (5.5c), and (5.5d) reveal the enhanced capillary, bag, multimode, and shear breakup mechanisms, respectively. Furthermore, Table (5.1) presents the transitional Weber numbers between the breakup regimes in this study (where $D/d = 19.6$), and compares the results with those observed in the wind tunnel experiments [44, 46, 149]. Based on the average air velocity, the critical We for transition between capillary-and-bag, bag-and-multimode, and multimode-and-shear, are 3.5, 22, and 65, respectively. However, using the maximum air velocity in the calculations, the critical We obtained here is aptly matched with the results of Sallam *et al.* [46]. This result is reasonable since the air velocity profile in the fully developed turbulent flow in a tube is similar to the air velocity profile over a flat plate in the wind tunnel test (considering the boundary layer thickness).

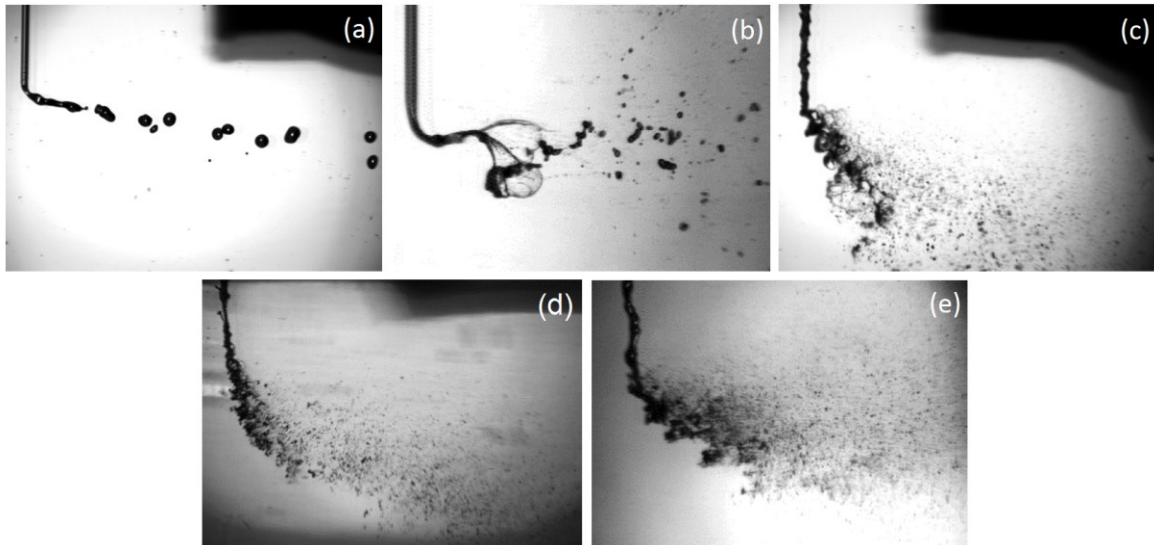


Figure 5.5 Breakup of water jets in transverse free air jets: a) enhanced capillary breakup ($We = 2.5, q = 3.6$), b) bag breakup ($We = 6.7, q = 15$), c) multimode breakup ($We = 25, q = 28$), d) shear breakup ($We = 72, q = 9$), e) surface/column breakup ($We = 175, q = 8.2$)

The mentioned four breakup regimes are observed for different H/d and D/d examined in this study. Although the results show that the effect of H/d on the breakup regimes and critical We are negligible, D/d has some influences on the transitional Weber numbers. Figure (5.6) shows the effect of D/d on the critical We . When D/d is equal to 8, the critical We (based on the air average velocity) for transition between capillary-and-bag, bag-and-multimode, and multimode-and-shear, are approximately 5, 30, and 70, respectively. In other words, by reducing D/d , the critical Weber numbers increases slightly. It should be noted that as the air tube diameter (D) decreases, the air momentum ($\rho_g U_g^2 D \pi / 4$) decreases. It is clear that, in this case, air density or velocity should be increased to enhance the air momentum. By increasing the air density or velocity, the air Weber number increases.

The criteria for the surface breakup existence as a function of Weber number and D/d are shown in Figure (5.6). Figure (5.5e) also shows the surface/column breakup regime. Surface breakup, where small droplets are generated by the leeward waves, occurs when the jet-to-crossflow momentum flux ratio, q , is large. When q is small, the liquid column experiences column breakup without surface breakup [149, 163]. As can be seen in Figure (5.6), Wu *et al.* [149], Tambe *et al.* [148] and Lakhamraju [43] established the mentioned criteria with the slopes of -0.81, -1.94, and -1.42. In the present work however, this criteria has a slope of almost -0.92 for both mentioned D/d . In our experiments, similar to other studies [43, 148, 149], the onset q for surface breakup diminishes by increasing the Weber number. Moreover, the onset q for surface breakup obtained from our experiments is lower than that of Wu *et al.* [149], and is in a good agreement with the recent study of Lakhamraju [43] at high We . The reduction of the onset q for surface breakup in our study, particularly at low We , can be due to the presence of perturbations on the cylindrical liquid jet. As the air velocity increases (i.e. We and q increases and decreases, respectively), the

air speed controls the breakup mechanism instead of the perturbations on the cylindrical liquid jet. Noting that our results are well matched with the findings of Lakhamraju [43] in this matter. Another interesting point in Figure (5.6) is the effect of D/d on the onset q for surface breakup. As can be seen by decreasing D/d , the onset q for surface breakup reduces slightly. This phenomenon can be explained by the discussion presented in the previous paragraph about the air momentum.

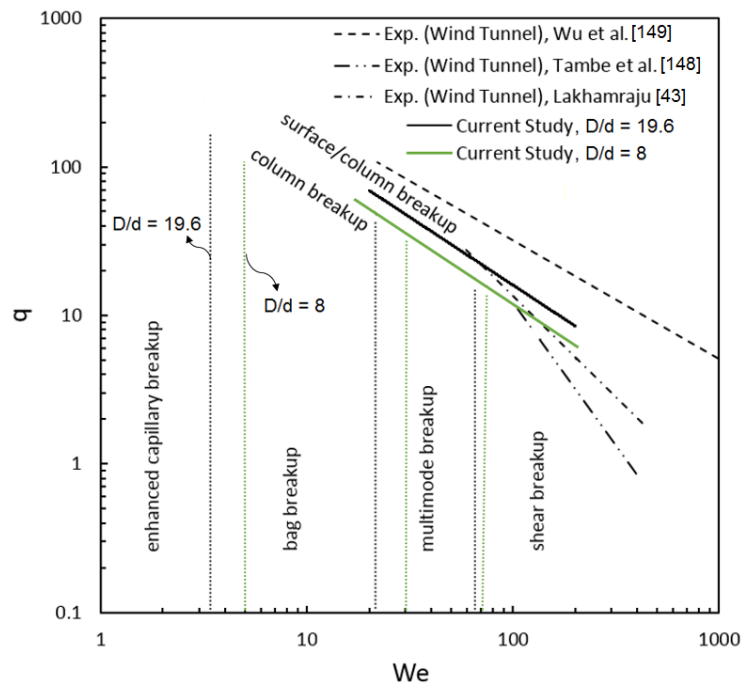


Figure 5.6 Breakup regime map of liquid jets in transverse free air jets

Figure (5.7) illustrates the technique applied in this work to obtain the average CBP location. This technique is the same as the method used by Lubarsky *et al.* [163]. A typical image obtained with a high speed camera and backlighting technique is shown in Figure (5.7a). Using the ImageJ software [199], this raw image is ultimately inverted into a binary field (Figure (5.7b)) by applying

a threshold that is set to the image intensity. The complete boundary of the intact liquid column is obtained by tracking the edge of this binary field. Here, the farthest point on the boundary (i.e. the location where the liquid column ceases to exist) from the coordinate origin is defined as the CBP. The coordinate origin and axes are shown in Figure (5.4). The origin is at the intersection of a vertical line extending downward from the liquid nozzle outlet and a horizontal line through the edge of the air tube (see Figure (5.4)). The positive x and y axes are in the directions of airflow and liquid injection, respectively. Figure (5.7c) indicates the CBP location obtained from the raw image. The CBP location is averaged over 200 images and the average CBP location (x_b, y_b) is shown in Figure (5.7d).

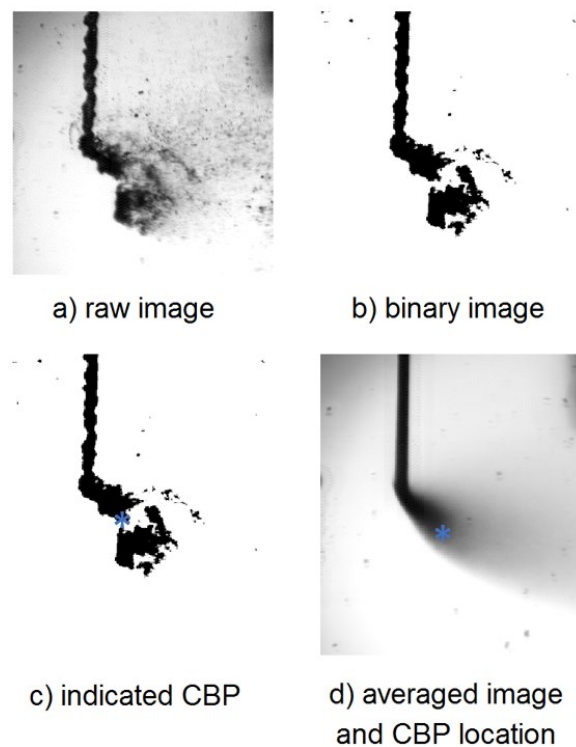


Figure 5.7 The technique used to locate the column breakup point (CBP)

The average location of the column breakup point (x_b, y_b) as a function of momentum flux ratio (q) and gaseous Weber number is shown in Figure (5.8). The data shown in this figure are related to different values of H/d and D/d while the average gaseous Weber number is greater than 70. As shown, x_b/d and y_b/d increase as q increases. On the other hand, these parameters decrease by increasing the gaseous Weber number. It is clearly shown that y_b/d strongly depends on the momentum flux ratio, q .

In Figure (5.9), the effects of H/d and D/d on the CBP location at relatively low and high We and q (i.e. $We = 50, 200$ and $q = 5, 20$) are shown. As can be seen, for high We and q , H/d does not have any effects on the CBP location and the data related to different D/d are disorderly distributed over the averaged value (i.e. solid line). In the case of low We and q , increasing H/d and D/d causes the CBP location decreases slightly. In general, our results show that when We is high (high We region is focused here because in suspension-solution thermal spray, the gaseous Weber number is typically more than 200 [12]), x_b/d and y_b/d are independent of D/d , H/d , and are functions of momentum flux ratio and gaseous Weber number (see Figures (5.8), and (5.9)). Therefore, for $We > 70$, a correlation for x_b/d is developed as follows

$$\frac{x_b}{d} = 10.79 We^{-0.33} q^{0.11} \quad \text{Equation 5.1}$$

where the correlation coefficient for the fit is 0.91, the standard deviation is 0.7, and the experimental uncertainty is approximately $\pm 8\%$. The correlation for estimating the transverse height of the column breakup point (i.e. y_b/d) is given below (for $We > 70$)

$$\frac{y_b}{d} = 2.655 We^{-0.127} q^{0.3} \quad \text{Equation 5.2}$$

where the correlation coefficient for the fit is 0.95, the standard deviation is 0.37, and the experimental uncertainty is about $\pm 7\%$.

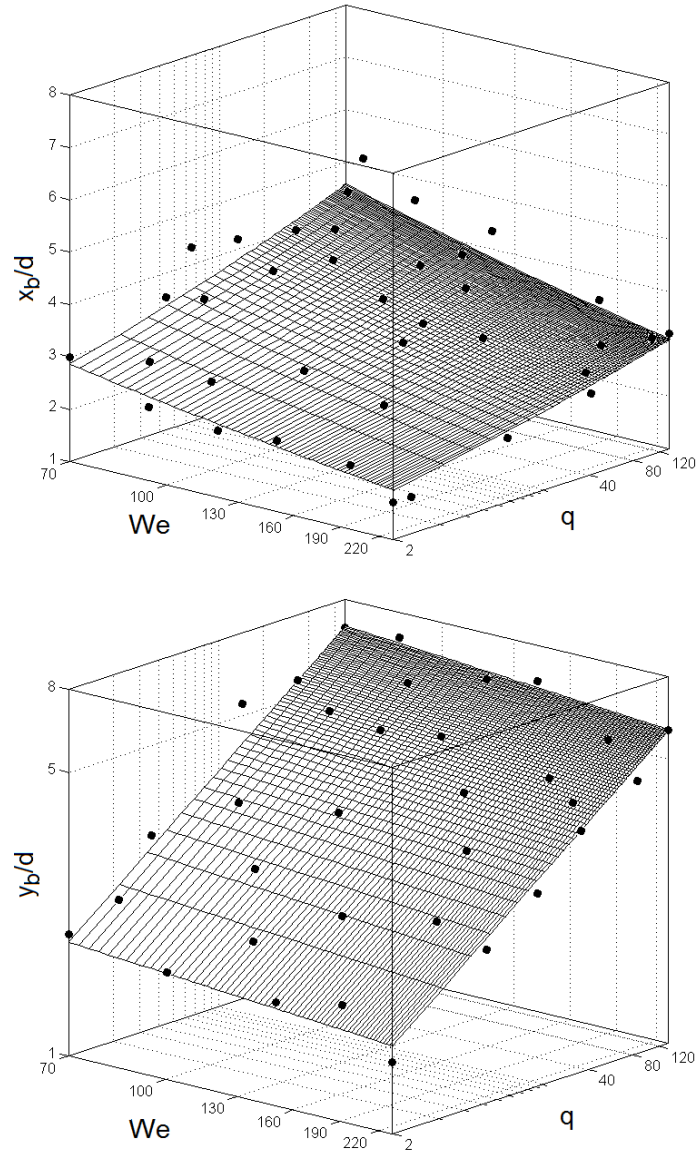


Figure 5.8 Location of the liquid column breakup point (CBP) as a function of gaseous Weber number and momentum flux ratio (based on the average gas velocity at the nozzle exit) for different values of D/d , and H/d

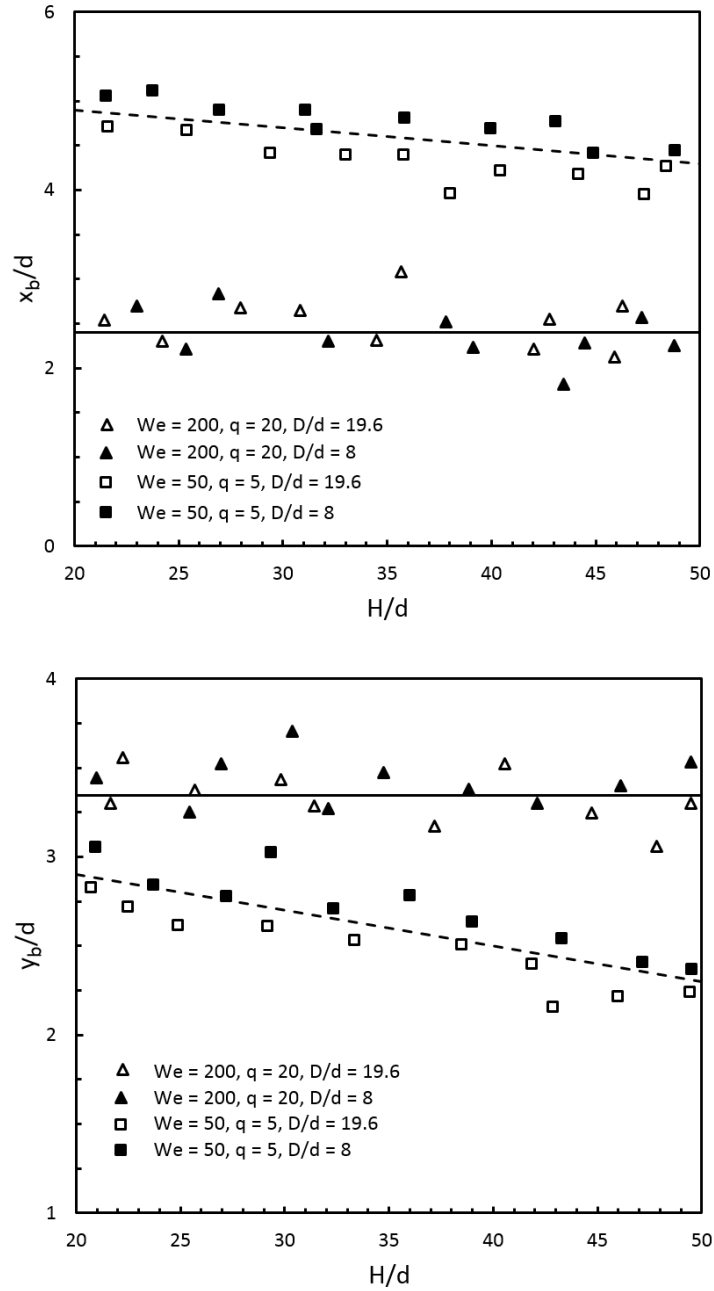


Figure 5.9 Location of the liquid column breakup point (CBP) as a function of D/d , and H/d

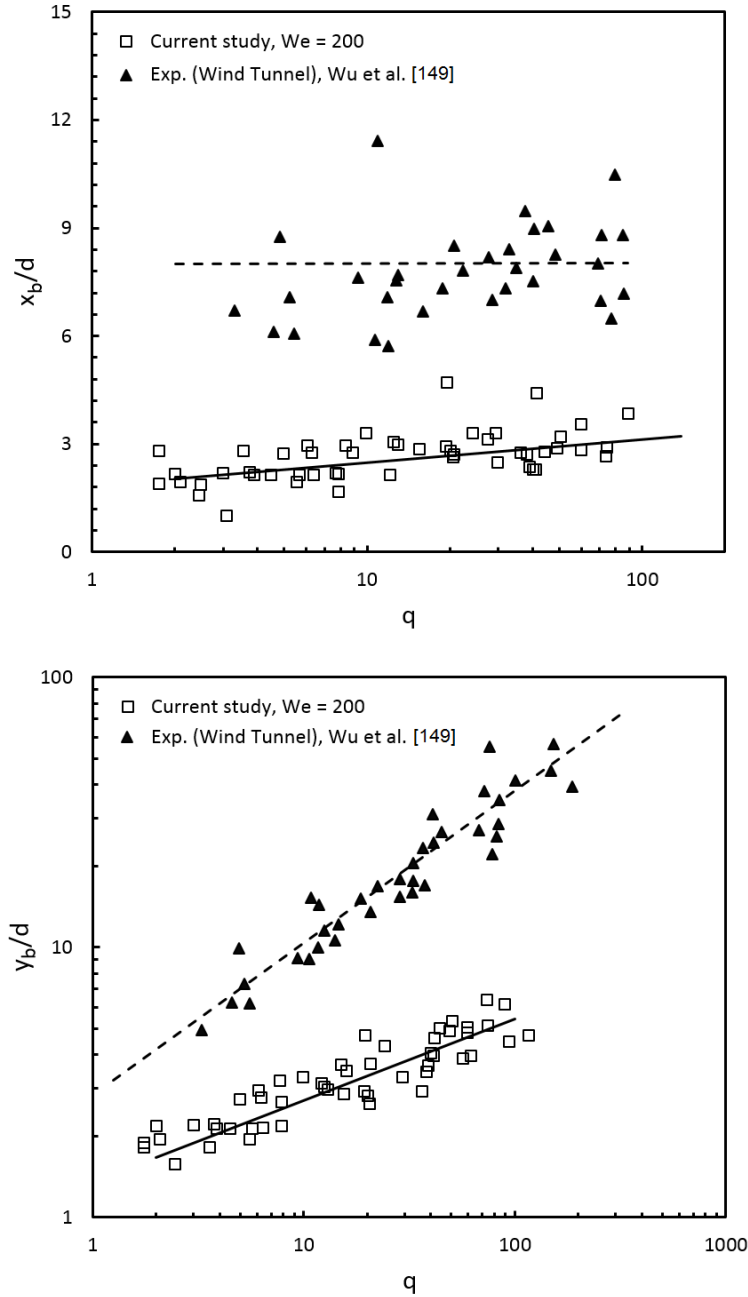


Figure 5.10 Comparison of the location of liquid column breakup point (CBP) obtained in this study with the results of Wu *et al.* [149]

It is worth mentioning that, x_b/d estimated in the present work is smaller compared to the results of Wu *et al.* [149], Sallam *et al.* [46], and Lee *et al.* [42] (see Figure (5.10)). Wu *et al.* [149]

and Sallam *et al.* [46] discussed that x_b/d for nonturbulent liquid jet in crossflow is constant and around 8. In addition, Lee *et al.* [42] explained that x_b/d for turbulent liquid jet in crossflow is also constant and equal to 5.2. However, Lubarsky *et al.* [163] found that x_b/d is a function of q and gaseous Weber number (similar results are obtained in the current work). They showed that x_b/d decreases as q and We increase [163]. They also reported that x_b/d in their investigated operational conditions (i.e. $2 < q < 200$, and $50 < We < 1500$) are in the range of 1-4 [163]. As mentioned above and shown in Figures (5.8) and (5.10), in contrast to the work of Lubarsky *et al.* [163], our results reveal that x_b/d increases slightly as q increases. Figure (5.10) also shows the values of y_b/d reported by Wu *et al.* [149], which is much higher than our results. However, Lubarsky *et al.* [163] reported that y_b/d for their investigated operational conditions is between 2 and 6.

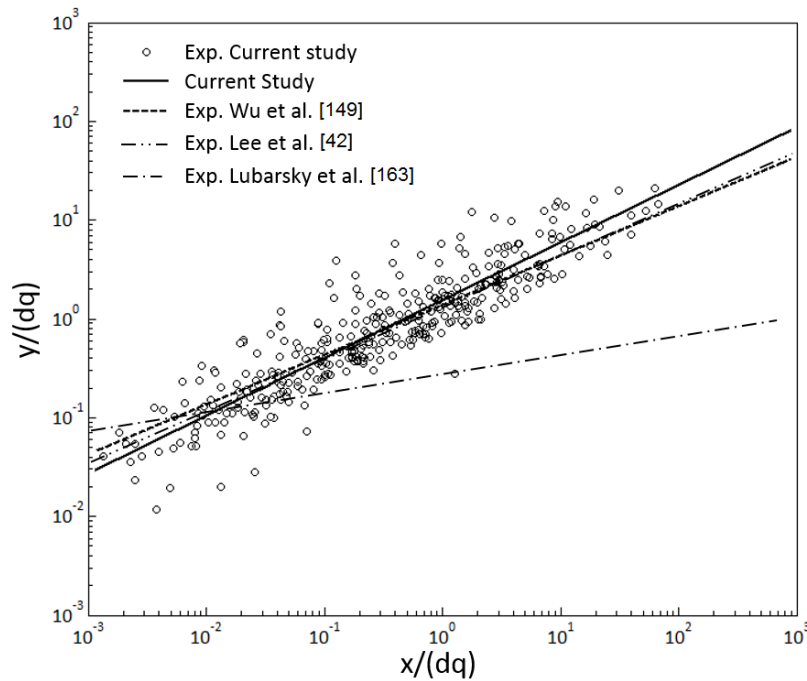


Figure 5.11 Liquid penetration height (spray trajectory) as a function of liquid-to-gas momentum flux ratio, q

Figure (5.11) shows the dependency of the spray penetration height (i.e. spray trajectory) to liquid-to-air momentum flux ratio, q , while gaseous Weber number (based on the average gas velocity) is greater than 40. In order to characterize the lower boundary of the spray pattern, each of the several thousand images captured by the high speed camera is processed individually. Using ImageJ software [199], threshold is applied to the raw images prior to generation of the binary fields. The spray trajectory is considered as the line that divides white and black zones in the binary image (see Figure (5.7)) [163]. Finally, the mean spray trajectory is calculated using conventional algorithms. As in other previous studies [148, 149, 163], our experiments demonstrate that the spray trajectory is dependent of q and independent of We , H/d , and D/d . As shown in Figure (5.11), by increasing liquid-to-gas momentum flux ratio, q , the liquid penetration height increases significantly. The following correlation for the spray penetration height is developed in this work

$$\frac{y}{d} = 1.538q^{0.42} \left(\frac{x}{d}\right)^{0.582} \quad \text{Equation 5.3}$$

where the experimental uncertainty is around $\pm 7\%$, the standard deviation is 0.21, and the correlation coefficient for the fit is 0.94. It should be noted that there is an excellent agreement between our experimental data and correlation, with the results obtained by Wu *et al.* [149] and Lee *et al.* [42] (shown in Figure (5.11)). On the other hand, the spray trajectory obtained here is significantly different from the results reported by Lubarsky *et al.* [163].

Figure (5.12) shows a sequence of images captured in this study where $We = 200$ and $q = 15$. The time interval between the images is 0.4 ms. These images illustrate that large ligaments exist close to the interaction point of liquid and air jets in our experiments. Due to presence of such large ligaments, our results in terms of CBP location are significantly different from the results obtained from wind tunnel tests (e.g. [42, 46, 149]). However, these ligaments do not change the spray trajectory in comparison with the results of wind tunnel tests [149]. As explained above,

these large ligaments are also observed in suspension plasma spray conditions (see Figure (5.2)) and our results show that one of the main reasons of their existence is the liquid column perturbations and instabilities. In other words, after ejection of liquid from the orifice, the instabilities appear and grow on the liquid column. Then, by the interaction of liquid jet with high speed gas flow, the liquid fragment (i.e. large ligament) ejects from the main flow at the point that liquid jet diameter is small (see the red arrow in Figure (5.12)).

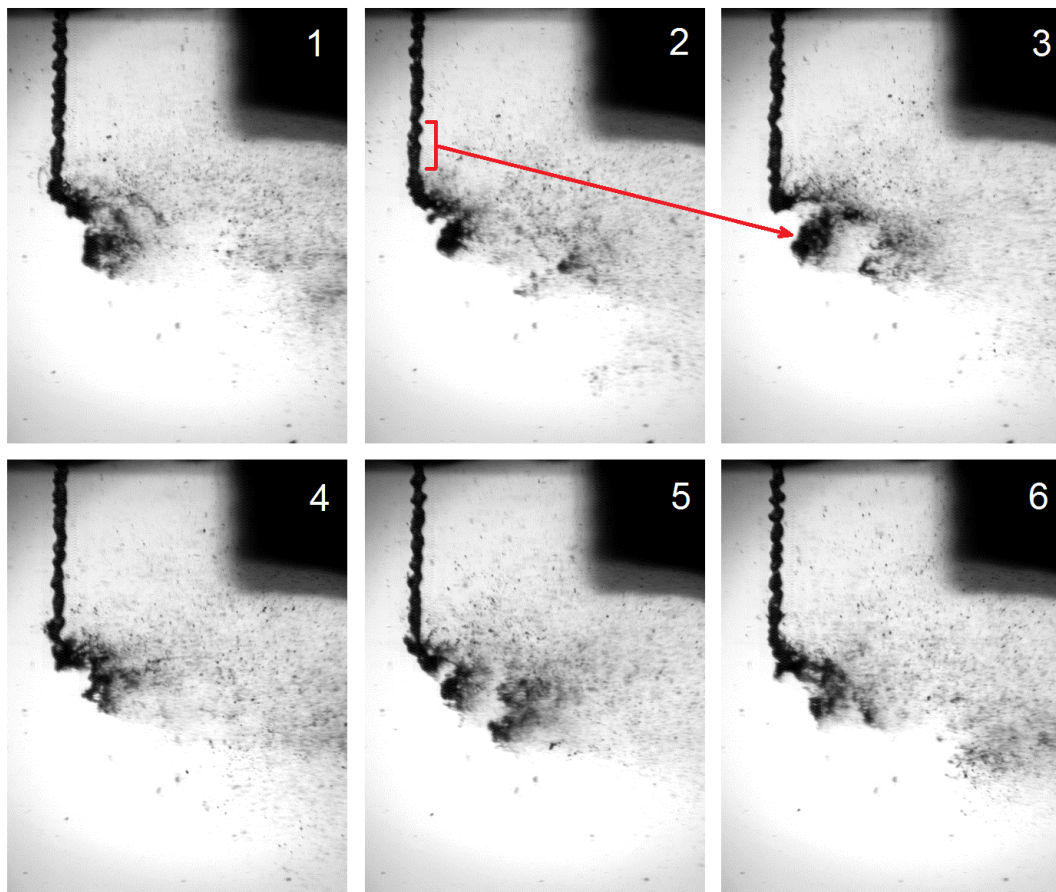


Figure 5.12 A series of captured images with time difference of 0.4 ms

It is worth mentioning that all the above discussions such as breakup mechanisms, established transitional Weber numbers, liquid column breakup point, and penetration height strongly depend

on the axial distance between the liquid nozzle exit and the air tube (W). As mentioned above the parameter W/D is kept constant ($=0.35\pm 0.03$) in this study. However, as this parameter increases, the breakup mechanism might change, the intact liquid column becomes oscillatory, and the penetration height increases dramatically. The main reasons are the velocity relaxation inside the gaseous jet, and the expansion in the free jet diameter. Figure (5.13) shows that increasing W/D changes the breakup mechanism from bag to capillary (We and q are calculated based on the average gas velocity at the tube exit). When $W/D < 0.35$, the velocity relaxation inside the gaseous jet is not significant, and does not have considerable effects on the above results.

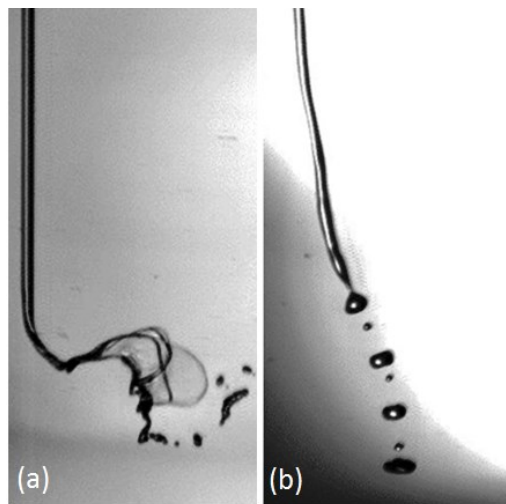


Figure 5.13 Effect of axial distance between the liquid nozzle exit and the air tube on breakup mechanisms and penetration height: a) bag breakup ($We = 6.7, q = 5.6, H/d = 35, W/D = 3.75$), b) enhanced capillary breakup ($We = 6.7, q = 5.6, H/d = 35, W/D = 14.5$)

5.4 Summary and Conclusions

As a fundamental study in the field of suspension-solution thermal sprays, the primary breakup of water jets in transverse free air jets is investigated at room conditions using

shadowgraphy technique. The main goals are understanding the effects of liquid column perturbations and instabilities, and ratio of gas nozzle-to-liquid orifice diameter on the breakup mechanisms, ligaments formations, and spray trajectory. Four breakup regimes (i.e. capillary, bag, multimode, and shear breakup) are observed based on the gaseous Weber number, We . It is shown that the diameter ratio has slight influences on the critical We and the onset of surface breakup. Moreover, the effects of momentum flux ratio, the distance between air tube and liquid orifice, gaseous Reynolds and Weber numbers on the location of liquid column breakup point (CBP) are studied in this work. It is found that the liquid column instabilities and momentum flux ratio affect the CBP location significantly. In other words, these instabilities lead to formation of large ligaments near the interaction point of liquid and gas jets. However, the spray trajectory found in the current study is almost the same as the trajectory obtained from the wind tunnel tests. It is also found that there is a similarity between the results of the current study and the results obtained from the water jet in plasma crossflow (see Figures (5.2) and (5.12)). Therefore, the empirical correlations developed here can be used to estimate the liquid breakup behavior, and droplets trajectories in the suspension plasma spray conditions. Our results also clears that to control the droplet size distribution, droplets trajectories, and evaporation rates, the liquid column perturbations and instabilities as the main reason of large ligaments formation should be controlled. In addition, in numerical simulations, to model the liquid behavior and to estimate the droplet size distribution, the liquid column perturbations and instabilities should be taken into account.

Chapter 6

Conclusions and Suggestions for Future Work

6.1 Summary

Investigating and understanding the physical phenomena involved in the suspension thermal spray processes are the main aims of this work. Although fine microstructure coatings generated by the suspension thermal spray technique have unique properties, controlling and improving the process are still challenging. It is worth mentioning that the effects of many parameters such as suspension breakup on the particle temperature and kinetic energy, and the coatings quality have not been completely understood yet. As a first step to reach the mentioned goals, a numerical model was developed (see chapters 2 and 3 [35, 101]). The model was based on the Eulerian-Lagrangian approach and was able to simulate the droplet breakup, liquid evaporation, particle in-flight behavior near the substrate, and particle impact conditions.

The model was applied to simulate the suspension plasma spray process [35]. The Kelvin-Helmholtz Rayleigh-Taylor (KHRT) model was used to simulate the droplet breakup. Flat substrates were located at different standoff distances ranging from 40 to 60 mm. It was found that by adding the substrate into the computational domain, the plasma temperature near the substrate increases. Furthermore, close to the substrate, many particles are decelerated and get diverted by the stagnation region. The Stokes number of the particles that move near the substrate and jet centerline were calculated. It was found that, the Stokes number of particles that are close to the

centerline can be between 0.1 and 2. On the other hand, for the particles that are far from the centerline, it is lower than 0.1.

In addition to suspension plasma spray, the suspension HVOF process was simulated using the mentioned Eulerian-Lagrangian approach [101]. In this case, since the Weber number is relatively low, Taylor Analogy Breakup (TAB) model was applied for simulation of the breakup process. The eddy dissipation model was used to simulate the propylene-oxygen, ethanol-oxygen, and ethylene glycol-oxygen reactions. It was shown that the chamber pressure increases by injection of suspension droplets. In addition, it was revealed that the particle trajectory is significantly influenced by the shock diamonds and turbulent mixing layer. In suspension HVOF process, compared to the typical HVOF process, the particle trajectory deviation is more severe due to lower Stokes number. A correlation was developed to determine spray cross section diameter (i.e. particle trajectory deviation) as a function of standoff distance.

Primary breakup of a liquid jet in crossflows was studied in more details [141, 164], because it mainly controls the particle trajectory and in-flight behavior. It should be noted that the crossflow in the suspension plasma spray process is nonuniform and oscillatory. In chapter 4, the effect of nonuniform crossflow on the liquid breakup mechanism, penetration height, and column deformation was studied numerically using the coupled level set and volume of fluid (VOF) method. It is clear that, when the crossflow is nonuniform, the Weber number and momentum flux ratio change considerably along the liquid column. It was found that the nonuniform crossflow has significant influence on the liquid penetration height and column waves structures. A general correlation for liquid penetration height as a function of crossflow velocity profile was developed. As mentioned above, the TAB and KHRT models are functions of the Weber number and,

therefore, the outcomes of this fundamental study can be used to calibrate these models and improve their accuracy for thermal spray conditions.

The effects of liquid column perturbations, the distance between the liquid orifice and gas nozzle, and ratio of gas nozzle-to-liquid orifice diameter on the breakup mechanisms, ligaments formations, and spray trajectory were experimentally investigated. It was found that the liquid column perturbations significantly influence the location of liquid column breakup point. The stated perturbations result in the formation of large ligaments near the interaction point of liquid and gas jets. On the other hand, these perturbations do not change the liquid penetration height compared to the results obtained from the wind tunnel tests. The two important outcomes of these experiments are; i) the liquid column perturbations have important influences on the droplet size distribution, trajectory, evaporation rate and etc., and ii) due to the formation of large ligaments near the gas-liquid interaction point, the assumption of droplet injection and using KHRT model to simulate the breakup phenomenon seem to be reasonable.

6.2 Scope for Research and Future Work

In general, suspension thermal spray is a new technique and the effects of many parameters and mechanisms in this process are not explored yet. Therefore, there is a wide range of research topics in this area, such as suspension preparation and storage, suspension breakup and evaporation/combustion, coatings buildup, rarefied flow effects, and etc. Numerical modeling of suspension/particle in-flight behavior was focused here and, therefore, some future works in this area will be suggested. In the following, more topics that can be considered for future research are briefly presented.

- Analyzing the effect of density ratio on the liquid jet primary breakup and droplet secondary breakup; in suspension plasma spray, the density ratio is too large and is around 50,000 [164]. It might have significant influences on the breakup mechanisms, liquid penetration height, and droplet size distribution.
- Investigating the effect of liquid injection angle on the breakup mechanisms, and droplet size distribution.
- Numerical modeling of spray injection into the plasma plume and HVOF torch; the spray can be generated by Effervescent or airblast atomizers [200, 201].
- Studying the behavior of liquid jet in an oscillating crossflow; in this case, the oscillation frequency can change the spray trajectory, surface waves' structures, and droplet size distribution [202].
- Using non-circular nozzles (e.g. elliptical nozzles) for suspension injection; the axis-switching phenomenon might result in a lower value of Sauter mean diameter (SMD). Therefore, it can have significant influences on particle in-flight behavior and the coatings quality.
- Measuring/calculating the thermophysical and transport properties of materials (e.g. mass diffusivity, and viscosity) at high temperature. In addition, the dynamic surface tension of suspensions should be measured and empirical and theoretical correlations should be provided since this dynamic parameter controls the breakup phenomena [1, 203].
- Coupling of interface capturing methods such as VOF and CLSVOF with Lagrangian spray method; using this approach, both primary and secondary atomization can be

modeled more accurately [151]. In addition, after completion of breakup and liquid evaporation, fine particles can be tracked through the computational domain.

- Improving VOF-LES coupling by providing an LES subgrid model for liquid/gas interface dynamics [204, 205].
- Studying the suspension evaporation/combustion mechanisms and modeling the micro-explosion phenomena [1, 206]. These phenomena have some effects on the particle agglomerations' size and velocity.
- Modifying the Nusselt number correlation and heat transfer coefficient by adding the effects of Knudsen number. Furthermore, the thermophoretic force should be added to the model [1, 21]. In addition, more accurate turbulence models such as LES should be used to simulate the suspension thermal spray processes.
- Investigating the effects of substrate location and shape on in-flight particle characteristics in suspension HVOF process; since the standoff distance in this process is relatively short, a bow shock might happen near the substrate. This shock can change the particle trajectory and velocity significantly.
- Adding the conjugate heat transfer method to the mentioned Eulerian-Lagrangian model in order to estimate the substrate temperature distribution.
- Study of droplet/particle impact on the substrate, splat formation, and coatings buildup; it can provide an accurate boundary condition for particle-substrate interaction in our model.
- Parametric study and optimizing the torch geometry, suspension injector type, shape, and location.

References

- [1] M. Jadidi, S. Moghtadernejad and A. Dolatabadi, "A comprehensive review on fluid dynamics and transport of suspension/liquid droplets and particles in high-velocity oxygen-fuel (HVOF) thermal spray," *Coatings*, vol. 5, no. 4, pp. 576-645, 2015.
- [2] L. Pawlowski, *The Science and Engineering of Thermal Spray Coatings*, 2nd ed., Chichester, West Sussex, UK: John Wiley & Sons, 2008.
- [3] R. Heimann, *Plasma Spray Coating: Principles and Applications*, 2nd ed., Weinheim, Germany: Wiley-VCH Verlagsgesellschaft mbH, 1996.
- [4] V. Sobolev, J. Guilemany and J. Nutting, *High Velocity Oxy-Fuel Spraying: Theory, Structure-Property Relationships and Applications*, London, UK: Maney Publishing, 2004.
- [5] M. Li and P. Christofides, "Modeling and control of high-velocity oxygen-fuel (HVOF) thermal spray: A tutorial review," *J. Therm. Spray Technol.*, vol. 18, pp. 753-768, 2009.
- [6] M. Oksa, E. Turunen, T. Suhonen, T. Varis and S. Hannula, "Optimization and characterization of high velocity oxy-fuel sprayed coatings: Techniques, materials, and applications," *Coatings*, vol. 1, pp. 17-25, 2011.
- [7] P. Fauchais, G. Montavon, R. Lima and B. Marple, "Engineering a new class of thermal spray nano-based microstructures from agglomerated nanostructured particles, suspensions and solutions: An invited review," *J. Phys. D: Appl. Phys.*, vol. 44, no. 9, p. 093001, 2011.
- [8] L. Pawlowski, "Suspension and solution thermal spray coatings," *Surf. Coat. Technol.*, vol. 203, pp. 2807-2829, 2009.
- [9] F. Toma, L. Berger, D. Jacquet, D. Wicky, I. Villaluenga, Y. de Miguel and J. Lindelov, "Comparative study on the photocatalytic behavior of titanium oxide thermal sprayed coatings from powders and suspensions," *Surf. Coat. Technol.*, vol. 203, pp. 2150-2156, 2009.
- [10] A. Killinger, M. Kuhn and R. Gadow, "High-velocity suspension flame spraying (HVSFS), a new approach for spraying nanoparticles with hypersonic speed," *Surf. Coat. Technol.*, vol. 201, pp. 1922-1929, 2006.
- [11] C. Marchand, G. Mariaux, M. Vardelle and A. Vardelle, "Injection and aerodynamic fragmentation of liquid precursors under plasma spray conditions," in *2nd International Workshop on Suspension and Solution Thermal Spraying*, Tours, France, 5-7 June 2008.
- [12] J. Fazilleau, C. Delbos, V. Rat, J. Coudert, P. Fauchais and B. Pateyron, "Phenomena involved in suspension plasma spraying part 1: Suspension injection and behavior," *Plasma Chem. Plasma Process*, vol. 26, pp. 371-391, 2006.
- [13] P. Fauchais, G. Montavon and G. Bertrand, "From powders to thermally sprayed coatings," *J. Therm. Spray Technol.*, vol. 19, pp. 56-80, 2010.

- [14] W. Yu, D. France, J. Routbort and S. Choi, "Review and comparison of nanofluid thermal conductivity and heat transfer enhancements," *Heat Transfer Eng.*, vol. 29, pp. 432-460, 2008.
- [15] A. Ghadimi, R. Saidur and H. Metselaar, "A review of nanofluid stability properties and characterization in stationary conditions," *Int. J. Heat Mass Transfer*, vol. 54, pp. 4051-4068, 2011.
- [16] L. Schramm, *Suspensions: Fundamentals and Applications in the Petroleum Industry*, Washington, DC, USA: The American Chemical Society, 1996.
- [17] D. Litchfield and D. Baird, "The rheology of high aspect ratio nano-particle filled liquids," *Rheol. Rev.*, pp. 1-60, 2006.
- [18] R. Gadow, A. Killinger and J. Rauch, "Introduction to high-velocity suspension flame spraying (HVSFS)," *J. Therm. Spray Technol.*, vol. 17, pp. 655-661, 2008.
- [19] F. Jabbari, M. Jadidi, R. Wuthrich and A. Dolatabadi, "A numerical study of suspension injection in plasma spraying process," *J. Therm. Spray Technol.*, vol. 23, pp. 3-13, 2014.
- [20] L. Fan and C. Zhu, *Principles of Gas-Solid Flows*, Cambridge, UK: Cambridge University Press, 1998.
- [21] C. Crowe, M. Sommerfeld and Y. Tsuji, *Multiphase Flows with Droplets and Particles*, Boca Raton, FL, USA: CRC Press, 1998.
- [22] R. Berry, "Ensemble Averaged Conservation Equations for Multiphase, Multi-Component, and Multi-Material Flows," in Idaho National Engineering and Environmental Laboratory, Bechtel BWXT Idaho, INEEL/EXT-03-01011, ID, USA, 2003.
- [23] B. Kashiwa and R. Rauenzahn, "A Multimaterial Formalism," Los Alamos National Laboratory, Technical Report LA-UR-94-771, NM, USA, 1994.
- [24] A. Dolatabadi, J. Mostaghimi and V. Pershin, "Modeling dense suspension of solid particles in highly compressible flows," *Int. J. Comput. Fluid Dyn.*, vol. 18, pp. 125-131, 2004.
- [25] B. Samareh and A. Dolatabadi, "Dense particulate flow in a cold gas dynamic spray system," *J. Fluids Eng.*, vol. 130, no. 8, p. 081702, 2008.
- [26] M. Bidabadi, A. Shabani Shahrabaki, M. Jadidi and S. Montazerinejad, "An Analytical Study of Radiation Effect on the Premixed Laminar Flame of Aluminum Dust Clouds," *Proc. Inst. Mech. Engrs. Part C J. Mech. Engng. Sci.*, vol. 224, no. 8, pp. 1679-1695, 2010.
- [27] M. Jadidi, M. Bidabadi and M. Hosseini, "Predictions of Laminar Flame in Aluminum Dust Clouds with a Two-Dimensional Analytical Model," *Proc. Inst. Mech. Engrs. Part G J. Aerosp. Engng.*, vol. 223, no. 7, pp. 915-925, 2009.
- [28] M. Jadidi, M. Bidabadi and A. Shahrabaki, "Quenching Distance and Laminar Flame Speed in a Binary Suspension of Solid Fuel Particles," *Latin Am. Appl. Res.*, vol. 40, pp. 39-45, 2010.

- [29] ANSYS FLUENT Theory Guide, Release 14.0, Cecil Township, PA, USA: ANSYS, Inc., 2011.
- [30] M. Taleby and S. Hossainpour, "Numerical investigation of high velocity suspension flame spraying," *J. Therm. Spray Technol.*, vol. 21, pp. 1163-1172, 2012.
- [31] E. Gozali, S. Kamnis and S. Gu, "Numerical investigation of combustion and liquid feedstock in high velocity suspension flame spraying process," *Surf. Coat. Technol.*, vol. 228, pp. 176-186, 2013.
- [32] E. Gozali, M. Mahrukh, S. Gu and S. Kamnis, "Numerical analysis of multicomponent suspension droplets in high-velocity flame spray process," *J. Therm. Spray Technol.*, vol. 23, pp. 940-949, 2014.
- [33] E. Dongmo, R. Gadow, A. Killinger and M. Wenzelburger, "Modeling of combustion as well as heat, mass, and momentum transfer during thermal spraying by HVOF and HVFSFS," *J. Therm. Spray Technol.*, vol. 18, pp. 896-908, 2009.
- [34] E. Dongmo, A. Killinger, M. Wenzelburger and R. Gadow, "Numerical approach and optimization of the combustion and gas dynamics in high velocity suspension flame spraying (HVFSFS)," *Surf. Coat. Technol.*, vol. 203, pp. 2139-2145, 2009.
- [35] M. Jadidi, M. Mousavi, S. Moghtadernejad and A. Dolatabadi, "A three-dimensional analysis of the suspension plasma spray impinging on a flat substrate," *J. Therm. Spray Technol.*, vol. 24, pp. 11-23, 2015.
- [36] K. Pourang, C. Moreau and A. Dolatabadi, "Effect of Substrate and Its Shape on in-Flight Particle Characteristics in Suspension Plasma Spraying," *J. Therm. Spray Technol.*, vol. 25, no. 1, pp. 44-54, 2016.
- [37] C. Marchand, C. Chazelas, G. Mariaux and A. Vardelle, "Liquid precursor plasma spraying: Modeling the interactions between the transient plasma jet and the droplets," *J. Therm. Spray Technol.*, vol. 16, pp. 705-712, 2007.
- [38] S. Vincent, G. Balmigere, C. Caruyer, E. Meillot and J. Caltagirone, "Contribution to the modeling of the interaction between a plasma flow and a liquid jet," *Surf. Coat. Technol.*, vol. 203, pp. 2162-2171, 2009.
- [39] C. Caruyer, S. Vincent, E. Meillot and J. Caltagirone, "Modeling the first instant of the interaction between a liquid and a plasma jet with a compressible approach," *Surf. Coat. Technol.*, vol. 205, pp. 974-979, 2010.
- [40] O. Elshamy, S. Tambe, J. Cai and S. Jeng, "Structure of liquid jets in subsonic crossflow at elevated ambient pressures," in *44th AIAA Aerospace Sciences Meeting and Exhibit*, Reno, Nevada, 9-12 January 2006.
- [41] M. Herrmann, "The influence of density ratio on the primary atomization of a turbulent liquid jet in crossflow," *Proc. Combust. Inst.*, vol. 33, pp. 2079-2088, 2011.
- [42] K. Lee, C. Aalburg, F. Diez, G. Faeth and K. Sallam, "Primary breakup of turbulent round liquid jets in uniform crossflows," *AIAA J.*, vol. 45, no. 8, pp. 1907-1916, 2007.

- [43] R. Lakhamraju, Liquid jet breakup studies in subsonic airstream at elevated temperatures, Cincinnati, Ohio, USA: Master Thesis, University of Cincinnati, 2005.
- [44] J. Mazallon, Z. Dai and G. Faeth, "Primary breakup of nonturbulent round liquid jets in gas crossflow," *Atomization Sprays*, vol. 9, no. 3, pp. 291-311, 1999.
- [45] R. Ragucci, A. Bellofiore and A. Cavaliere, "Trajectory and momentum coherence breakdown of a liquid jet in high-density air cross-flow," *Atomization Sprays*, vol. 17, pp. 47-70, 2007.
- [46] K. Sallam, C. Aalburg and G. Faeth, "Breakup of round nonturbulent liquid jets in gaseous crossflow," *AIAA J.*, vol. 42, no. 12, pp. 2529-2540, 2004.
- [47] S. Tambe, Liquid jets injected into non-uniform crossflow, Cincinnati, Ohio: PhD Thesis, University of Cincinnati, 2010.
- [48] S. Tambe and S. Jeng, "Three-dimensional penetration and velocity distribution of liquid jets injected transversely into a swirling crossflow," in *ILASS Americas, 22nd Annual Conference on Liquid Atomization and Spray Systems*, Cincinnati, Ohio, 16-19 May 2010.
- [49] S. Tambe, O. Elshamy and S. Jeng, "Liquid jets injected transversely into a shear layer," in *45th AIAA Aerospace Sciences Meeting and Exhibit*, Reno, Nevada, 8-11 January 2007.
- [50] S. Tambe, O. Elshamy and S. Jeng, "Spray properties of liquid jets injected transversely into a shear layer," in *43rd AIAA/ASME/SAE/ASEE Joint Propulsion Conference and Exhibit*, Cincinnati, Ohio, 8-11 July 2007.
- [51] A. Prosperetti and G. Tryggvason, *Computational Methods for Multiphase Flow*, Cambridge, UK: Cambridge University Press, 2009.
- [52] G. Tryggvason, R. Scardovelli and S. Zaleski, *Direct Numerical Simulations of Gas-Liquid Multiphase Flows*, Cambridge, UK: Cambridge University Press, 2011.
- [53] C. Hirt and B. Nichols, "Volume of fluid (VOF) method for the dynamics of free boundaries," *J. Comput. Phys.*, vol. 39, pp. 201-225, 1981.
- [54] J. Brackbill, D. Kothe and C. Zemach, "A continuum method for modeling surface tension," *J. Comput. Phys.*, vol. 100, pp. 335-354, 1992.
- [55] S. Deshpande, L. Anumolu and M. Trujillo, "Evaluating the performance of the two-phase flow solver interFoam," *Comput. Sci. Disc.*, vol. 5, p. 014016, 2012.
- [56] S. Ghods and M. Herrmann, "A consistent rescaled momentum transport method for simulating large density ratio incompressible multiphase flows using level set methods," *Phys. Scr.*, vol. 2013, no. T155, p. 014050, 2013.
- [57] W. Rider and D. Kothe, "Reconstructing volume tracking," *J. Comput. Phys.*, vol. 141, pp. 112-152, 1998.
- [58] F. Xiao, S. Ii and C. Chen, "Revisit to the thinc scheme: A simple algebraic VOF algorithm," *J. Comput. Phys.*, vol. 230, pp. 7086-7092, 2011.

- [59] S. Cummins, M. Francois and D. Kothe, "Estimating curvature from volume fractions," *Comput. Struct.*, vol. 83, pp. 425-434, 2005.
- [60] Y. Renardy and M. Renardy, "PROST: A parabolic reconstruction of surface tension for the volume-of-fluid method," *J. Comput. Phys.*, vol. 183, pp. 400-421, 2002.
- [61] S. Popinet, "An accurate adaptive solver for surface-tension-driven interfacial flows," *J. Comput. Phys.*, vol. 228, pp. 5838-5866, 2009.
- [62] O. Ubbink and R. Issa, "A method for capturing sharp fluid interfaces on arbitrary meshes," *J. Comput. Phys.*, vol. 153, pp. 26-50, 1999.
- [63] M. Francois, S. Cummins, E. Dendy, D. Kothe, J. Sicilian and M. Williams, "A balanced-force algorithm for continuous and sharp interfacial surface tension models within a volume tracking framework," *J. Comput. Phys.*, vol. 213, pp. 141-173, 2006.
- [64] "OpenCFD Ltd.," [Online]. Available: <http://www.openfoam.com>.
- [65] V. Suponitsky, A. Froese and S. Barsky, "Richtmyer-Meshkov instability of a liquid-gas interface driven by a cylindrical imploding pressure wave," *Comput. Fluids*, vol. 89, pp. 1-19, 2014.
- [66] M. Jadidi, M. Tembely, S. Moghtadernejad and A. Dolatabadi, "A coupled level set and volume of fluid method with application to compressible two-phase flow," in *22nd Annual Conference of the CFD Society of Canada*, Toronto, Canada, 1-4 June 2014.
- [67] H. Rusche, *Computational Fluid Dynamics of Dispersed Two-Phase Flows at High Phase Fractions*, London, UK: Ph.D. Thesis, Imperial College of Science Technology and Medicine, 2002.
- [68] A. Albadawi, D. Donoghue, A. Robinson, D. Murray and Y. Delaure, "Influence of surface tension implementation in volume of fluid and coupled volume of fluid with level set methods for bubble growth and detachment," *Int. J. Multiphas. Flow*, vol. 53, pp. 11-28, 2013.
- [69] C. Kees, I. Akkerman, M. Farthing and Y. Bazilevs, "A conservative level set method suitable for variable-order approximations and unstructured meshes," *J. Comput. Phys.*, vol. 230, pp. 4536-4558, 2011.
- [70] M. Sussman and E. Puckett, "A coupled level set and volume-of-fluid method for computing 3D and axisymmetric incompressible two-phase flows," *J. Comput. Phys.*, vol. 162, pp. 301-337, 2000.
- [71] M. Sussman, "A second order coupled level set and volume-of-fluid method for computing growth and collapse of vapor bubbles," *J. Comput. Phys.*, vol. 187, pp. 110-136, 2003.
- [72] J. Sethian and P. Smereka, "Level set methods for fluid interfaces," *Annu. Rev. Fluid Mech.*, vol. 35, pp. 341-372, 2003.

- [73] P. Fauchais, R. Etchart-Salas, V. Rat, J. Coudert, N. Caron and K. Wittmann-Teneze, "Parameters Controlling Liquid Plasma Spraying: Solutions, Sols, or Suspensions," *J. Therm. Spray Technol.*, vol. 17, no. 1, pp. 31-59, 2008.
- [74] E. Meillot, S. Vincent, C. Caruyer, J. Caltagirone and D. Damiani, "From DC Time-Dependent Thermal Plasma Generation to Suspension Plasma-Spraying Interactions," *J. Therm. Spray Technol.*, vol. 18, pp. 875-886, 2009.
- [75] Y. Shan, T. Coyle and J. Mostaghimi, "Numerical Simulation of Droplet Breakup and Collision in the Solution Precursor Plasma Spraying," *J. Therm. Spray Technol.*, vol. 16, pp. 698-704, 2007.
- [76] C. Marchand, A. Vardelle, G. Mariaux and P. Lefort, "Modeling of the Plasma Spray Process with Liquid Feedstock Injection," *Surf. Coat. Technol.*, vol. 202, pp. 4458-4464, 2008.
- [77] D. Lapiere, R. Kearney, M. Vardelle, A. Vardelle and P. Fauchais, "Effect of a Substrate on the Temperature Distribution in an Argon-Hydrogen Thermal Plasma Jet," *Plasma Chem. Plasma Process.*, vol. 14, pp. 407-423, 1994.
- [78] C. Kang, H. Ng and S. Yu, "Comparative Study of Plasma Spray Flow Fields and Particle Behavior Near to Flat Inclined Substrates," *Plasma Chem. Plasma Process.*, vol. 26, pp. 149-175, 2006.
- [79] N. Zuckerman and N. Lior, "Jet Impingement Heat Transfer: Physics, Correlations, and Numerical Modeling," *Advances in Heat Transfer*, vol. 39, pp. 565-631, 2006.
- [80] M. Coussirat, J. v. Beech, M. Mestres, E. Egusguiza, J. Buchlin and X. Escaler, "Computational Fluid Dynamics Modeling of Impinging Gas-Jet Systems: I. Assessment of Eddy Viscosity Models," *J. Fluids Eng.*, vol. 127, pp. 691-703, 2005.
- [81] H. Martin, "Heat and Mass Transfer between Impinging Gas Jets and Solid Surfaces," *Advances in Heat Transfer*, vol. 13, pp. 1-60, 1977.
- [82] H. Matsufuji and E. Hasegawa, "Critical Condition for Collision of Suspended Small Particles with a Body in a Viscous Fluid," *Bull. JSME*, vol. 29, pp. 3375-3382, 1986.
- [83] C. Phillips and S. Kaye, "The Influence of the Viscous Boundary Layer on the Critical Stokes Number for Particle Impacting Near a Stagnation Point," *J. Aerosol Sci.*, vol. 30, pp. 709-718, 1999.
- [84] K. Volkov, "Influence of Turbulence on the Deposition of Particles from a Gas-Dispersed Flow on the Wall," *J. Eng. Phys. Thermophys.*, vol. 77, pp. 894-903, 2004.
- [85] C. Glenford Clum III, The Effects of Particle Size, Chemical Composition and Temperature on Deposition in an Impingement Cooling Scheme, Ohio, USA: M.Sc. Thesis, The Ohio State University, 2013.
- [86] J. Laitone, "Erosion Prediction Near a Stagnation Point Resulting from Aerodynamically Entrained Solid Particles," *J. Aircraft*, vol. 16, pp. 809-814, 1979.

- [87] M. Aghasibeig, M. Mousavi, F. Ben Ettouill, C. Moreau, R. Wuthrich and A. Dolatabadi, "Electrocatalytically active nickel-based electrode coatings formed by atmospheric and suspension plasma spraying," *J. Therm. Spray Technol.*, vol. 23, pp. 220-226, 2014.
- [88] L. Birry and A. Lasia, "Studies of the Hydrogen Evolution Reaction on Raney Nickel-Molybdenum Electrodes," *J. Appl. Electrochem.*, vol. 34, pp. 735-749, 2004.
- [89] R. Bolot, M. Imbert and C. Coddet, "Mathematical Modeling of a Free Plasma Jet Discharging into Air and Comparison with Probe Measurements," in *Thermal Spray 1997: A United Forum for Scientific and Technological Advances*, C.C. Berndt Ed., Ohio, USA, ASM International, 1997, pp. 549-555.
- [90] K. Remesh, S. Yu, H. Ng and C. Berndt, "Computational Study and Experimental Comparison of the In-Flight Particle Behavior for an External Injection Plasma Spray Process," *J. Therm. Spray Technol.*, vol. 12, no. 4, pp. 508-522, 2003.
- [91] Y. Wan, S. Sampath, V. Prasad, R. Williamson and J.R. Fincke, "An Advanced Model for Plasma Spraying of Functionally Graded Materials," *J. Mater. Process. Technol.*, vol. 137, no. 1-3, pp. 110-116, 2003.
- [92] A. Boussagol, G. Mariaux, E. Legros, A. Vardelle and P. Nysten, "3-D Modeling of a D.C. Plasma Jet Using Different Commercial CFD Codes," in *Proceedings of 14th International Symposium On Plasma Chemistry*, Orleans, France, 2000.
- [93] B. Selvan, K. Ramachandran, B. Pillai and D. Subhakar, "Numerical Modelling of Ar-N₂ Plasma Jet Impinging on a Flat Substrate," *J. Therm. Spray Technol.*, vol. 20, pp. 534-548, 2011.
- [94] E. Farvardin, O. Stier, V. Luthen and A. Dolatabadi, "Effect of Using Liquid Feedstock in a High Pressure Cold Spray Nozzle," *J. Therm. Spray Technol.*, vol. 20, pp. 307-316, 2011.
- [95] V. Zinov'ev, *Handbook of Thermophysical Properties of Metals at High Temperatures*, New York, USA: Nova Science Publishers, 1996.
- [96] T. Iida and R. Guthrie, *The Physical Properties of Liquid Metals*, Oxford, UK: Oxford Science Publications, Clarendon Press, 1988.
- [97] P. Desai, "Thermodynamics Properties of Nickel," *Int. J. Thermophys.*, vol. 8, pp. 763-780, 1987.
- [98] R. Dhiman, A. McDonald and S. Chandra, "Predicting Splat Morphology in a Thermal Spray Process," *Surf. Coat. Technol.*, vol. 201, pp. 7789-7801, 2007.
- [99] S. Anderson and E. Longmire, "Particle Motion in the Stagnation Zone of an Impinging Air Jet," *J. Fluid Mech.*, vol. 299, pp. 333-366, 1995.
- [100] W. Burwash, W. Finlay and E. Matida, "Deposition of Particles by a Confined Impinging Jet onto a Flat Surface at $Re = 10^4$," *Aerosol Sci. Technol.*, vol. 40, pp. 147-156, 2006.
- [101] M. Jadidi, S. Moghtadernejad and A. Dolatabadi, "Numerical modeling of suspension HVOF spray," *J. Therm. Spray Technol.*, vol. 25, pp. 451-464, 2016.

- [102] P. Fauchais and G. Montavon, "Latest Developments in Suspension and Liquid Precursor Thermal Spraying," *J. Therm. Spray Technol.*, vol. 19, pp. 226-239, 2009.
- [103] A. Killinger, R. Gadow, G. Mauer, A. Guignard, R. Vaben and D. Stover, "Review of New Developments in Suspension and Solution Precursor Thermal Spray Processes," *J. Therm. Spray Technol.*, vol. 20, pp. 677-695, 2011.
- [104] J. O. Berghaus, J. Legoux, C. Moreau, R. Hui, C. Deces-Petit, W. Qu, S. Yick, Z. Wang, R. Maric and D. Ghosh, "Suspension HVOF Spraying of Reduced Temperature Solid Oxide Fuel Cell Electrolytes," *J. Therm. Spray Technol.*, vol. 17, pp. 700-707, 2008.
- [105] S. Moghtadernejad, M. Tembely, M. Jadidi, N. Esmail and A. Dolatabadi, "Shear driven droplet shedding and coalescence on a superhydrophobic surface," *Phys. Fluids*, vol. 27, p. 032106, 2015.
- [106] S. Moghtadernejad, M. Mohammadi, M. Jadidi, M. Tembely and A. Dolatabadi, "Shear driven droplet shedding on surfaces with various wettabilities," *SAE Int. J. Aerosp.*, vol. 6, pp. 459-464, 2013.
- [107] S. Moghtadernejad, M. Jadidi, M. Tembely and A. Dolatabadi, "Shear driven rivulet dynamics on surfaces with various wettabilities," in *Proceedings of the ASME 2014 International Mechanical Engineering Congress and Exposition*, Montreal, QC, Canada, 14–20 Nov. 2014.
- [108] S. Moghtadernejad, M. Jadidi, M. Tembely, N. Esmail and A. Dolatabadi, "Concurrent droplet coalescence and solidification on surfaces with various wettabilities," *J. Fluids Eng.*, vol. 137, no. 7, p. 071302, 2015.
- [109] S. Moghtadernejad, M. Jadidi, N. Esmail and A. Dolatabadi, "Shear driven droplet coalescence and rivulet formation," *Proc. Inst. Mech. Engrs. Part. C J. Mech. Engng. Sci.*, vol. 230, pp. 793-803, 2016.
- [110] S. Moghtadernejad, Dynamics of Droplet Shedding and Coalescence under the Effect of Shear Flow, Montreal, QC, Canada: Ph.D. Thesis, Concordia University, 2014.
- [111] A. Vardelle, C. Moreau, N. Themelis and C. Chazelas, "A Perspective on Plasma Spray Technology," *Plasma Chem. Plasma Process*, vol. 35, pp. 491-509, 2015.
- [112] R. Gadow, A. Killinger and J. Rauch, "New Results in High Velocity Suspension Flame Spraying (HVSFS)," *Surf. Coat. Tech.*, vol. 202, pp. 4329-4336, 2008.
- [113] A. Dolatabadi, J. Mostaghimi and V. Pershin, "Effect of a Cylindrical Shroud on Particle Conditions in High Velocity Oxy-Fuel Spray Process," *Sci. Technol. Adv. Mat.*, vol. 3, pp. 245-255, 2002.
- [114] J. Anderson Jr., Modern Compressible Flow with Historical Perspective, 2nd ed., Singapore: McGraw-Hill, 1990.
- [115] M. Norman and K. Winkler, "Supersonic jets," Los Alamos Science, Spring/Summer 1985.

- [116] S. Turns, An introduction to combustion, concepts and applications, 2nd ed., Boston, USA: McGraw-Hill, 2000.
- [117] J. Oberste Berghaus and B. Marple, "High-Velocity Oxy-Fuel (HVOF) Suspension Spraying of Mullite Coatings," *J. Therm. Spray Technol.*, vol. 17, pp. 671-678, 2008.
- [118] H. Tabbara and S. Gu, "A Study of Liquid Droplet Disintegration for the Development of Nanostructured Coatings," *AIChE J.*, vol. 58, pp. 3533-3544, 2012.
- [119] S. Kamnis and S. Gu, "3-D modelling of kerosene-fuelled HVOF thermal spray gun," *Chem. Eng. Sci.*, vol. 61, pp. 5427-5439, 2006.
- [120] S. Gordon and B. McBride, "Computer Program for Calculation of Complex Chemical Equilibrium Compositions and Applications," NASA Reference Publication No. 1311, Lewis Research Center, Cleveland, USA, 5 Oct. 1994.
- [121] G. Lorenzetto and A. Lefebvre, "Measurements of drop size on a plain-jet airblast atomizer," *AIAA J.*, vol. 15, pp. 1006-1010, 1977.
- [122] E. Quijada-Maldonado, G. Meindersma and A. de Haan, "Viscosity and Density Data for the Ternary System Water(1)-Ethanol(2)-Ethylene glycol(3) between 298.15 K and 328.15 K," *J. Chem. Thermodynamics*, vol. 57, pp. 500-505, 2013.
- [123] C. Goodson, Simulation of Microwave Heating of Mullite Rods, Virginia, USA: M.Sc. Thesis, Virginia Polytechnic Institute and State University, 1997.
- [124] H. Schneider, K. Okada and J. Pask, Mullite and Mullite Ceramics, Chichester, UK: Wiley, 1994.
- [125] B. Hildmann and H. Schneider, "Heat Capacity of Mullite: New Data and Evidence for a High-Temperature Phase Transformation," *J. Am. Ceram. Soc.*, vol. 8, no. 2, pp. 227-234, 2004.
- [126] S. Azizian and M. Hemmati, "Surface Tension of Binary Mixtures of Ethanol + Ethylene Glycol from 20 to 50 °C," *J. Chem. Eng. Data*, vol. 48, pp. 662-663, 2003.
- [127] S. Tanvir and L. Qiao, "Surface Tension of Nanofluid-Type Fuels Containing Suspended Nanomaterials," *Nanoscale Res. Lett.*, vol. 7, p. 226, 2012.
- [128] B. Brian and J. Chen, "Surface tension of solid-liquid slurries," *AIChE J.*, vol. 33, no. 2, pp. 316-318, 1987.
- [129] G. Taylor, "The shape and acceleration of a drop in high-speed air stream," in *The Scientific Papers of Sir Geoffrey Ingram Taylor*, G.K. Batchelor Ed., Cambridge, UK, Cambridge University Press, 1963, 3, pp. 457-464.
- [130] M. Li and P. Christofides, "Computational study of particle in-flight behavior in the HVOF thermal spray process," *Chem. Eng. Sci.*, vol. 61, pp. 6540-6552, 2006.
- [131] M. Li and P. Christofides, "Multi-scale modeling and analysis of an industrial HVOF thermal spray process," *Chem. Eng. Sci.*, vol. 60, pp. 3649-3669, 2005.

- [132] A. Dolatabadi, J. Mostaghimi and V. Pershin, "High efficiency nozzle for thermal spray of high quality, low oxide content coatings". USA Patent 6,845,929, 2005.
- [133] S. Basu and B. Cetegen, "Modeling of Liquid Ceramic Precursor Droplets in a High Velocity Oxy-Fuel Flame Jet," *Acta Mater.*, vol. 56, pp. 2750-2759, 2008.
- [134] G. Mauer, R. Vaßen and D. Stover, "Comparison and Applications of DPV-2000 and Accuraspray-g3 Diagnostic Systems," *J. Therm. Spray Technol.*, vol. 16, pp. 414-424, 2007.
- [135] F. Tarasi, Suspension plasma sprayed alumina-yttria stabilized zirconia nano-composite thermal barrier coatings: formation and roles of the amorphous phase, Montreal, Canada: Ph.D. Thesis, Concordia University, 2010.
- [136] J. Colmenares-Angulo, K. Shinoda, T. Wentz, W. Zhang, Y. Tan and S. Sampath, "On the Response of Different Particle State Sensors to Deliberate Process Variations," *J. Therm. Spray Technol.*, vol. 20, pp. 1035-1048, 2011.
- [137] S. Sampath, V. Srinivasan, A. Valarezo, A. Vaidya and T. Streibl, "Sensing, Control, and In Situ Measurement of Coating Properties: An Integrated Approach Toward Establishing Process-Property Correlations," *J. Therm. Spray Technol.*, vol. 18, pp. 243-255, 2009.
- [138] J. Bissons, M. Lamontagne, C. Moreau, L. Pouliot, J. Blain and F. Nadeau, "Ensemble In-Flight Particle Diagnostics Under Thermal Spray Conditions," in *Thermal Spray 2001: New Surfaces for a New Millennium*, C.C. Berndt, K.A. Khor, and E.F. Lugscheider, Eds., Materials Park, OH, ASM International, 2001, pp. 705-714.
- [139] S. Moghtadernejad, M. Jadidi, N. Esmail and A. Dolatabadi, "SPH simulation of rivulet dynamics on surfaces with various wettabilities," *SAE Int. J. Aerosp.*, vol. 8, no. 1, pp. 160-173, 2015.
- [140] M. Gorokhovski and M. Herrmann, "Modeling primary atomization," *Annu. Rev. Fluid Mech.*, vol. 40, pp. 343-366, 2008.
- [141] M. Jadidi, S. Moghtadernejad and A. Dolatabadi, "Numerical Simulation of Primary Breakup of Round Nonturbulent Liquid Jets in Shear-Laden Gaseous Crossflow," *Atomization Sprays*, accepted 2016, in press.
- [142] J. Becker and C. Hassa, "Breakup and atomization of a kerosene jet in crossflow at elevated pressure," *Atomization Sprays*, vol. 11, pp. 49-67, 2002.
- [143] T. Inamura and N. Nagai, "Spray characteristics of liquid jets traversing subsonic airstreams," *J. Propul. Power*, vol. 13, no. 2, pp. 250-256, 1997.
- [144] J. Nouri and J. Whitelaw, "Gasoline sprays in uniform crossflow," *Atomization Sprays*, vol. 17, pp. 621-640, 2007.
- [145] M. Rachner, J. Becker, C. Hassa and T. Doerr, "Modeling of the atomization of a plain liquid fuel jet in crossflow at gas turbine conditions," *Aerosp. Sci. Technol.*, vol. 6, pp. 495-506, 2002.

- [146] J. Schetz and A. Padhey, "Penetration and breakup of liquids in subsonic airstreams," *AIAA J.*, vol. 15, no. 10, pp. 1385-1390, 1977.
- [147] J. N. Stenzler, J. Lee, D. Santavicca and W. Lee, "Penetration of liquid jets in a cross-flow," *Atomization Sprays*, vol. 16, pp. 887-906, 2006.
- [148] S. Tambe, S. Jeng, H. Mongia and G. Hsiao, "Liquid jets in subsonic crossflow," in *43rd AIAA Aerospace Sciences Meeting and Exhibit*, Reno, Nevada, 10-13 January 2005.
- [149] P. Wu, K. Kirkendall, R. Fuller and A. Nejad, "Breakup processes of liquid jets in subsonic crossflows," *J. Propul. Power*, vol. 13, no. 1, pp. 64-72, 1997.
- [150] P. Wu, K. Kirkendall, R. Fuller and A. Nejad, "Spray structures of liquid jets atomized in subsonic crossflows," *J. Propul. Power*, vol. 14, no. 2, pp. 173-182, 1998.
- [151] M. Herrmann, "Detailed numerical simulations of the primary atomization of a turbulent liquid jet in crossflow," *J. Eng. Gas. Turbines Power*, vol. 132, p. 061506, 2010.
- [152] X. Li and M. Soteriou, "High-fidelity simulation of high density-ratio liquid jet atomization in crossflow with experimental validation," in *ILASS Americas, 26th Annual Conference on Liquid Atomization and Spray Systems*, Portland, Oregon, 18-21 May 2014.
- [153] F. Xiao, M. Dianat and J. McQuirk, "Large eddy simulation of liquid-jet primary breakup in air crossflow," *AIAA J.*, vol. 51, no. 12, pp. 2878-2893, 2013.
- [154] E. Farvardin and A. Dolatabadi, "Simulation of biodiesel jet in cross flow," in *12th Triennial International Conference on Liquid Atomization and Spray Systems*, Heidelberg, Germany, 2-6 Sep. 2012.
- [155] X. Li and M. Soteriou, "Validation of high-fidelity simulation of liquid jet atomization in crossflow," in *ILASS Americas, 27th Annual Conference on Liquid Atomization and Spray Systems*, Raleigh, North Carolina, 17-20 May 2015.
- [156] J. Becker and C. Hassa, "Liquid fuel placement and mixing of generic aeroengine premix module at different operating conditions," *J. Eng. Gas. Turbines Power*, vol. 125, pp. 901-908, 2003.
- [157] X. Gong, K. Choi and N. Cernansky, "Lean direct wall injection mode atomization of liquid jets in swirling flow," *J. Propul. Power*, vol. 22, pp. 209-210, 2006.
- [158] T. Sikroria, A. Kushari, S. Syed and J. Lovett, "Experimental investigation of liquid jet breakup in a crossflow of a swirling air stream," *J. Eng. Gas. Turbines Power*, vol. 136, p. 061501, 2014.
- [159] S. Tavangar, S. Hashemabadi and A. Saberimoghadam, "CFD simulation for secondary breakup of coal-water slurry drops using OpenFOAM," *Fuel Process. Technol.*, vol. 132, pp. 153-163, 2015.
- [160] X. Tian, H. Zhao, H. Liu, W. Li and J. Xu, "Three-dimensional large eddy simulation of round liquid jet primary breakup in coaxial gas flow using the VOF method," *Fuel Process. Technol.*, vol. 131, pp. 396-402, 2015.

- [161] E. Farvardin and A. Dolatabadi, "Numerical simulation of the breakup of elliptical liquid jet in still air," *J. Fluids Eng.*, vol. 135, no. 7, p. 071302, 2013.
- [162] T. Yamamoto, "Setting and Usage of OpenFOAM multiphase solver (S-CLSVOF)," in *30th OpenCAE study meeting*, Kansai, Japan, 31 May 2014.
- [163] E. Lubarsky, D. Shcherbik, O. Bibik, Y. Gopala and B. Zinn, "Fuel jet in cross flow - experimental study of spray characteristics," in *Advanced Fluid Dynamics*, H.W. Oh, Ed., Vienna, Austria, INTECH Open Access Publisher, 2012.
- [164] M. Jadidi, S. Moghtadernejad and A. Dolatabadi, "Penetration and breakup of liquid jet in transverse free air jet with application in suspension-solution thermal sprays," *Mater. Des.*, vol. 110, pp. 425-435, 2016.
- [165] P. Fauchais, J. Heberlein and M. Boulos, *Thermal Spray Fundamentals: From Powder to Part*, New York, USA: Springer, 2014.
- [166] R. Lima and B. Marple, "Process-property-performance relationships for titanium dioxide coatings engineered from nanostructured and conventional powders," *Mater. Des.*, vol. 29, pp. 1845-1855, 2008.
- [167] S. Hong, Y. Wu, B. Wang, Y. Zheng, W. Gao and G. Li, "High-velocity oxygen-fuel spray parameter optimization of nanostructured WC-10Co-4Cr coatings and sliding wear behavior of the optimized coating," *Mater. Des.*, vol. 55, pp. 286-291, 2014.
- [168] J. Kim, H. Yang, K. Baik, B. Seong, C. Lee and S. Hwang, "Development and properties of nanostructured thermal spray coatings," *Curr. Appl. Phys.*, vol. 6, pp. 1002-1006, 2006.
- [169] P. Fauchais, M. Vardelle, S. Goutier and A. Vardelle, "Key challenges and opportunities in suspension and solution plasma spraying," *Plasma Chem. Plasma Process*, vol. 35, no. 3, pp. 511-525, 2015.
- [170] P. Fauchais, M. Vardelle, A. Vardelle and S. Goutier, "What do we know, what are the current limitations of suspension plasma spraying," *J. Therm. Spray Technol.*, vol. 24, pp. 1120-1129, 2015.
- [171] J. Stenzler, J. Lee and D. Santavicca, "Penetration of liquid jets in a crossflow," in *Proceedings of 41st Aerospace Science Meeting and Exhibit*, Reno, ND, USA, 6-9 January 2003.
- [172] T. Inamura, N. Nagai, T. Watanabe and N. Yatsuyanagi, "Disintegration of liquid and slurry jets traversing subsonic airstreams," in *Proceedings of 3rd World Conference on Experimental Heat Transfer, Fluid Mechanics, and Thermodynamics*, Honolulu, HI, USA, 31 Oct. - 5 Nov. 1993.
- [173] B. Masuda, R. Hack, V. McDonnell, G. Oskam and D. Cramb, "Some observations of liquid jet in crossflow," in *Proceedings of 18th Annual Conference on Liquid and Atomization and Spray Systems*, Irvine, CA, USA, 22-25 May 2005.

- [174] T. Chen, C. Smith, D. Schommer and A. Nejad, "Multi-zone behavior of transverse liquid jet in high-speed flow," in *Proceedings of 31st AIAA Aerospace Sciences Meeting and Exhibit*, Reno, ND, USA, 11-14 January 1993.
- [175] M. Birouk and N. Lekic, "Liquid jet breakup in quiescent atmosphere: A review," *Atomization Sprays*, vol. 19, pp. 501-528, 2009.
- [176] C. Dumouchel, "On the experimental investigation on primary atomization of liquid streams," *Exp. Fluids*, vol. 45, pp. 371-422, 2008.
- [177] H. Vahedi Tafreshi and B. Pourdeyhimi, "The effects of nozzle geometry of water jet breakup at high Reynolds numbers," *Exp. Fluids*, vol. 35, pp. 364-371, 2003.
- [178] D. Damiani, D. Tarlet and E. Meillot, "A particle-tracking-velocimetry (PTV) investigation of liquid injection in a DC plasma jet," *J. Therm. Spray Technol.*, vol. 23, pp. 340-353, 2014.
- [179] E. Meillot, R. Vert, C. Caruyer, D. Damiani and M. Vardelle, "Manufacturing nanostructured YSZ coatings by suspension plasma spraying (SPS): effect of injection parameters," *J. Phys. D: Appl. Phys.*, vol. 44, p. 194008, 2011.
- [180] C. Caruyer, S. Vincent, E. Meillot, J. Caltagirone and D. Dmiani, "Analysis of the unsteadiness of a plasma jet and the related turbulence," *Surf. Coat. Tech.*, vol. 205, pp. 1165-1170, 2010.
- [181] E. Meillot, D. Damiani, S. Vincent, C. Caruyer and J. Caltagirone, "Analysis by modeling of plasma flow interactions with liquid injection," *Surf. Coat. Tech.*, vol. 220, pp. 149-156, 2013.
- [182] E. Meillot, S. Vincent, C. Caruyer, D. Damiani and J. Caltagirone, "Modeling the interactions between a thermal plasma flow and a continuous liquid jet in a suspension spraying process," *J. Phys. D: Appl. Phys.*, vol. 46, p. 224017, 2013.
- [183] F. Girard, E. Meillot, S. Vincent, J. Caltagirone and L. Bianchi, "Contributions to heat and mas transfer between a plasma jet and droplets in suspension plasma spraying," *Surf. Coat. Tech.*, vol. 268, pp. 278-283, 2015.
- [184] P. Fauchais, M. Vardelle, S. Goutier and A. Vardelle, "Specific measurements of in-flight droplet and particle behavior and coating microstructure in suspension and solution plasma spraying," *J. Therm. Spray Technol.*, vol. 24, pp. 1498-1505, 2015.
- [185] Q. Wang, U. Mondragon, C. Brown and V. McDonell, "Characterization of trajectory, break point, and break point dynamics of a plain liquid jet in a crossflow," *Atomization Sprays*, vol. 21, pp. 203-219, 2011.
- [186] M. Birouk, C. Iyogun and N. Popplewell, "Role of viscosity on trajetory of liquid jets in a cross-airflow," *Atomization Sprays*, vol. 17, pp. 267-287, 2007.
- [187] E. Lubarsky, J. Reichel, B. Zinn and R. McAmis, "Spray in crossflow: dependence on Weber number," *J. Eng. Gas Turbines Power*, vol. 132, p. 021501, 2010.

- [188] D. Sedarsky, M. Paciaroni, E. Berrocal, P. Petterson, J. Zelina, J. Gord and M. Linne, "Model validation image data for breakup of a liquid jet in crossflow: part I," *Exp. Fluids*, vol. 49, pp. 391-408, 2010.
- [189] M. Linne, M. Paciaroni, E. Berrocal and D. Sedarsky, "Ballistic imaging of liquid breakup processes in dense sprays," *Proc. Combust. Inst.*, vol. 32, pp. 2147-2161, 2009.
- [190] S. No, "A review on empirical correlations for jet/spray trajectory of liquid jet in uniform crossflow," *Int. J. Spray Combust. Dyn.*, vol. 7, pp. 283-313, 2015.
- [191] M. Linne, M. Paciaroni, J. Gord and T. Meyer, "Ballistic imaging of the liquid core for a steady jet in crossflow," *Appl. Opt.*, vol. 44, pp. 6627-6634, 2005.
- [192] A. Cavaliere, R. Ragucci and C. Noviello, "Bending and break-up of a liquid jet in high pressure airflow," *Exp. Therm. Fluid Sci.*, vol. 27, pp. 449-454, 2003.
- [193] A. Bellofiore, A. Cavaliere and R. Ragucci, "Air density effect on the atomization of liquid jets in crossflow," *Combust. Sci. Technol.*, vol. 179, pp. 319-342, 2007.
- [194] M. Herrmann, M. Arienti and M. Soteriou, "The impact of density ratio on the liquid core dynamics of a turbulent liquid jet injected into a crossflow," *J. Eng. Gas Turbines Power*, vol. 133, p. 061501, 2011.
- [195] R. Fuller, P. Wu, K. Kirkendall and A. Nejad, "Effects of injection angle on atomization of liquid jets in transverse airflow," *AIAA J.*, vol. 38, pp. 64-72, 2000.
- [196] M. Costa, M. Melo, J. Sousa and Y. Levy, "Spray characteristics of angled liquid injection into subsonic crossflows," *AIAA J.*, vol. 44, pp. 646-653, 2006.
- [197] K. Ahn, J. Kim and Y. Yoon, "Effects of orifice internal flow on transverse injection into subsonic crossflows: cavitation and hydraulic flip," *Atomization Sprays*, vol. 16, pp. 15-34, 2006.
- [198] F. White, *Fluid Mechanics*, 4th ed., New York, USA: McGraw-Hill, 1999.
- [199] "ImageJ, Image Processing and Analysis in Java," [Online]. Available: <http://imagej.nih.gov/ij/>.
- [200] S.D. Sovani, P.E. Sojka and A.H. Lefebvre, "Effervescent atomization," *Prog. Energy Combust. Sci.*, vol. 27, pp. 483-521, 2001.
- [201] A.H. Lefebvre, "Airblast atomization," *Prog. Energy Combust. Sci.*, vol. 6, pp. 233-261, 1980.
- [202] A.R. Sharma, *Liquid jet in oscillating crossflow: characterization of near-field and far-field spray behavior*, Cincinnati, Ohio: Master Thesis, University of Cincinnati, 2015.
- [203] K.D. Kihm and P. Deignan, "Dynamic surface tension of coal-water slurry fuels," *Fuel*, vol. 74, pp. 295-300, 1995.
- [204] M. Herrmann, "A sub-grid surface dynamics model for sub-filter surface tension induced interface dynamics," *Comput. Fluids*, vol. 87, pp. 92-101, 2013.

- [205] M. Herrmann, "A dual-scale LES subgrid model for turbulent liquid/gas phase interface dynamics," in *ASME/JSME/KSME 2015 Joint Fluids Engineering Conference*, Seoul, South Korea, 26-31 July 2015.
- [206] P.R. Choudhury, "Slurry fuels," *Prog. Energy Combust. Sci.*, vol. 18, pp. 409-427, 1992.
- [207] D. Gerlach, N. Alleborn, V. Buwa and F. Durst, "Numerical simulation of periodic bubble formation at a submerged orifice with constant gas flow rate," *Chem. Eng. Sci.*, vol. 62, pp. 2109-2125, 2007.

Appendix: A coupled level set and volume of fluid method with application to compressible two-phase flow

“Reprinted from the paper published in the 22nd Annual Conference of the CFD Society of Canada, Toronto, Canada, 1-4 June 2014, [66]”

A simple coupling of Level Set (LS) and Volume of Fluid (VOF) methods (S-CLSVOF) with application in compressible gas-liquid two-phase flow is presented. The LS method is added to the compressible VOF solver in OpenFOAM [64], which is a CFD Open source solver library, to improve the computation of interface curvature and surface tension force. The results of this method and compressible VOF solver are compared for a test case. It is shown that the interface curvature and the surface tension force computations are considerably improved by adding LS method to the compressible VOF solver. The governing equations solved in compressible VOF (compressibleInterFoam) are given below

Continuity equation

$$\frac{\partial \rho}{\partial t} + \nabla \cdot (\rho \mathbf{U}) = 0 \quad \text{Equation A.1}$$

Momentum equation

$$\frac{\partial \rho \mathbf{U}}{\partial t} + \nabla \cdot (\rho \mathbf{U} \mathbf{U}) = -\nabla \left(p + \frac{2}{3} \mu \nabla \cdot \mathbf{U} \right) + \rho \mathbf{g} + [\nabla \cdot (\mu \nabla \mathbf{U}) + \nabla \mathbf{U} \cdot \nabla \mu] + \sigma \kappa \nabla \alpha_1 \quad \text{Equation A.2}$$

where σ is the surface tension, κ is the curvature of the free surface and α_1 is the phase fraction of phase 1. It should be noted that curvature of the free surface is calculated from the phase fraction α_1 as

$$\kappa = -\nabla \cdot \left(\frac{\nabla \alpha_1}{|\nabla \alpha_1|} \right) \quad \text{Equation A.3}$$

Equation of State

$$\rho_i = \rho_{0i} + \Psi_i p \quad \text{Equation A.4}$$

where the subscript i denotes the phase i and Ψ_i is the compressibility $\Psi_i = 1/c_i^2$ and c_i here is the speed of sound. For a compressible phase (i.e. gas) the nominal density ρ_0 is set to zero which leads to an ideal gas equation of state for an isothermal fluid. For the low compressibility phase (i.e. liquid) ρ_0 is set to the nominal density of the liquid under normal conditions. Therefore, a constant liquid density is used unless the liquid is subjected to very high pressures.

Volume fraction equation

The volume fraction equation of a compressible flow is written as

$$\frac{\partial \alpha_1}{\partial t} + \nabla \cdot (\alpha_1 \mathbf{U}) + \nabla \cdot (\mathbf{U}_c \alpha_1 (1 - \alpha_1)) = \alpha_1 (1 - \alpha_1) \left(\frac{\Psi_2}{\rho_2} - \frac{\Psi_1}{\rho_1} \right) \frac{Dp}{Dt} + \alpha_1 \nabla \cdot \mathbf{U} \quad \text{Equation 0A.5}$$

The MULES (multidimensional universal limiter with explicit solution) method is used to solve the volume fraction advection equation. The algorithm developed by Albadawi *et al.* [68] and discussed in chapter 4 is used for coupling LS and compressible VOF here. The level set function is initialized using Equation (4.11). After solving the re-initialization equation, the interface curvature and surface tension force are computed using Equations (4.14) and (4.15). The density and viscosity of both phases are calculated by Equations (4.18) and (4.19).

In this study, we assess our method based on a 3D bubble growth and detachment problem. Additionally, our method is compared with the compressible VOF method available in OpenFOAM. The schematic diagram of the numerical domain can be seen in Figure (A.1). During the process, air comes out of an orifice and forms a bubble. Within time the bubble volume increases continuously. However, the lift force causes the bubble to detach and rise upwards [207]. A parabolic velocity profile is assumed at the air inlet for the boundary condition. The maximum

velocity in the parabolic velocity profile is calculated based on the air flow rate [68]. The air flow rate is equal to 200 mlph. For the lower wall, the adhesion boundary condition is used to prevent bubble interface spreading along the wall. The wall static contact angle is set to 20° while no slip boundary condition is used for the other walls. To expose the initial condition, a semi-spherical bubble at the inflow is patched so that the distance function for LS method can be calculated. It should be noted that the gravity force is considered in the mentioned problem. Also, the physical properties of the fluids are assumed to be constant. The PIMPLE scheme is used to couple pressure and velocity. Furthermore, the Courant number of 0.25 with adaptive time step is used to control the computations.

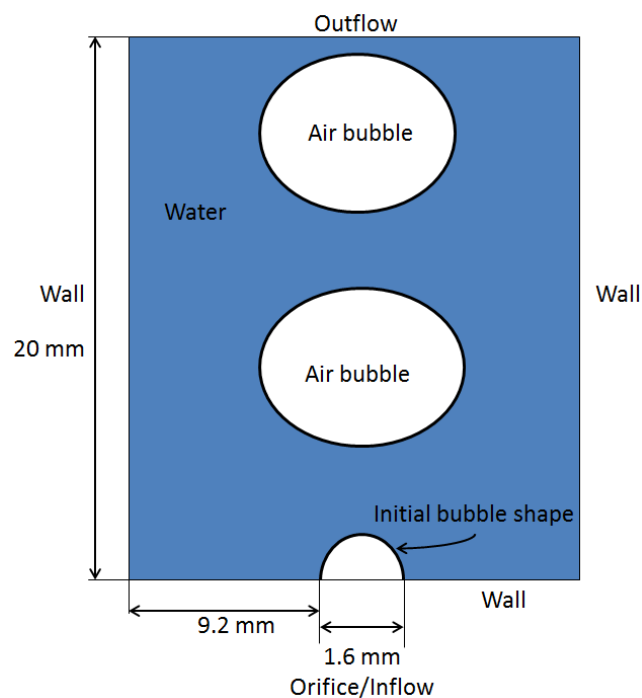


Figure A.1 Schematic diagram of the problem of bubble growth and detachment

The comparison between the numerical results and the experimental measurements [68] is shown in Figure (A.2). It is worth noting that the numerical interfaces are obtained from

compressible VOF and S-CLSVOF mentioned above. As can be seen in Figure (A.2), the VOF method predicts the bubble with smaller volume and height. On the other hand, the S-CLSVOF results are in good agreement with experimental data. The bubble detachment time resulting from the experiment, VOF, and S-CLSVOF are 0.523, 0.327 and 0.421 s respectively. It is clear that the computations of interface curvature and surface tension force are improved by S-CLSVOF.

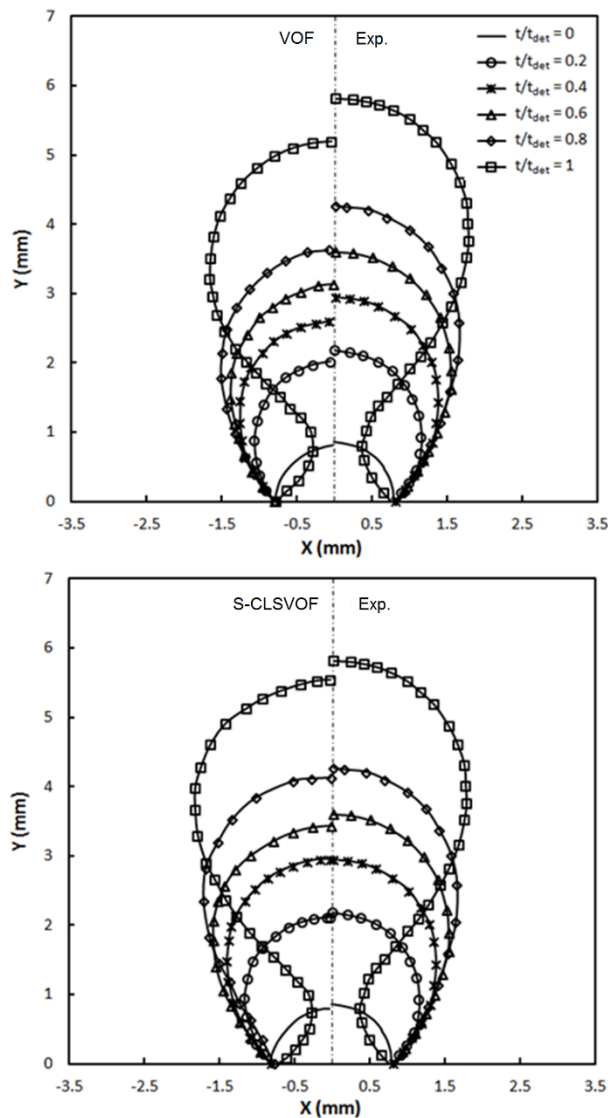


Figure A.2 Bubble shape predictions by experimental [68], VOF and S-CLSVOF for the problem of bubble growth and detachment